**Monika Dźwigońska**

# The role of epigenetic and transcriptomic changes in the hypoxic microenvironment of glioma

PhD thesis
Completed at the Laboratory of Tumour Hypoxia and Epigenomics and the Laboratory of Molecular Neurobiology
of the Nencki Institute of Experimental Biology
Polish Academy of Sciences

**SUPERVISOR**
**Dr. Katarzyna Leszczyńska, Ph.D., D.Sc.**

Warsaw, 2025

## *Podziękowania*

*Szczególne podziękowania kieruję do mojej promotor dr hab. Katarzyny Leszczyńskiej. Dziękuję za przekazaną wiedzę, doświadczenie oraz wszelką pomoc i cenne rady udzielane w trakcie realizacji badań i pisania niniejszej pracy. Jestem ogromnie wdzięczna za liczne możliwości sprzyjające mojemu rozwojowi naukowemu, a także nieocenione wsparcie w każdej sytuacji. Dziękuję również za wiarę w moje możliwości, zaufanie oraz przyjazną atmosferę, które towarzyszyły mi na każdym etapie pracy.*

*Dziękuję prof. dr hab. Bożenie Kamińskiej-Kaczmarek za możliwość pracy w swoim zespole, przekazaną wiedzę oraz cenne uwagi w trakcie realizacji moich badań w Pracowni Neurobiologii Molekularnej Instytutu Nenckiego PAN.*

*Dziękuję dr hab. Jakubowi Mieczkowskiemu za wprowadzenie mnie w świat bioinformatyki, za poświęcony czas i cierpliwość, zwłaszcza na początku mojej drogi, za wszystkie wskazówki dotyczące analiz oraz za wiarę, że mogę i potrafię więcej.*

*Ogromne podziękowania kieruję do wszystkich Koleżanek i Kolegów z Pracowni Neurobiologii Molekularnej oraz Pracowni Hipoksji i Epigenomiki Nowotworów Instytutu Nenckiego PAN. W szczególności dziękuję: dr Paulinie Kamińskiej za bycie najlepszą towarzyszką doktoranckiej codzienności, za wsparcie, zrozumienie i wszystkie chwile, które czyniły tę drogę łatwiejszą; Szymonowi Lipcowi za optymizm, inspirację do działania i wszystkie ciekawe rozmowy, nie tylko naukowe; dr Aleksandrze Ellert-Miklaszewskiej, dr Katarzynie Poleszak, dr Paulinie Pilanc-Kudlek oraz dr Salwadorowi Cyranowskiemu za tworzenie przyjaznej, inspirującej i pełnej wsparcia atmosfery w pracy; dr Pawłowi Segitowi, dr Karolowi Jackowi, dr Adrii Jaume Roura-Canalda oraz dr hab. Bartoszowi Wojtasiowi za każdą pomoc w analizach bioinformatycznych oraz Patrycji Rosie za przeprowadzone analizy single-cell RNA-seq.*

*Dziękuję moim Przyjaciołom, w szczególności siostrze Natalii, Patrykowi, Justynie, Mateuszowi oraz grupie Archihehe, którzy zawsze wiernie mi kibicowali. Dziękuję za wspólny czas, rozmowy i za wszystkie chwile, które wniosły dużo radości do mojej codzienności.*

*Szczególnie dziękuję moim Rodzicom, Beacie i Waldemarowi. To dzięki Waszemu wsparciu i trosce o mój rozwój mogłam podążać za swoimi naukowymi zainteresowaniami.*

*Najmocniejsze podziękowania kieruję do mojego męża, Jarka. Dziękuję za Twoją obecność, ciekawość, nieustające wsparcie i wyrozumiałość.*
*Tobie dedykuję niniejszą pracę.*

This study was supported by the following research grants:

NCN, OPUS 17, 2019/33/B/NZ1/01556
EU, HORIZON-MISS-2023-CANCER-01, HIT-GLIO, 101136835

# Table of contents

# Abstract

Hypoxia is a common feature of solid tumours, arising from abnormal vasculature that fails to deliver sufficient oxygen to rapidly proliferating tumour cells. This physiological stress plays a pivotal role in tumour progression by contributing to genomic instability, enhancing cellular invasiveness, metastatic potential, suppressing anti-tumour immunity, and reducing the efficacy of major treatments. In IDH-wild-type glioblastoma (GBM), the most aggressive and deadly primary brain tumour, intratumoral hypoxia is highly extensive and represents a critical determinant of poor patient survival. Moreover, the GBM microenvironment is infiltrated by diverse cell types, with glioma-associated microglia and macrophages (GAMs) constituting the predominant population. These cells can adopt immunosuppressive phenotypes and are recognised as major contributors of glioma progression. Since GAMs are commonly recruited to hypoxic niches, such stress can further enhance their tumour-promoting functions. One of key cellular responses to hypoxia is the remodelling of chromatin properties through histone modifications and DNA methylation. However, the extent to which these changes contribute to the hypoxia-driven reprogramming of the GBM transcriptome is not yet fully understood. In this study, the impact of hypoxic stress on chromatin reprograming and transcriptomic profiles within the glioma TME was investigated, particularly in GAMs. First, using the Assay for Transposase-Accessible Chromatin using sequencing (ATAC-seq) approach, hypoxia-dependent chromatin alterations were assessed in glioma cells. The data revealed global reduction in chromatin accessibility at promoter regions of numerous genes under hypoxic condition (<0.1% $O_2$). Notably, specific functional pathways were affected, including those involved in mRNA processing and splicing, as well as regulators of R-loop formation. Second, hypoxia was found to alter the expression of key identity marker genes in GAMs. In glioma-co-cultured GAMs *in vitro* and in glioblastoma patient samples, hypoxia upregulated the expression of monocytic marker *Lgals3* and downregulated the homeostatic microglial markers *P2ry12* and *Tmem119*. In addition, hypoxic stress appeared to interfere with multiple functional markers, including genes related to lipid metabolism, phagocytosis, chemotaxis, ribosomal biogenesis, and the interferon response. Some of these hypoxia-induced changes in GAMs were fine-tuned through the changes in chromatin accessibility. Furthermore, it was found that hypoxia induced lipid droplet accumulation in myeloid cells via increased expression of lipid storage-related genes and this effect could be reversed through targeting epigenetic

mechanisms with histone deacetylase inhibitors. Overall, these findings highlight hypoxic stress as a potent epigenomic and transcriptomic regulator of glioma TME which may hold significance for future basic research and clinical applications.

# Streszczenie

Hipoksja jest częstą cechą guzów litych, wynikającą z nieprawidłowego unaczynienia, które nie jest w stanie dostarczyć wystarczającej ilości tlenu do szybko proliferujących komórek guza. Ten stres fizjologiczny odgrywa kluczową rolę w progresji nowotworu, przyczyniając się do niestabilności genomowej, zwiększając inwazyjność komórek i potencjał przerzutów, osłabiając odpowiedź przeciwnowotworową układu odpornościowego czy zmniejszając skuteczność głównych metod leczenia. Glejak złośliwy z prawidłowym genem IDH (ang. IDH-wild-type glioblastoma, GBM) jest najbardziej agresywnym i śmiertelnym pierwotnym guzem mózgu. Regiony hipoksji w GBM są bardzo rozległe i stanowią istotny czynnik determinujący złe rokowania pacjentów. Ponadto mikrośrodowisko GBM jest naciekane przez różne typy komórek, spośród których dominującą populację stanowią mikroglej i makrofagi związane z glejakiem (ang. glioma-associated microglia and macrophages, GAMs). Komórki te zamiast inicjować odpowiedź przeciwnowotworową, wykazują fenotyp immunosupresyjny wspierając tym samym wzrost guza. Ponadto GAMs są często rekrutowane do hipoksyjnych nisz guza, co może prowadzić do dalszych zmian fenotypowych sprzyjających rozwojowi nowotworu. Jedną z kluczowych odpowiedzi komórkowych na hipoksję jest przebudowa chromatyny poprzez zmiany modyfikacji histonów czy metylację DNA. Jednak stopień, w jakim zmiany te wpływają na zależne od hipoksji przeprogramowanie transkryptomu GBM nie jest jeszcze w pełni poznany. W niniejszej rozprawie doktorskiej zbadano wpływ stresu hipoksycznego na organizację chromatyny i profile transkryptomiczne w mikrośrodowisku glejaka, w szczególności w komórkach GAMs. W pierwszym etapie oceniono wpływ hipoksji na dostępność chromatyny w komórkach glejaka metodą ATAC-seq (ang. Assay for Transposase-Accessible Chromatin using sequencing). Dane wykazały globalne zmniejszenie dostępności chromatyny w regionach promotorów wielu genów w warunkach hipoksji (<0.1% O2). Szczególnie dotyczyło to szlaków związanych z przetwarzaniem i splicingiem mRNA oraz regulacją pętli R (ang. R-loop). W kolejnym etapie wykazano, że niedotlenienie zmienia ekspresję kluczowych genów wykorzystywanych do identyfikacji GAMs. W hodowlach komórek GAMs i glejaka *in vitro* oraz w próbkach pochodzących od pacjentów z GBM hipoksja zwiększyła ekspresję markera makrofagów obwodowych *Lgals3,* jednocześnie obniżając ekspresję homeostatycznych markerów mikrogleju *P2ry12* i *Tmem119.* Ponadto hipoksja wpłynęła na ekspresje wielu markerów

funkcjonalnych, w tym genów związanych z metabolizmem lipidów, fagocytozą, chemotaksją, biogenezą rybosomów oraz odpowiedzią interferonową. Część zmian indukowanych przez hipoksję w GAMs była regulowana poprzez przebudowę chromatyny. Wykazano również, że hipoksja indukuje akumulację kropli lipidowych w komórkach mikrogleju i makrofagów poprzez zwiększoną ekspresję genów związanych z magazynowaniem lipidów. Dodatkowo efekt ten może być odwrócony dzięki celowaniu w mechanizmy epigenetyczne, np. przy użyciu inhibitorów deacetylaz histonowych. Podsumowując, przedstawione badania podkreślają rolę hipoksji jako silnego regulatora zmian epigenomicznych i transkryptomicznych w mikrośrodowisku glejaka, co może mieć kluczowe znaczenie dla dalszych badań podstawowych, jak i dla zastosowań klinicznych.

# Abbreviations

ATAC-seq - Assay for Transposase-Accessible Chromatin using sequencing

ATF4 - activating transcription factor 4

ATF3 - activating transcription factor 3

ATM - ataxia-telangiectasia mutated

ATR - ataxia-telangiectasia-and-Rad3-related protein

BMDMs - bone marrow-derived macrophage cells

BSA - bovine serum albumin

CA9 - carbonic anhydrase 9

COX - cytochrome c oxidase

CUT&RUN - Cleavage Under Targets and Release Using Nuclease

DDR - DNA damage response

DMEM - Dulbecco's Modified Eagle Medium

EDTA - ethylenediaminetetraacetic acid

EGTA - ethylene glycol-bis (β-aminoethyl ether)-N,N,N′,N′-tetraacetic acid

eIF2α - eukaryotic initiation factors

FABPs - fatty acid-binding proteins

FACS - fluorescence activated cell sorting

FBS - fetal bovine serum

GAMs - glioma-associated microglia/macrophages

GBM - glioblastoma

GLUT1 - glucose transporter 1

GLUT3 - glucose transporter 3

HATs - histone lysine acetyltransferases

HDACs - histone deacetylases

HDACi - histone deacetylases inhibitor

HDAC7 - histone deacetylase 7

HIFs - hypoxia-inducible factors

HIF-1α - hypoxia-inducible factor 1 alpha

HIF-1β - hypoxia-inducible factor 1 beta

HREs - hypoxia response elements

HRP - horseradish peroxidase

IDH - isocitrate dehydrogenase

IRF8 - interferon regulatory factor 8

JmjC - Jumonji C

KDMs - histone lysine demethylases

KLFs - Krüppel-like factors

KMTs - histone lysine methyltransferases

LDHA - lactate dehydrogenase A

LDs - lipid droplets

LGALS3 - galectin-3

LLM - lipid-laded macrophages

LPS - lipopolysaccharide

MGMT - O6-Methylguanine-DNA methyltransferase

MMP9 - matrix metalloproteinase 9

Mo - monocytes

Mφ - macrophages

PBS - phosphate-buffered saline

PBST - PBS with Tween

PCA - principal component analysis

PDK1 - pyruvate dehydrogenase kinase 1

PERK - protein kinase R-like endoplasmic reticulum kinase

PFA - paraformaldehyde

PHDs - prolyl hydroxylases

PLIN2 - perilipin-2

pVHL - Von Hippel–Lindau tumor suppressor

PTMs - post-translational modifications

RNA-seq - RNA sequencing

ROS - reactive oxygen species

RS - replication stress

RT - room temperature

SD - standard deviation

SDS - sodium dodecyl sulfate

SOX8 - SRY-box 8

TBST - Tris-Buffered Saline with Tween 20

TFs - transcription factors

TGFβ - transforming growth factor beta

TME - tumour microenvironment
VEGF - vascular endothelial growth factor

**Gene name**

To improve readability of the thesis, all gene descriptions are listed below. Throughout the thesis, mouse gene names are written in italics with only the first letter capitalised (e.g. *Lgals3*), whereas human gene symbols are written in italics in all uppercase letters (e.g. *LGALS3*). Listed below are the extended gene names, provided in accordance with mouse gene nomenclature (if not specified otherwise):

*Abca1* - ATP-binding cassette, sub-family A member 1
*Abcg1* - ATP binding cassette subfamily G member 1
*Adam8* - a disintegrin and metallopeptidase domain 8
*Adm* - adrenomedullin
*Adgre1* - adhesion G protein-coupled receptor E1
*Aldoa* - aldolase A, fructose-bisphosphate
*Alyref2* - Aly/REF export factor 2
*Apoe* - apolipoprotein E
*Arg1* - arginase
*Atf3* - activating transcription factor 3
*Bnip3* - BCL2/adenovirus E1B interacting protein 3
*Bnip3l* - BCL2/adenovirus E1B interacting protein 3-like
*Ccl2* - C-C motif chemokine ligand 2
*Cd37* – CD37antigen
*Cd68* - CD68 antigen
*Cd69* - CD69 antigen
*Cd74* – CD74 antigen
*Cd83* – CD83 antigen
*Cd109* - CD109 antigen
*Cstb* - cystatin B
*Ctsl* - cathepsin L
*Cxcl3* - C-X-C motif chemokine ligand 3
*Cytip* - cytohesin 1 interacting protein
*Ddr1* - discoidin domain receptor family, member 1

*Ddx1* - DEAD box helicase 1

*Ddx5* - DEAD box helicase 5

*Dhcr7* - 7-dehydrocholesterol reductase

*Ddx39b* - DEAD box helicase 39b

*Dhx9* - DExH-box helicase 9

*Dhx15* - DEAH-box helicase 15

*Dyrk3* - dual-specificity tyrosine phosphorylation regulated kinase 3

*Eno1b* - enolase 1B, retrotransposed

*Eno2* - enolase 2

*Ero1a* - endoplasmic reticulum oxidoreductase 1 alpha

*Fabp3* - fatty acid binding protein 3

*Fabp4* - fatty acid binding protein 4

*Fabp5* - fatty acid binding protein 5

*Fabp7* - fatty acid binding protein 7

*Fam162a* - family with sequence similarity 162, member A

*Fdft1* - farnesyl diphosphate farnesyl transferase

*Fgfr3* - fibroblast growth factor receptor 3

*Ftl1* - ferritin light polypeptide 1

*Gapdh* - glyceraldehyde-3-phosphate dehydrogenase

*Gdnf* - glial cell line derived neurotrophic factor

*Gfap* - glial fibrillary acidic protein

*Glut1* - glucose transporter protein type 1 (solute carrier family 2 member 1, *Slc2a1*)

*Gpi1* - glucose-6-phosphate isomerase 1

*Gpat3* - glycerol-3-phosphate acyltransferase 3

*Gpnmb* - glycoprotein (transmembrane) nmb

*Gpr34* - G protein-coupled receptor 34

*Hilpda* - hypoxia inducible lipid droplet associated

*Hk2* - hexokinase 2

*H2-Aa* - histocompatibility 2, class II antigen A, alpha

*HnrnpU* - heterogeneous nuclear ribonucleoprotein U

*HrnpK* - heterogeneous nuclear ribonucleoprotein K

*Ifitm2* - interferon induced transmembrane protein 2

*Ifit1* - interferon-induced protein with tetratricopeptide repeats 3

*Ifit3* - interferon-induced protein with tetratricopeptide repeats 3

*Ighm* - immunoglobulin heavy constant mu

*Itgam* - integrin alpha M

*Isg15* - ISG15 ubiquitin-like modifier

*Lama5* - laminin, alpha 5

*Lamc2* - laminin, gamma 2

*Lamp2* - lysosomal-associated membrane protein 2

*Ldha* - lactate dehydrogenase A

*Lfng* - LFNG O-fucosylpeptide 3-beta-N-acetylglucosaminyltransferase

*Lgals1* - lectin, galactose binding, soluble 1

*Lgals3* - lectin galactoside-binding doluble 3

*Lpin1* - lipin 1

*Lpin2* - lipin 2

*Lpin3* - lipin 3

*Map1lc3b* - microtubule-associated protein 1 light chain 3 beta

*Map1b* - microtubule-associated protein 1B

*Map6* - microtubule-associated protein 6

*Mef2c* - myocyte enhancer factor 2C

*Mif* - macrophage migration inhibitory factor (glycosylation-inhibiting factor)

*Mndal* - myeloid nuclear differentiation antigen

*Mt2* - metallothionein 2

*Myo5b* - myosin VB

*Ndrg1* - N-myc downstream regulated gene 1

*Nfam1* - Nfat activating molecule with ITAM motif 1

*Ngfr* - nerve growth factor receptor (TNFR superfamily, member 16)

*Nr1h2* - nuclear receptor subfamily 1, group H, member 2

*Nupr1* - nuclear protein transcription regulator 1

*Olfml3* - olfactomedin-like 3

*P2ry12* - purinergic receptor P2Y G-protein coupled 12

*Pecam1* - platelet/endothelial cell adhesion molecule 1

*Pgam1* - phosphoglycerate mutase 1

*Plac8* - placenta-specific 8

*Plin2* - perilipin 2

*Plin3* - perilipin 3

*Plp2* - proteolipid protein 2

*Plxnb3* - plexin B3

*Pkm* - pyruvate kinase, muscle

*Ppard* - peroxisome proliferator activator receptor delta

*Rab18* - RAB18, member RAS oncogene family

*Rab42* - RAB42, member RAS oncogene family

*Rala* - v-ral simian leukemia viral oncogene A

*Rassf2* - Ras association (RalGDS/AF-6) domain family member 2

*Rpl3* - ribosomal protein L13

*Rpl19* - ribosomal protein L19

*Rps15* - ribosomal protein S15

*Rsg16* - regulator of G-protein signaling 16

*S100a6* - S100 calcium binding protein A6 (calcyclin)

*S100a10* - S100 calcium binding protein A10 (calpactin)

*S100a11* - S100 calcium binding protein A11

*Scd4* - stearoyl-coenzyme A desaturase 4

*Sfpq* - splicing factor proline/glutamine rich

*Slc2a1* - solute carrier family 2

*Slc9b2* - solute carrier family 9, subfamily B (NHA2, cation proton antiporter 2)

*Snap23* - synaptosomal-associated protein 23

*Soat1* - sterol O-acyltransferase 1

*Soat2* - sterol O-acyltransferase 2

*Sparc* - secreted acidic cysteine rich glycoprotein

*Spi1* - Spi-1 proto-oncogene

*Spp1* - secreted phosphoprotein 1

*Srebf1* - sterol regulatory element binding transcription factor 1

*Srgn* - serglycin

*Srsf1* serine and arginine-rich splicing factor 1

*Tgfbi* - transforming growth factor, beta induced

*Thoc1* - THO complex 1

*Timp1* - tissue inhibitor of metalloproteinase 1

*Tmem119* - transmembrane protein 119

*Tnfrsf11a* - tumor necrosis factor receptor superfamily, member 11a, NFKB activator

*Tpi1* - triosephosphate isomerase 1

*Vamp4* - vesicle-associated membrane protein 4

*Vamp7* - vesicle-associated membrane protein 7

*Vegfa* - vascular endothelial growth factor A

*Vim* - vimentin

# 1. Introduction

## 1.1. Introduction to tumour hypoxia

Hypoxia refers to an insufficient level of oxygen, which can occur under both physiological and pathological conditions. In healthy tissues, oxygen ($O_2$) concentrations typically range from 3-10% $O_2$, depending on the tissue (**Table 1.1**) [1–3], and are often referred to as physioxia.

**Table 1.1. Examples of average oxygen levels in normal tissue.** $pO_2$ = partial pressure of oxygen, where 1 mmHg = 0.13% $O_2$.

| Tissue | $pO_2$ (mmHg) | % $O_2$ |
|---|---|---|
| Brain | 35 | 4.6 |
| Lung | 42.8 | 5.6 |
| Pancreatic | 51.6 | 6.8 |
| Kidney | 72 | 9.5 |
| Liver | 31 | 4.1 |
| Intestine | 61 | 8 |
| Skin | 8-35 | 1.1–4.6 |
| Muscle | 25 | 3.3 |
| Bone marrow | 54.9 | 7.1 |

Under physiological condition, low oxygen levels regulate multiple adaptive processes including glucose metabolism, embryogenesis, stem cell homeostasis or tissue repair and regeneration [4,5]. However, disruption of oxygen homeostasis results in pathological hypoxia, which is a common hallmark of the most solid tumours [1]. Tumour hypoxia arises due to an imbalance between oxygen consumption rate by rapidly and uncontrollably proliferating tumour cells and insufficient oxygen delivery due to a dysfunctional tumour vasculature. The hypoxic stress induces a set of mechanisms aimed to restore oxygen supply in cells, including upregulation of vascular endothelial growth factor (VEGF), which stimulates vascularization of the tumour mass. However, the vessels within a tumour tissue become leaky, tortuous and highly disorganised, resulting in an impairment of the blood flow, in places in a vessel collapse, and overall in a highly heterogeneous oxygenation within the tumour microenvironment (TME) [6,7]. Intratumoral oxygen concentrations vary spatially, ranging from mild hypoxia (≤ 2% $O_2$), to more severe hypoxia or even anoxia (<0.1% $O_2$), particularly in poorly vascularised or

avascular zones. These extreme prolonged conditions ultimately result in cell death and the formation of necrotic areas [1,8]. In addition, tumour hypoxia can be distinguished based on the fluctuations in the local oxygen periods. Chronic hypoxia refers to long-lasting oxygen decline (from hours to days), and typically arises in cells located more than 150-200 µm from a functional blood vessel [9]. Survival under these conditions depends on genetic adaptations of cells that regulate anaerobic metabolism, cell cycle control, and resistance to apoptosis, necrosis, or autophagy [10]. In contrast, brief periods of acute hypoxia (for minutes to hours) followed by re-oxygenation result in 'cycling' hypoxia. It occurs due to a transient blockage of blood vessels causing cycles of oxygen decrease and reoxygenation. This fluctuation triggers distinct biological responses compared to chronic hypoxia, as it generates excessive level of reactive oxygen species (ROS), DNA damage, specific transcriptomic changes, resulting in promotion of angiogenesis, therapy resistance and metastasis [11,12].

## 1.2. Cellular response to hypoxia

Cellular response to hypoxic environment involves a diverse range of processes at the level of transcription, translation, metabolism and epigenome. Those oxygen sensing pathways depend on the severity and duration of hypoxia and are also influenced by the cell type and interactions with other components of the TME (**Figure 1.1**) [10].

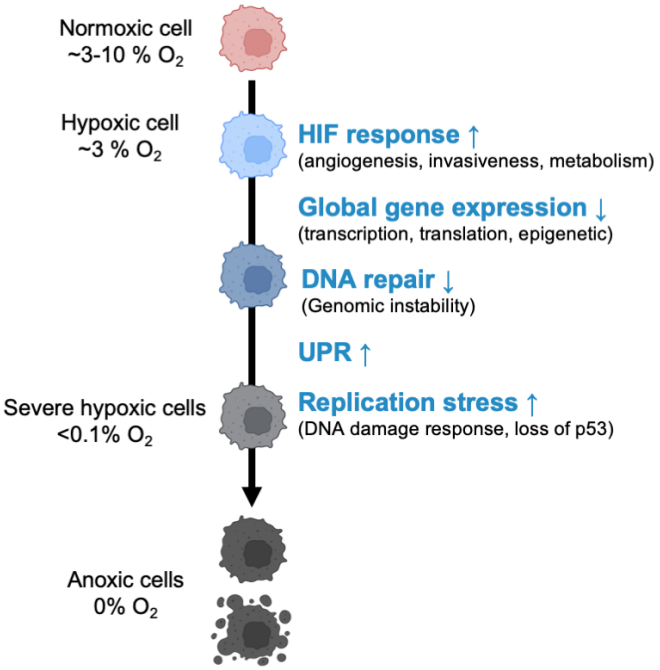


**Figure 1.1. Hypoxic oxygen level dictates diverse cellular signalling and responses during tumour evolution.** Graphics prepared with BioRender.com. HIF – hypoxia-inducible factor; UPR – unfolded protein response.

### 1.2.1. Hypoxia-inducible factors (HIFs)

A central role in the initial response under hypoxic stress is played by the family of transcription factors (TFs) named hypoxia-inducible factors (HIFs). Those TFs and their regulation were discovered and initially characterised by William G. Kaelin Jr, Sir Peter J. Ratcliffe and Gregg L. Semenza, who were awarded the 2019 Nobel Prize in Physiology or Medicine for showing "how cells sense and adapt to oxygen availability" [7]. HIFs are heterodimers composed of an oxygen-depended α subunit, including HIF-1α, HIF-2α or HIF-3α and a constitutively expressed HIF-1β subunit. Under normoxia (normal levels of oxygen), the oxygen-dependent degradation domain of HIF-α is hydroxylated by prolyl hydroxylases (PHDs), enzymes, which are active in the presence of $O_2$, iron ($Fe^{2+}$) and α- ketoglutarate. Then, hydroxylated HIF-α subunit is recognised and polyubiquitylated by the von Hippel-Lindau (pVHL)-containing E3 ubiquitin ligase complex and guided to the proteasomal degradation (**Figure 1.2**, left panel). In oxygen-deprived condition, oxygen-depended PHDs are inhibited, therefore HIF-α subunit remains unhydroxylated and stabilises due to the lack of degradation process. Subsequently, HIF-α translocates to the nucleus and dimerises with HIF-1β. HIF-α / HIF-1β complex binds then to the hypoxia response elements (HREs) present at promoters or gene bodies of select genes to induce their transcription (**Figure 1.2**, right panel) [7,13,14]. HIFs regulate a broad transcriptional program to promote tumour progression, including genes regulating angiogenesis (e.g. VEGF), metabolism (e.g. glucose transporters GLUT1, GLUT3), cellular pH (e.g. carbonic anhydrase 9 (CA9)), and other [7,15]. In addition, HIFs activation enhances cell migration, invasiveness and maintenance of stem-like states of cancer cells, collectively contributing to tumour progression, metastasis, and therapy resistance [1,7].

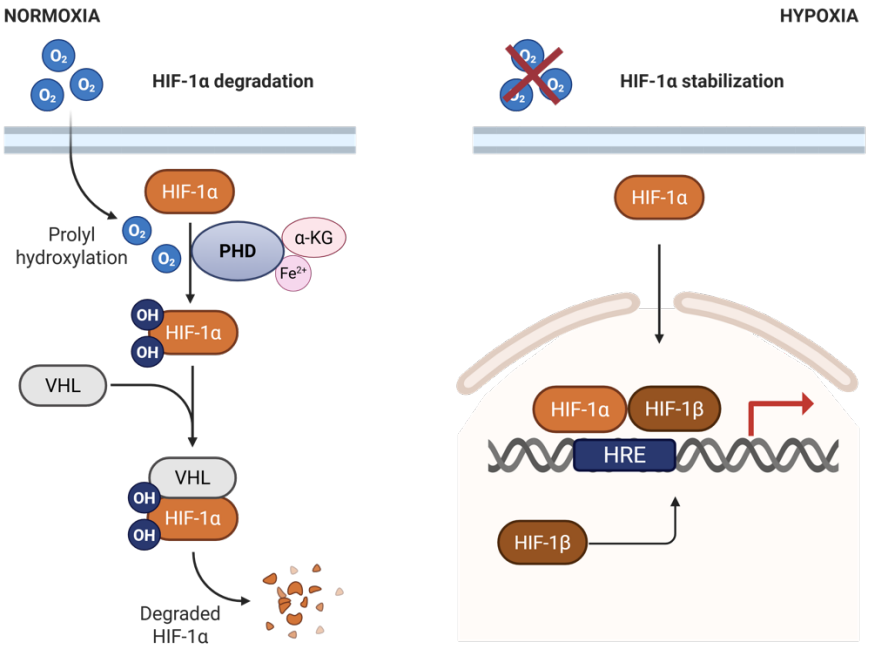


**Figure 1.2. Schematic diagram illustrating oxygen-dependent regulation of HIF-1α protein.** Graphics prepared with BioRender.com.

### 1.2.2. Glucose metabolism

Oxygen depletion in the TME rapidly triggers metabolic adaptations that are critical for cell survival under hypoxic stress. The majority of tumour cells relay on an aerobic glycolysis for the energy production, known as the Warburg effect, and hypoxia further promote this metabolism [16]. Beside the upregulation of glucose transporters responsible for extracellular glucose import (e.g. GLUT1 or GLUT3), hypoxia increases genes related to the glycolytic conversion of intracellular glucose, including aldolase and phosphofructokinase 1 (PFK1) [16]. Lactate dehydrogenase A (LDHA) and pyruvate dehydrogenase kinase 1 (PDK1) are also upregulated by HIFs, which promote production of lactate and limit the supply of pyruvate like acetyl-CoA needed for anabolic processes [17,18]. In addition, severe hypoxia influences the function of the mitochondrial electron transport chain (ECT), as oxidative phosphorylation relies on oxygen as the final electron acceptor [10]. In this process, the enzyme cytochrome c oxidase (COX) plays a key role in reducing oxygen to water, ultimately driving ATP production. Under hypoxia, COX activity is inhibited, reducing electron flux through the ETC and forcing hypoxic cancer cells to shift their metabolism towards anaerobic glycolysis [19]. Furthermore, COX inhibition leads to inefficient electron transfer and the accumulation of reactive oxygen species (ROS), which in turn contribute to the stabilisation of HIF-1α, and reinforcement of hypoxia-responsive pathways [8].

### 1.2.3. Lipid metabolism

Hypoxia also reprograms lipid metabolism, as rapidly proliferating cells in the TME require fatty acids and cholesterol for organelle biogenesis, energy storage and cell signalling [7]. Under low oxygen, HIFs enhance uptake and metabolism of glutamine, which enters the tricarboxylic acid (TCA) cycle to generate intermediates such as citrate, that is then converted to acetyl-CoA, as precursor of lipid synthesis [20]. In addition, in hypoxia, a level lipid desaturation, process that produces unsaturated fatty acids, is inhibited as stearoyl-CoA desaturase is oxygen depended [21]. To counteract the lipotoxic effects of excess saturated fats, hypoxic cells increase the uptake of unsaturated lipids from the extracellular environment via HIF-dependent upregulation of fatty acid–binding proteins (FABPs) and the fatty acid translocase CD36 [22–24]. Potentially toxic saturated fatty acids are then converted into neutral lipids and stored as lipid droplets (LDs), a process facilitated by increased expression of the lipid droplet-associated protein perilipin-2 (PLIN2) [25]. These hypoxia-driven alterations in lipid metabolism help cells survive metabolic stress, support rapid proliferation, but also suppress anti-tumour immunity, thereby promoting tumour progression.

### 1.2.4. Unfolded protein response, DNA damage response and DNA Repair

Under more prolonged and severe hypoxia (<0.1% $O_2$), other processes (independent of HIFs signalling) become activated (**Figure 1.1**) [10]. For instance, in the absence of oxygen, protein glycosylation and disulphide bond formation are disrupted, both of which are critical for the correct folding and processing of proteins [26]. This results in accumulation of unfolded or misfolded proteins and induction of unfolded protein response (UPR). A key important stress-sensing player of this pathway is protein kinase R-like endoplasmic reticulum kinase (PERK), which becomes activated in hypoxia and phosphorylates the eukaryotic initiation factors (eIF2α), leading to global inhibition of mRNA translation [27]. Beyond this translational regulation, the PERK–eIF2α axis also induces the expression of several hypoxia-responsive genes, including CA9, which mediates pH balance in cells, or transcription factor activating transcription factor 4 (ATF4), which is involved in amino acid metabolism, oxidative stress resistance, or autophagy [28–30].

A further distinct adaptation to severe hypoxia is the activation of the DNA damage response (DDR) [31]. This effect is linked to replication stress (RS), primary arising

from reduced nucleotide availability under hypoxic condition [32]. RS causes an extreme slow-down of DNA replication forks during DNA synthesis and is characterised by accumulation of single-stranded DNA [32,33]. This leads to the activation of two the most important proteins involved in DDR such as ataxia-telangiectasia mutated (ATM) and ataxia-telangiectasia-and-Rad3-related protein (ATR), which phosphorylate and activate a number of proteins that control cell cycle progression and induce apoptosis, including p53 tumour suppressor gene [34,35]. Over 50% of cases of the majority of tumour types harbour inactivating mutations or loss of p53 expression [36]. Hypoxia exerts a selective pressure to eliminate cells with high apoptotic potential through activation of p53-dependent apoptosis, thereby promoting the survival and expansion of apoptosis-resistant clones. This drives the emergence of aggressive, p53-deficient subclones and accelerates cancer evolution [37]. Additionally, hypoxia leads to increased level of R-loops, which are three-stranded nucleic acid structures formed by RNA/DNA hybrid paired with a displaced single-stranded DNA [38,39]. These structures are crucial in regulation of gene expression and also chromatin organisation. Abnormal R-loop accumulation can also magnify replication stress and genome instability, which are linked with cancer progression [39].

While the DNA damage response pathway and activation of ATM/ATR kinases mainly occurs due to replication stress rather than the actual DNA damage, the hypoxic conditions can also lead to DNA breaks when followed by reoxygenation or cycling hypoxia [40]. Moderate to severe hypoxia impairs DNA repair mechanism, including double-strand break (DSB) repair pathways such as: homologous recombination (HR) and non-homologous end joining (NHEJ), as well as mismatch repair (MMR); nucleotide excision repair (NER), and base excision repair (BER) [33]. These inhibitory effects occur at different regulatory levels and involve the role of HIFs, changes in post-translational protein modifications, and epigenetic modifications (epigenetic meaning alterations in histone post-translational modifications and/or DNA modifications) [13]. For instance, the key homologous recombination repair proteins such as RAD51 and BRCA1 are downregulated at both the transcriptional and translational levels, leading to the accumulation of mutations and thereby contributing to the genomic instability and carcinogenesis [40].

## 1.3. Consequences of Tumour Hypoxia

The presence of hypoxic regions within tumours is a detrimental factor to patients' outcomes, as numerous studies have shown that high tumour hypoxia correlates with a poor prognosis [41,42]. Hypoxia affects multiple processes that are critical for tumour progression and efficacy of existing therapies (**Figure 1.3**). For example, hypoxic stress can significantly contribute to resistance to radiotherapy. Ionizing radiation generates free radicals, which are further stabilised by the oxygen, leading to a DNA damage that is difficult to repair by the cell, and ultimately causes cell death [43]. In addition, oxygen is reduced by radiation to hydrogen peroxide, which initiates signalling cascades via ROS that contribute to secondary damage and inflammation in surrounding tissue [44]. In oxygen-deprived tissue, those mechanism are decreased and DNA damage is often reversible, resulting in resistance to radiation [13].

Hypoxia has been shown to impair delivery of drugs to cancer cells through several mechanism. Dysfunctional tumour vasculature may not effectively deliver drugs and ultimately limit the diffusion of chemotherapeutic agents. Furthermore, hypoxic cells typically exhibit low proliferation rates, which reduces the effectiveness of chemotherapeutic drugs that target dividing cells [45]. Tumour hypoxia is paired with acidosis and metabolic changes, which can also interfere with the activity of many therapeutic agents and make them less effective in those conditions [46]. In addition, hypoxia, through HIF-1α signalling, can induce the expression of drug efflux proteins such as ABC-transporters (ABCB1 or ABCG2), thereby contributing to multidrug resistance phenotype of tumour cells [47].

Other reasons why hypoxic tumour regions negatively impact patient's prognosis are associated with the capacity of hypoxia to drive aggressive phenotype of cancer cells. As mentioned above, severe hypoxia contributes to genomic instability through several mechanism including activation of DNA replication stress or decreased DNA repaired pathway. Accumulation of those processes (as consequence of faulty DNA replication, repair, or cell cycle arrest) may directly promote chromosomal instability characterised by structural rearrangements and abnormal chromosome number [10]. These genetically unstable cells are more aggressive and easily adapt to stress environmental condition enabling their selection and clonal expansion [48]. In addition, hypoxia imposes strong selective pressure alongside cancer driver genes. Under hypoxic conditions, mutations in tumour suppressor genes such as *p53* or *PTEN* are preferentially selected, promoting the

survival and expansion of apoptosis-resistant populations, driving the emergence of aggressive, therapy-resistant subpopulations, and accelerating cancer evolution [49].

Adaptation of tumour cells to hypoxic conditions enhances invasiveness and a distant metastatic ability of these cells. Hypoxia, primary through HIF-1a signalling, modulates multiple steps of the metastatic cascade. One key effect is a regulation of genes involved in epithelial-to-mesenchymal transition (EMT), a process where cancer cells become more motile and invasive by acquiring mesenchymal-like phenotype [10]. This includes the loss of E-cadherin and increased expression of N-cadherin, driven by transcription factors like TWIST, SNAI1/2 or ZEB1, resulting in reduced cell-cell adhesion and enhanced cell migration [50]. Hypoxia also regulates genes involved in disruption and remodelling of extracellular matrix (ECM), including matrix metalloproteinases (MMPs) such as MMP9 or MMP2 as well as lysyl oxidases (LOX), which are important players in shaping the premetastatic niche [51,52]. In addition, hypoxia induces angiogenesis, which provides ways for cancer cells to disseminate to distant organs.

Hypoxic regions of tumours not only enhance their metastatic capacity, but also profoundly affect the innate and adaptive immune responses. It was well confirmed that hypoxia is linked with reduced anti-tumour immunity. For instance, hypoxic zones often lack cytotoxic T cells or contain T cells that are dysfunctional and terminally exhausted [53]. In contrast, these regions actively recruit tumour-associated myeloid cells (discussed in detail below) and regulatory T cells, reprogramming them towards immunosuppressive phenotypes [54,55]. Hypoxia also promotes immune evasion by downregulation of MHC class I antigen presentation, supressing the activity of NK cells or T cells, and the upregulation of immune checkpoint molecules, such as PD-L1, on tumour and stromal cells, enabling cancer cells to escape the immune surveillance [56–58]. Additionally, hypoxic tumour cells release molecules including transforming growth factor beta (TGF-β), adenosine and lactate, that further suppress immune activity. Moreover, hypoxia suppress inflammatory responses and interferons signalling, further contributing to an immunosuppressive TME [44,59]. Together, tumour hypoxia is a critical stress factor that influences cancer biology on multiple levels, posing a serious problem for effective therapy.

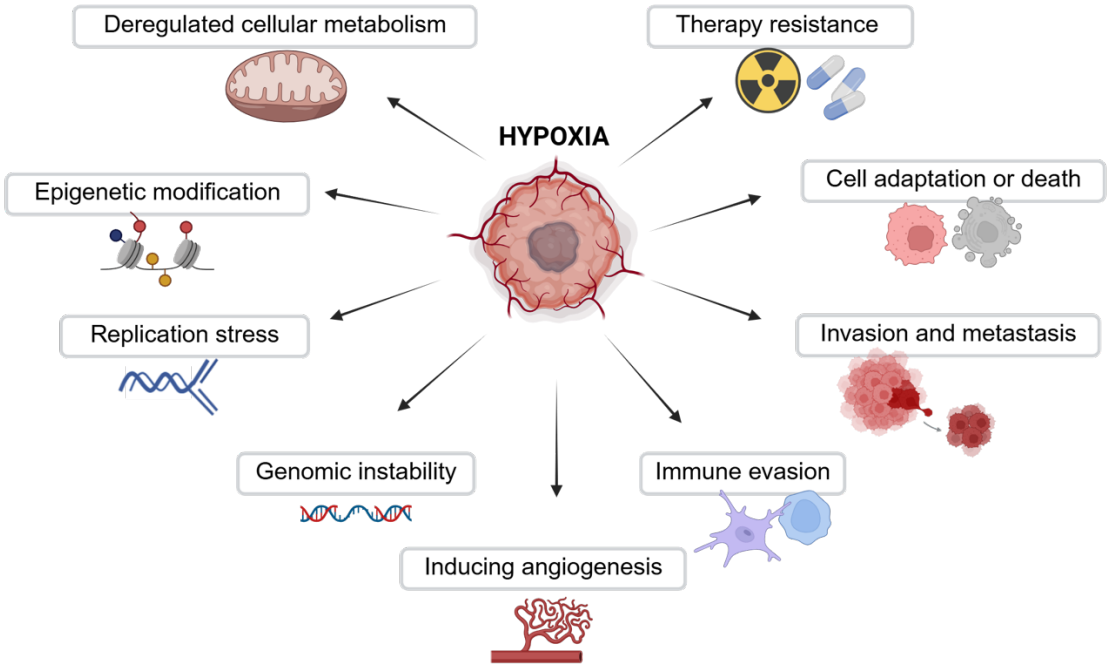


**Figure 1.3. Biological consequences of hypoxia in tumour progression.** Graphics prepared with BioRender.com.

## 1.4. Chromatin architecture and gene regulation

The precise regulation of gene expression is fundamental to the proper functioning of all cellular processes, including proliferation, differentiation or adaptation to external conditions. An important way of controlling gene expression is through epigenetic regulation of chromatin, such as alterations in histone post-translational modifications (PTMs) and DNA methylation. Chromatin is comprised of structural units called nucleosomes, each consisting of approximately 147 base pairs of DNA wrapped around a histone octamer, made of two molecules of each of four core histone proteins (H2A, H2B, H3 and H4) [60]. The nucleosome composition, histone PTMs, DNA methylation or chromatin remodelling complexes affect chromatin accessibility, which determines the ability of TFs and other regulatory proteins to access the DNA and regulate the gene expression [61]. Functionally, chromatin states can be categorised as 'open' chromatin with transcriptionally accessible region (euchromatin) and 'closed' chromatin which is more condensed and correlate with transcriptionally repressed regions (heterochromatin) (**Figure 1.4**) [62]. There are various types of PTMs, which occur primarily at the N-terminal tails of histones and are added or removed by specific histone-modifying enzymes, including writers and erasers, respectively [63]. Certain histone modification patterns influence chromatin properties and accessibility and provide

activating or repressing signals for gene expression. For example, histone acetylation occurs on lysine residues across histone H3 or H4, neutralizing the basic charge of histones and weakening their interaction with DNA. This leads to a more relaxed chromatin structure, which is associated with transcriptional activation. Histone acetylation is regulated by two competing types of enzymes, including histone lysine acetyltransferases (HATs), which transfer acetyl group from acetyl-CoA to a lysine, and histone deacetylases (HDACs) which remove acetyl groups, causing more condense chromatin structure [64]. Another example of well-defined PTMs in regulation of chromatin landscape are histone methylations, which occur mainly on lysine and arginine residues of H3 and H4. Histone methylation is also regulated by two groups of enzymes, including histone methyltransferases (HMTs) and histone demethylases (HDMs), which methylate and demethylate histones, respectively. Lysine residues can undergo mono- (me1), di- (me2), or trimethylation (me3), whereas arginine residues may be modified through me1 or me2 [62]. Importantly, specific PTMs are associated with distinct functional outcomes. For instance, acetylation of histone H3 lysine 27 (H3K27ac) and trimethylation at lysine 4 (H3K4me3) are predominantly found at regulatory regions such as promoters and are associated with active gene expression. Additionally, presence of H3K27ac together with H3K4me1 marks nucleosomes flanking active enhancer elements. In contrast, me3 of histone H3 lysine 9 or 27 (H3K9me3 and H3K27me3) represses gene expression and marks heterochromatin regions [65,66]. Another important modification influencing gene regulation is direct DNA methylation, which involves addition of methyl group to cytosine residues, predominantly in CpG dinucleotides, catalysed by DNA methyltransferases (DNMTs). DNA methylation restricts TF biding and affinity, leading to reduced expression levels [67].

Epigenetic machinery is essential for supporting cell function and specialisation by controlling chromatin accessibility, transcription factor binding, and a precise regulation of gene expression. Better understanding of epigenetic alterations occurring in pathological condition of cancer, e.g. hypoxia, is fundamental for developing more effective therapeutic strategies.

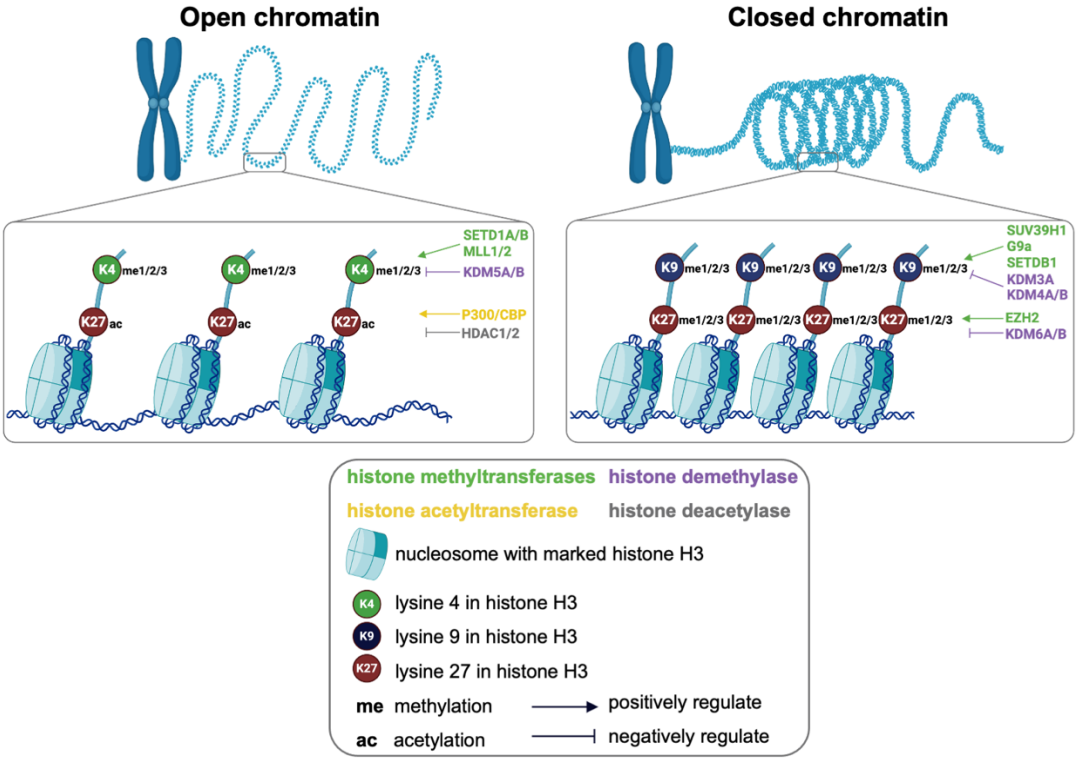


**Figure 1.4. Schematic representation of open chromatin with loosely packed nucleosomes (left) and closed chromatin with densely packed nucleosomes (right).** Examples of proteins regulating specific lysine residues in histone H3 are shown. Activating histone marks are introduced by HMTs (SETD1A, SETD1B), HDMs (KDM3A, KDM4A, KDM4B, KDM6A, KDM6B) and HATs (p300/CBP). In contrast, repressive histone marks are form by HMTs (SUV39H1, G9a, SETDB1 and EZH2), HDMs (KDM5A and KDM5B) and HDACs (HDAC1 and HDAC3) leading to heterochromatin formation. Positive and negative regulation of nucleosome structure is indicated by arrows or inhibitory lines, respectively. Graphics prepared with BioRender.com.

## 1.5. Hypoxia and epigenomic regulation

Growing evidence shows that hypoxia is a key factor significantly affecting the epigenetic landscape in cells. Several molecular mechanisms, by which hypoxia regulates different histone-modifying enzymes, have been identified. A widely studied mechanism involves Jumonji C (JmjC) domain histone lysine demethylases (KDMs), which function as oxygen-dependent hydroxylases [8,68–71]. Under hypoxic conditions, KDMs become inhibited, which results in the accumulation of methylation of various histone lysine residues, including H3K4me2/3 (a major target of KDM5A) or H3K27me2/me3 (a major target of KDM6A). This results in a global increase of histone methylation, changes in chromatin accessibility and dysregulation of gene expression [70,71]. A global increase in H3K9me3 is also observed under hypoxic condition. This effect may be associated with increased activity of histone lysine methyltransferases (KMTs) such as G9a or SETDB1, which under normoxic conditions may be targeted for degradation through oxygen-like

PHDs [72–74]. At the same time, the activity of H3K9-specyfic JmjC demethylases (KDM4A/B) may be reduced under hypoxia [74]. These alterations in histone mark have important functional consequences. For example, elevated H3K9me3 levels are required for the induction of ATM-mediated signalling during replication stress in hypoxic cells [75]. Moreover, hypoxia induced R-loop formation, which has been shown to further promote H3K9me2 deposition and contributing to both transcriptional and replication stress [76]. Finally, expression of some chromatin remodelling enzymes may be upregulated by HIF-1α activity, including KMTs such as EZH2, which methylates H3K27, as well as many KDMs. However, deprived oxygen still inhibits their enzymatic function, leading to an overall increase histone methylation under hypoxia [72]. In contrast, histone acetylation is globally reduced under hypoxic condition, primary due to decreased acetyl-CoA levels needed by HATs. Under the shortage of oxygen, the activity of PDK1 producing acetyl-CoA from glucose, is inhibited, leading to reduced acetyl-CoA availability and subsequently impaired chromatin acetylation. Moreover, several HDACs are positively regulated by hypoxia or directly by HIF-1α, including HDAC1/3/6/9, leading to a global chromatin deacetylation, and more condensed chromatin structure [77]. Hypoxia also reduces the activity of ten-eleven translocation (TET) dioxygenases responsible for the oxidation of 5-methylcytosine (5-mC) to 5-hydroxymethylcytosine (5-hmC) and subsequent DNA demethylation. As a result, promoter hypermethylation and transcriptional repression occur under hypoxic conditions [78].

Overall, hypoxia significantly alters the epigenetic properties of chromatin through multiple mechanisms, including dysregulation of expression of numerous chromatin modifying enzymes, as well as changing their activity due to limitations in the availability of particular metabolic cofactors. As a result, hypoxia-driven epigenetic reprogramming contributes to dynamic changes in transcriptional programs and eventual development of aggressive cancer phenotypes [79].

### 1.6. Facts about glioblastoma

Gliomas are primary brain tumours, which originate from neural stem cells or progenitor cells that carry genetic alterations responsible tumour development. Overall, the high-grade gliomas represent around 80% of all malignant brain tumours and, are diagnosed in approximately 6 out of 100,000 people worldwide [80,81]. Currently, according to the 2021 World Health Organization (WHO) classification of tumours of the central nervous system (CNS), gliomas are classified based on the histopathological

characteristics and molecular profile as grades1 - 4, with increasing malignancy from low to high grade [82]. The most frequent types of primary brain tumours in adult neuro-oncology practice are *"Adult-type diffuse gliomas"*, which are characterised by extensive, diffuse infiltrative growth of tumours cells into the brain parenchyma. Those tumours are divided primarily based on the presence of isocitrate dehydrogenase (IDH) mutations, and comprise three tumour types, including: IDH-mutant and 1p/19q-codeleted oligodendrogliomas (grade 2 and 3), IDH-mutant astrocytomas (grade 2-4) and IDH-wild-type glioblastomas (GBM) (grade 4) [82]. Tumours with IDH1/2 mutations cause production of oncometabolite 2-hydroxyglutarate (2-HG), resulting in changes in cancer cell metabolism and increased histone and DNA methylation, which affect the expression of many genes important for oncogenesis. Nevertheless, patients with IDH-mutant gliomas show better outcomes, compared to the patients with IDH-wild-type GBM [83].

GBM is the most aggressive and deadliest type of primary brain tumours, which constitutes more than a half of all malignant gliomas [82,84]. The high malignancy of GBM stems from pronounced cellular heterogeneity, driven by interplay of genetic, epigenetic and microenvironmental factors. Specifically, the emergence of single cell next-generation sequencing (NGS) methods enabled characterisation of four major cellular states in GBM, such as neural progenitor-like (NPC-like), oligodendrocyte progenitor-like (OPC-like), astrocyte-like (AC-like) and mesenchymal-like (MES-like) [85]. The MES-like state was further divided into hypoxia-independent (MES1) and hypoxia-dependent (MES2). The abundance of these states is associated with certain genetic alterations, including amplification of *CDK4* in NPC-like state, amplification of *PDGFRA* in OPC-like state, amplification of *EGFR* in AC-like state, and Chr5q deletions with *NF1* alterations in MES-like state [85]. These cellular states coexist within individual tumours and display remarkable plasticity, shifting in response to signals from highly heterogeneous TME [85,86]. Recent advances in single cells spatial transcriptomics and proteomics, and the integration of these datasets, have enabled a more detailed characterisation of cellular components within GBM [86,87]. The pioneering study by Greenwald et al. defined five-layer spatial organisation model that extends from a hypoxic/necrosis core, through hypoxia-driven angiogenesis and neurodevelopmental states, and ultimately, to infiltrated areas of brain tissue. Furthermore, hypoxia was identified as a central factor driving the multi-layered organisation of GBM [86]. The interplay between diverse tumour cell populations and the complex TME contributes to

the aggressive and invasive nature of GBM, and significantly limits the effectiveness of therapy [85–87].

The standard treatment for the patients newly diagnosed with GBM involves the maximal safe surgical resection followed by combined radiotherapy and chemotherapy with temozolomide, which cause DNA damage [81]. The efficiency of this drug depends on the status of O6-Methylguanine-DNA methyltransferase (MGMT), an enzyme that repairs the damage. Only patients with MGMT promoter methylation benefit from TMZ-based chemotherapy [88]. Nevertheless, despite the complex treatment, nearly all patients relapse resulting in an overall survival rate just beyond one year. Numerous clinical trials are ongoing, exploring new cytotoxic drugs, immunotherapies (including immune checkpoint inhibitors, monoclonal antibodies etc.), and targeted therapies. While these new approaches (and particularly combinatorial treatments involving immunotherapy) may bring some future therapeutic benefits, the results to date have not showed yet the significantly improved outcomes in patients [81,89].

### 1.7. Histological characteristics of glioblastoma TME

A key histological characteristic of GBM is the presence of necrotic regions with pseudopalisading areas and microvascular proliferation – both features are closely associated with malignancy and invasiveness of tumour cells [90]. Pseudopalisades are formed by densely packed, elongated and linearly arranged tumour cells that usually surround the necrotic areas (**Figure 1.5**). Pseudopalisades are thought to arise when the malignant glioma cells migrate away from the hypoxic and necrotic regions. Prolonged, severely hypoxic and low-glucose environment induces eventual cell death, which additionally stimulates the escape of the surviving cells that form invasive structures. These pseudopalisading cells subsequently contribute to the microvascular hyperplasia, by promoting the formation of dense, fragile and leaky blood vessels, driven by excessive expression of proangiogenic factors. In addition, hypoxia induces stem cell properties in tumours cells and affect the aspects of cellular homeostasis, further supporting the tumours growth and invasion, and making the GBM treatment a serious challenge [91,92].

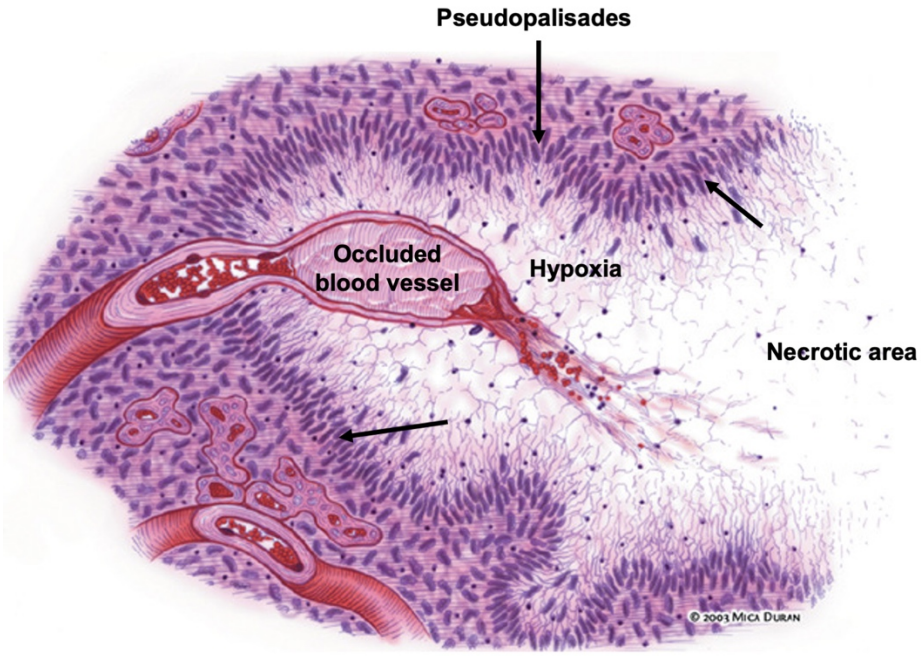


**Figure 1.5. Schematic illustration of pseudopalisading areas (arrows) in GBM.** Adapted from Brat et al. [93].

## 1.8. Characterisation of glioma-associated microglia/macrophages (GAMs)

The TME of GBM is highly heterogeneous and rich in multiple cell types that interact with tumour cells. While the most abundant are endothelial cells and innate immune cells, some fibroblasts were also reported to be present in GBM. These various stromal cells produce signalling factors and ECM molecules that together change the local microenvironment facilitating the tumour growth and infiltration into the brain [94]. Among these components, the most dominant non-neoplastic population are glioma-associated microglia/macrophages (GAMs), which can constitute from 30% to 50% of the tumours mass. Therefore, these myeloid cells have been extensively investigated, and proved to exhibit multiple phenotypes and functions [95].

GAMs arise from two distinct sources: microglia and bone marrow-derived monocytes/macrophages. Microglia are derived from the embryonic progenitors in the yolk sac, migrating to and residing within the brain parenchyma. These cells play an instrumental role in the brain development, function, maintenance of the CNS homeostasis, and limiting the excessive immune responses [96]. Under neuropathological conditions, including brain tumours, the integrity of the blood-brain barrier becomes compromised leading to entry of the peripheral innate immune cells, including monocytes [97]. Originating from the hematopoietic stem cells in the bone marrow, these cells enter

the bloodstream, circulate through peripheral tissues, and in response to the glioma-derived signals such as CC chemokine 2 (CCL2) or colony stimulating factor 1 (CSF-1), subsequently migrate into the glioma parenchyma, where they differentiate into tumour-associated macrophages [95].

The primary function of immune cells is to eliminate the tumour cells. However, glioma cells, through various stimuli, reprogram GAMs, which become supportive to tumour progression and evade the anti-tumour response [94]. GAMs secrete multiple immunosuppressive cytokines including interleukin 10 (IL-10), TGFβ or arginase 1 (ARG1), which may inhibit the cytotoxic response of T cells and NK cells. GAMs also secrete tumour-promoting factors, including epidermal growth factor (EGF), IL-6, MMP9 or VEGF, which support glioma cell proliferation, invasiveness or stimulate angiogenesis [98,99].

Both microglia and monocytes/macrophages are dynamic cell populations, that acquire distinct functional phenotypes, depending on the type of stimulus they encounter [98]. Similarly, as in other tumour types, GAMs were initially categorised into M1 and M2 macrophages. In such interpretation, the M1 macrophages are activated by damage-associated molecular pattern (DAMPs) or pathogen-associated molecular pattern (PAMPs) and exhibit pro-inflammatory activity or tumour-inhibitory functions, by secreting cytokines such as tumour necrosis factor (TNF-α), IL-1β, IL-12, nitric oxide, and ROS [100]. In contrast, the M2 macrophages, named as "alternatively activated" subtype, are induced by anti-inflammatory cytokines, such as, IL-4, IL-10 and IL-13 and overexpression of scavenger receptors (e.g. CD163), or mannose receptors (CD206) [95,98,100]. However, expression patterns of GAMs do not correspond to simplified phenotype of M1 and M2 macrophages. Instead, they exhibit highly complex and heterogeneous profiles, mirroring their remarkable functional plasticity [100]. Recent single-cell RNA sequencing and other high-resolution profiling approaches have characterised the detailed phenotypic and functional diversity of GAMs in both human GBM and experimental mouse glioma models. Using a comprehensive gene expression signature, GAMs are clustered and defined by characteristic molecular markers [101–104]. Different studies showed that, in terms of cellular origin, GAMs are divided into:

- microglia-derived GAMs (Mg-GAMs) based on the induced expression of genes such as *Tmem119*, *P2yr12*, *Sparc*, *Gpr34*, *Olfml3, etc;*

- monocyte/macrophage-derived GAMs (Mo/Mφ-GAMs) with increased expression of *Lgals3*, *Tgfbi*, *S100a11*, *S100a6* or *Ifitm2, etc*.

Within each Mg-GAMs and Mo/Mφ-GAMs groups, additional clusters can be found with predominant specialised phenotypic programs. Listed here are the distinct sets of top highly expressed molecular markers associated with each GAM phenotype (rather than an exhaustive list of genes found in each cluster):

- interferon-responsive GAMs (*Ifit1, Ifit3*, *Isg15,* etc*);*
- chemotactic GAMs (*Ccl2, Spp1, Rgs16,* etc);
- lipid-associated GAMs (*Ftl1, Lgals3, Apoe,* etc);
- phagocytic GAMs (*Cd83, H2-Aa, Cd69,* etc);
- hypoxic GAMs (*Adm, Bnip3l, Ero1a,* etc);
- ribosomal GAMs (*Rpl13, Rpl19, Rps15,* etc);
- transitional GAMs (*Ly6c2, Plac8, S100a6,* etc).

Although these states exhibit some degree of functional specialisation, the majority of GAMs subpopulations contribute to GBM progression and the establishment of an immunosuppressive microenvironment [101]. Moreover, myeloid markers that are broadly expressed across GAM subtypes can be modulated by environmental factors (like hypoxic stress), raising concerns about the reliability of using them as single markers to identify particular GAM populations in approaches such as immunohistochemistry [100].

### 1.9. Hypoxia and GAMs

In GBM, the spatial distribution of immune cells within the TME is highly complex, with Mg-GAMs and Mo/Mφ-GAMs occupying distinct localisations. Mg-GAMs are enriched both at the tumour tissue and the surrounding brain parenchyma. On the contrary, most of the Mo/Mφ-GAMs are present in the tumour core and perivascular niches, due to infiltration from the leaky blood vessels [101,103,105].

GBM is highly hypoxic, and therefore GAMs located within the tumour core are frequently exposed to oxygen shortages [106,107]. Such persistent hypoxic stress can profoundly influence their phenotype by driving specific gene expression allowing adaptation to these metabolically challenging conditions [10]. Advances in single cell transcriptomics, spatial transcriptomics and proteomics recently enabled high-resolution, single-cell mapping of GAMs within TME [86,87,108]. As described above, Greenwald et al. defined the five layers in the organised GBM structure, in which hypoxic stress emerges

as a key force shaping this spatial architecture of layers. In the context of Mg and Mo/Mφ, it was shown that inflammatory GAMs localise preferentially to oxygen-deprived niche (hypoxia-associated layer), co-exist with mesenchymal-hypoxic tumours cells and exhibit more immune-suppressive phenotypes. Following this layer, there is a region enriched in myeloid cells that interact with T cells and vascular cells, collectively compensating for oxygen deprivation through the formation of complex immune-vascular response [86]. Accumulation of GAMs in the hypoxic and/or necrotic regions of GBM may be driven by increased level of chemoattractants by tumour cells. For instance, hypoxia induces expression of VEGF, semaphorin 3A (SEMA3A) or stromal cell-derived factor 1α (SDF1α), which all are known as the migratory stimulating factors for macrophages [54]. Once GAMs enter hypoxic regions, upregulation of other factors is triggered, including the chemokine CCL8 and the cytokine IL-1β, which enhance the recruitment of additional GAMs. Upon becoming entrapped within hypoxic areas of GBM, these cells acquire immunosuppressive and immunotolerant phenotypes [107]. Additionally, it was shown that hypoxia-altered GAMs destabilise endothelial adhesion junctions through the secretion of adrenomedullin, leading to the formation of highly permeable blood vessel [103]. Authors showed that inhibiting adrenomedullin, either genetically or with inhibitors, reverses this effect and restores the normal vascular structure, which may enhance therapeutic drug delivery [103]. A recent study discovered a new GAM subpopulation characterised as lipid-laded macrophages (LLM). LLMs accumulate in hypoxic niches and are characterised by altered metabolism. The LLMs become lipid-rich through the accumulation of myelin derived cholesterol, promote immunosuppressive phenotypes and drive the malignant progression of glioma cells [109].

Overall, those data suggest that hypoxia affects GAM phenotypes and, plays a prominent role in the GBM progression and therapeutic failure. However, how hypoxia reprograms different GAMs subpopulations and whether these changes are driven by epigenetics mechanisms remains poorly understood.

# 2. Aims

Hypoxia is an important intratumoral stress which may induce tumour aggressiveness and therapy resistance. Many studies have shown that hypoxia influences the chromatin landscape, especially by changing the histone PTMs. However, how this epigenetic regulation can affect the transcriptome and functions of glioma TME, and particularly GAMs, has not been fully elucidated. Therefore, **the main aim of this work was to understand the epigenomic, transcriptomic and phenotypic changes induced by hypoxic stress within the TME of glioblastoma and how these contribute to the interactions between glioma and microglia cells.**

The specific aims were as follows:

1. To characterise the genome-wide chromatin changes in glioma cells induced by hypoxic stress.
2. To optimise the direct oxygen-dependent co-culture model of glioma and myeloid cells that reliably reflects the *in vivo* interactions.
3. To precisely dissect transcriptomic changes in myeloid cells dependent on hypoxic stress and on interactions with glioma cells.
4. To assess the chromatin accessibility changes in myeloid cells exposed to hypoxia and compare these with gene expression.
5. To validate the links between hypoxia-induced epigenetic and transcriptomic changes, and phenotypes displayed by myeloid cells.

# 3. Materials and Methods

## 3.1. Cell culture

The murine BV2 microglia cell line (provided by Prof. Klaus Reymann from Leibniz Institute for Neurobiology) and the murine RAW 264.7 macrophage cell line (Biological Resource Center ICLC Cell bank, #ICLC ATL02001, in collaboration with Dr hab. Anna Malik, Cellular Neurobiology Research Group, University of Warsaw) were cultured in Dulbecco's Modified Eagle Medium (DMEM) with GlutaMAX™ (Gibco™, #31966047), supplemented with 2% and 10% fetal bovine serum (FBS, Gibco™, #16000044), respectively. Bone marrow-derived macrophages (BMDMs) were isolated and differentiated from monocytes to BMDMs by Mr Tomasz Obrębski (Cellular Neurobiology Research Group, University of Warsaw) by culturing in DMEM with GlutaMAX™, 10% FBS and 30 ng/mL M-CSF (Gibco, #315-02-10UG) and replacing with fresh medium (containing 10% FBS and 30 ng/mL M-CSF) on day 3, 5 and 7. Hypoxic exposure was conducted on day 10 of the monocyte to BMDM differentiation. GL261 mouse glioma cells stably expressing pEGFP-N1 or tdTomato, as well as HCT116 human colorectal carcinoma cells, were cultured in DMEM (Gibco™, #11885084) with 10% FBS. All culture media were additionally supplemented with antibiotics (100 U/mL penicillin, 100 µg/mL streptomycin, Gibco™, #10378016). Cell cultures were maintained in a humidified incubators supplied with 5% $CO_2$ at 37°C. The regular mycoplasma tests were carried out in all cells used.

## 3.2. Hypoxic conditions and drugs treatment

To create hypoxic conditions, cells were incubated at <0.1 or 1% $O_2$ in a humidified hypoxic chamber (M35 Hypoxystation, Don Whitley) in the presence of 5% $CO_2$ at 37 °C for 16 hours. As an alternative, hypoxic conditions were mimicked by treating cells with 250 µM cobalt chloride ($CoCl_2$) under normoxic conditions (21% $O_2$). For panobinostat treatment under hypoxic conditions, cells were exposed to <0.1% $O_2$ and incubated with 10 nM panobinostat or an equivalent volume of DMSO for 16 hours.

## 3.3. Direct co-culture assay

GL261 cells were initially seeded in DMEM supplemented with 10% FBS and antibiotics. After 24 hours, either BV2 cells or BMDMs were added to GL261 cultures at a ratio of 1:2 (BV2:GL261) or 1:1 (BMDM:GL261), respectively. Co-cultures were

maintained in DMEM with GlutaMAX™ supplemented with 2% FBS for BV2 cells or with 10% FBS and 10 ng/mL CSF-1 for BMDMs. Following 24 hours of co-culture, the cells were exposed to hypoxic conditions (<0.1% $O_2$) or maintained under normoxia for another 16 hours and used in further assays. Control BV2 or BMDM cells were cultured as monocultures and exposed to hypoxia or normoxia for 16 hours (**Figure 3.1**).

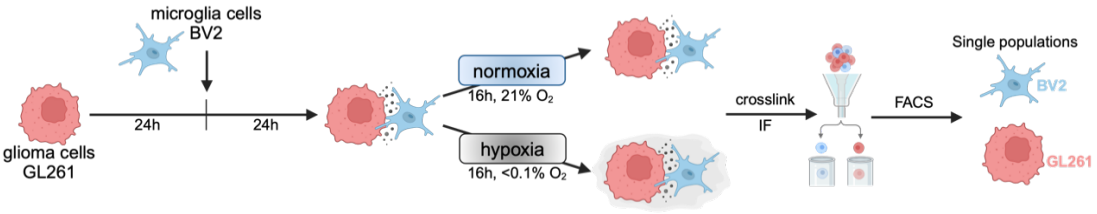


**Figure 3.1.** A scheme summarising direct glioma-microglia co-culture experiment. IF – immunofluorescence; FACS – fluorescence-activated cells sorting. The scheme shows co-culture of BV2 cells with GL261 cells; the co-culture of BMDMs with GL261 was performed in an analogous way.

### 3.4. Immunoblotting

Cells were washed in PBS and lysed in sodium dodecyl sulfate (SDS) lysis buffer (10 mM Tris-Cl, pH 7.5, 0.1 mM ethylenediaminetetraacetic acid (EDTA), 0.1 mM ethylene glycol-bis (β-aminoethyl ether)-N,N,N′,N′-tetraacetic acid (EGTA), 0.5% SDS, 0.1 mM β-mercaptoethanol, protease/phosphatase inhibitors), followed by sonication at 4°C using a Bioruptor Pico (Diagenode) at ultra-high power settings (30 s ON and 30 s OFF, 6 cycles). The sonicated cells were centrifuged at 4 °C for 15 min at 14000 x g and the supernatant was transferred to a new tube. The protein concentration was determined using NanoDrop™ spectrophotometer. Total protein extracts were prepared in 2x SDS sample-loading buffer (100 mM Tris-Cl, pH 6.8, 4% (w/v) SDS, 20% (v/v) glycerol, 2% (v/v) β-mercaptoethanol, 25 mM EDTA, 0.04% (w/v) bromophenol blue) and denatured for 5 min at 95 °C. Lysates with equal amounts of proteins were subjected to SDS-PAGE and western blotting using Trans-Blot Turbo Transfer System (Bio-Rad). After blocking with 5% non-fat milk in TBST (20 mM Tris-buffered solution pH 7.5, 150 mM NaCl, 0.1% Tween-20), the membranes were incubated overnight with primary antibodies (**Table 3.1**) diluted in 3% BSA in TBST 1:1000 or incubated for 1 hour with a horseradish peroxidase (HRP)-conjugated anti-β-actin antibody in 5% non-fat milk in TBST. Following three washes with TBST, the membranes were incubated with HRP-conjugated secondary antibodies for 1 hour at room temperature (RT). After the final washes with TBST, an enhanced chemiluminescence detection system (ECL) and

Chemidoc Imaging System (BioRad) were used to develop the signal from HRP-conjugated secondary antibodies.

**Table 3.1. List of antibodies used for Western blot.**

| Antibody | Company | Cat. number |
|---|---|---|
| DDX5 | Sigma | Pab204 |
| DHX9 | Abcam | ab26271 |
| Cleaved Caspase-3 | Cell Signalling | 9661 |
| Cleaved Caspase-7 | Cell Signalling | 9491 |
| HIF-1α | Abcam | ab179483 |
| H3K4me3 | Millipore | 07-473 |
| H3K9me3 | Millipore | 07-442 |
| H3K27me3 | Millipore | 07-449 |
| H3K27ac | Cell Signalling | 8173S |
| H3ac | Millipore | 06-599 |
| H3 | Abcam | ab1791 |
| LGALS3 | Abcam | ab53082 |
| PARP | Cell Signalling | 9542 |

### 3.5. Immunofluorescence on xenograft sections

Orthotopic mouse GL261 glioma growth was conducted under the protocol approved by the Local Ethics Committee for Animal Experimentation at the Nencki Institute of Experimental Biology in Warsaw (project license 1019/2020). Mice were fed with standard chow ad libitum and kept under standard day/night conditions. Male C57BL/6 mice (12 weeks) were anesthetised with 4% isofluorane and maintained at 1.5% isofluorane in oxygen during the tumour implantation procedure. After performing 1 cm longitudinal skin incision a hole was drilled with a micromotor drill at the following 1 mm anterior-posterior, -2 mm lateral and -3 mm dorsal-ventral in relation to bregma. Next, using syringe with a 26-gauge needle in a stereotactic apparatus Luc+tdT+ GL261 glioma cells (8 x $10^4$ cells in µL of DMEM) were implanted under aseptic conditions into the right striatum at the rate of 0.25 µL/min. Once the injection of cells finished, the needle was slowly retracted at the speed of 1 mm/min. After 25 days of post-implantation, animals were intraperitoneally injected with 60 mg/kg of Pimonidazole (Hypoxyprobe™-1, #HP2-200) and 2 hours later were anesthetised, sacrificed, and perfused with ice-cold PBS and subsequently with 4% paraformaldehyde (PFA) in PBS. Brains with tumours were then removed and fixed additionally with 4% PFA in PBS for

24 hours at 4°C, followed by immersion in 30% sucrose for 48 hours at 4°C and mounting in a tissue freezing medium (Leica, #14020108926) on dry ice. Coronal sections 10 μm in size were collected using a cryostat and stored at -80°C. Tissue sections were subjected to an antigen retrieval with 10 mM sodium citrate buffer (pH 6.0) for 15 min at 96°C. Then, autofluorescence was quenched with 50 mM $NH_4Cl$ in PBS for 20 min, followed by a wash with PBS and blocking in PBS containing 10% donkey serum (DS) and 0.1% Triton X-100 solution for 2 hours. Subsequently, sections were incubated overnight at 4 °C with anti-pimonidazole antibody conjugated with FITC or Pacific Blue (1:100, Hypoxyprobe™-1, #HP2-200), anti-GLUT1 (1:300, Proteintech, #21829-1-AP) or anti-DDX5 (1:200, Abcam, #ab126730) antibodies diluted in 0.1% Triton X-100/PBS solution and 3% of donkey serum. The next day, sections were washed in PBS and incubated with donkey anti-rabbit IgG conjugated with Alexa Fluor™ 555 (1:1000, Invitrogen, #A31572) or with Alexa Fluor 647 (1:1000, Invitrogen, #A-31573) for 2 hours at RT. Nuclei were counter-stained with DAPI (0.1 mg/mL) for 10 min and after washes in PBS, tumour sections were mounted with mounting medium (Dako, #S3023). Images were acquired using a Zeiss LSM800 confocal microscope (40x objective).

### 3.6. Immunofluorescence staining of histone modification

Cells were seeded on glass coverslips in 24-well plates following the procedure as described in the direct co-culture section (3.3). After incubation in hypoxic or normoxic conditions cells were washed with PBS and fixed with 4% PFA for 10 min. Following fixation, cells were washed with PBS, permeabilized with ice-cold 100% methanol for 10 min, and washed with PBS. Next, cells were blocked with blocking buffer (3% DS, 1% BSA, 0.3% Triton X-100 in PBS), then stained either with H3K9me3 (1:500, Millipore, #07-442) or H3K27me3 antibody (1:500, Millipore, #07-449) diluted in a blocking buffer for 1 hour. After three washes with PBST (0.1% Tween 20 in PBS), cells were incubated for 1 hour with a secondary donkey anti-rabbit antibody conjugated with Alexa Fluor-555 (1:2000, Invitrogen, #A31572) diluted in a blocking buffer. Coverslips were then washed three times with PBST, stained with DAPI (1 μg/mL, Sigma, #D9542) for 10 min, washed twice with PBS and rinsed in distilled water. Finally, coverslips were mounted on glass slides using a mounting solution (Dako, #S3023). Images were captured on Leica DM4000B (40x objective). Fluorescence intensity of H3K9me3 and H3K27me3 staining was assessed for three independent experiments and calculated using ImageJ.

### 3.7. Phalloidin staining for F-actin visualisation

Cells were seeded on glass coverslips in 24-well plates following the procedure described in section 3.3. After incubation in hypoxic or normoxic conditions cells were washed with PBS and fixed with 4% PFA for 10 min. Fixed cells were then permeabilized with 0.1% Triton X-100 for 5 min and subsequently washed with PBS. F-actin was stained using Phalloidin - Tetramethylrhodamine B isothiocyanate (1:500, Sigma, #P1951) for 30 min at RT, followed by 10 min nuclear staining with DAPI (1 μg/mL, Sigma, #D9542). Coverslips were then washed twice with PBS, rinsed with distilled water and mounted on glass slides using a mounting solution (Dako, #S3023). Images were acquired using fluorescence microscope Zeiss 800 microscope (40x objective).

### 3.8. BODIPY staining for lipid droplet visualisation

BV2 or BMDM cells were seeded on glass coverslips in 24-well plates and the following day, exposed to hypoxia (<0.1% $O_2$) or maintained under normoxic conditions for 16 hours. Cells were then washed with PBS and fixed with 4% PFA for 10 min. After two PBS washes, cells were permeabilised with 0.3% Triton X-100 for 10 min, followed by a double wash with PBS and a 50 min incubation with 50 μM BODIPY 493/503 solution in PBS (Molecular Probes, #D3922). Coverslips were washed three times with PBS and stained with DAPI (1:1000) for 10 min. This was followed by two PBS washes, a rinse in distilled water and mounting on slides using a mounting solution (Dako, #S3023). For each condition, five Z-stack images were collected from three independent experiments using fluorescence microscope Zeiss 800 microscope (40x objective). The number of lipid droplets (LDs) per cell, total LDs volume per cell, and total LDs fluorescence per cell (calculated as a sum of LD volume × LD mean intensity for all detected droplets in a cell) were quantified using Imaris software. Data are shown as mean ± standard deviation (SD) from all cell measurements. Statistical significance was determined using an unpaired t-test.

### 3.9. CODEX Multiplex Immunofluorescence Staining

A patient-derived glioma tissue microarray (TMA, GL806f198, from Tissue Array) was processed and stained using the PhenoCycler-Fusion system (Akoya Biosciences), according to manufacturer's FFPE protocol. In brief, TMA sections were deparaffinized in xylene and rehydrated through a graded ethanol series (100%, 90%, 70%, 50% and 30%) to water, with 5 min incubations at each step. Tissue sections were

then subjected to an antigen retrieval using AR9 Akoya Buffer for 20 min under high pressure in a pressure cooker. Following this, the tissues were washed twice with Akoya Hydration Buffer (2 min each) and equilibrated for 30 min in Akoya Staining Buffer. The sample slides were then stained in Akoya Blocking Buffer with a panel of antibodies, including pre-conjugated antibodies from Akoya Biosciences: DAPI (#7000003), CD31 (#4450017) - BX001 - AF750 (1:200), CD45 (#4550121) - BX021 - AF647 (1:200), CD68 (#232176) - BX015 - AF647 (1:200). Additional markers were stained using custom-conjugated antibodies, prepared with Akoya Biosciences conjugation kit (#232195): GLUT1 (Abcam, #ab252403) - BX054 - Atto 550 (1:500), TMEM119 (Cell Signaling, #83308) - BX027 - AF647 (1:500), GPNMB (R&D Systems, #AF2550) - BX032 - AF750 (1:200), and LGALS-3 (BioLegend, #125401) - BX040 - AF750 (1:200). After 3 hours of staining at RT, slides were washed twice with Akoya Staining Buffer (2 min each). FFPE tissues were then sequentially fixed with 16% PFA (10 min, RT), ice-cold methanol (10 min, 4°C), and the Akoya Fixative Reagent (20 min, RT) to stabilise antibody-antigen complexes and prepare samples for cyclic staining. Between each fixation step, slides were washed three times with fresh PBS. After post-fixation, the stained TMA slides were assembled into a flow cell and imaged using PhenoCycler-Fusion system.

### 3.10. Phagocytosis assay

BMDM cells were seeded on glass coverslips in 24-well plates. The next day, red fluorescent latex beads (Sigma-Aldrich, #L3030) were added at a 1:50 cell-to-bead ratio, and cells were then subjected to either hypoxia (<0.1% $O_2$) or maintained under normoxic conditions. Lipopolysaccharide (LPS, 100 ng/mL) was used as a positive control. Following 16 hours, cells were gently rinsed twice with PBS and then fixed with 4% PFA for 10 min. Phagocytic activity was assessed by fluorescence microscopy in 15 randomly chosen fields and classified as low (>2 beads/cell), medium (≥2 and <10 beads/cell), or high (≥10 beads/cell).

### 3.11. Fluorescence-activated cell sorting (FACS) of cell co-cultures

GL261 co-cultures with BV2 or with BMDM cells were proceed as described below in section 3.12.1, 3.16.1 or 3.17.1. Subsequently cells were washed with PBS and incubated in 3% bovine serum albumin (BSA) (Sigma, #A7906) with CD16/CD32 Fc Block™ (1:250, BD Pharmingen, #553142) in phosphate-buffered saline (PBS)

for 15 min at RT. Next, the anti-CD45-PE antibody (Clone 30-F11, 1:400, BD Pharmingen, #553081) was added in blocking buffer and incubated for 40 min at RT followed by washes with PBS. Cell pellets were then resuspended in 300 µL 1% BSA in PBS and cell suspensions were filtered through 35 µm sterile filter into 5 mL polystyrene round bottom tubes. CD45+ or GFP+ cells were sorted into 15 mL tubes pre-coated with 1% BSA in PBS using Cell Sorter BD FACSAriaII at the Laboratory of Cytometry. Briefly, fluidics startup was performed, and the nozzle was set to 85 µm. Next, the stream was turned on, and the amplitude was adjusted until the breakoff drop was in an optimal position. Cytometer Set-Up and Tracking (CST) was run to check cytometer performance using CS&T beads (BD Biosciences, #655051). Drop delay was calibrated using BD FACS™ Accudrop Beads (BD Biosciences, #345249). After establishing a stable stream and accurately setting the drop delay, the side streams were adjusted to collect the desired population. Gates for sorting were set for CD45-postive events as BV2 cells or BMDMs and GFP-positive events as GL261 cells (**Figure 3.2**). After sort, samples were immediately placed on ice, and cells used in downstream applications.

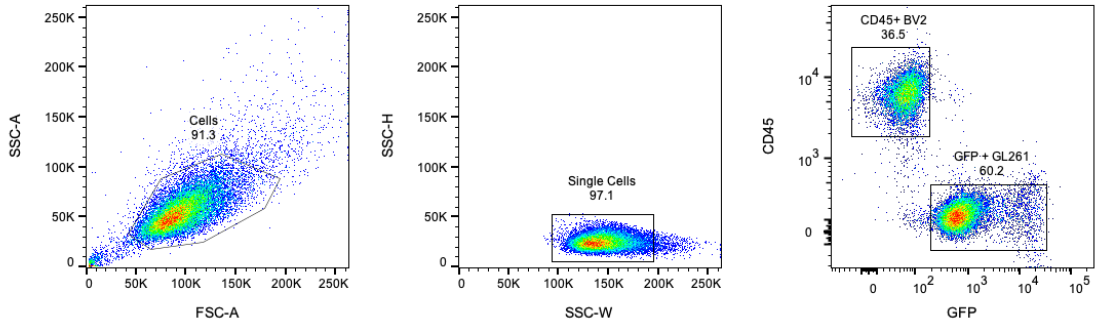


**Figure 3.2.** Gating strategy for the flow cytometric sorting of BV2 CD45+ cells and GL261 GFP+ cells.

## 3.12. Assay for Transposase-Accessible Chromatin using sequencing (ATAC-seq)

### 3.12.1. Cells fixation with formaldehyde and FACS

Cells were washed with PBS and detached from cell culture plates with Tryple (Gibco, #12604013) for 2-3 min at 37 °C. Next, cells suspensions were transferred to 1.5 mL Eppendorf tubes and centrifuged. After discarding the supernatant, pellets were resuspended and fixed in 1% formaldehyde (Sigma, #F8775) for 10 min at RT. Hypoxia-treated cells were processed in the hypoxia chamber up to this point. Next, cells were quenched with glycine (final concentration 0.125 M) for 5 min at RT, centrifuged at

500 x g for 5 min, and washed twice with PBS. Finally, cells were stained and sorted as described in section 3.11.

### 3.12.2. Cell lysis and transposition

ATAC-seq was performed as previously described with some modifications [110]. Cells were counted using the haemocytometer and 50,000 cells were lysed in 50 µL ice-cold lysis buffer made with 10 mM Tris-HCl, pH 7.4, 10 mM NaCl, 3 mM MgCl2 and 0.1% IGEPAL CA-630 (Sigma, #I8896) for 5 min on ice. Cells were then centrifuged at 500 x g for 8 min at 4 °C, and cell pellets were resuspended in transposition reaction mix consisting 25 µL TD buffer (Illumina, #20034198), 2.5 µL Nextera Tn5 Transposase (Illumina, #20034198) and 22.5 µL nuclease-free $H_2O$. Transposition reactions were incubated for 30 min at 37°C in thermoblock set to 300 x rmp. After this time, reaction was stopped by adding 8 µL of 0.5 M EDTA. Cells were subsequently centrifuged and reverse crosslinked overnight at 65°C with shaking (1200 rpm) in buffer containing 50 mM Tris-Cl, 1 mM EDTA, 1% SDS, 0.2 M NaCl, 200 µg/mL proteinase K (Thermo Scientific, #EO0491). Transposed DNA was purified with Zymo DNA Clean & Concentrator-5 columns (ZymoResearch, #D4014) and eluted in 10 µL of nuclease-free $H_2O$. Purified DNA was stored at -20°C.

### 3.12.3. PCR Amplification

To amplify DNA fragments PCR reaction was performed using 10 µL transposed DNA, 10 µL nuclease free $H_2O$, 2.5 µL each of 25 µM Custom Nextera PCR Primer 1 and Primer 2 (with sequences as described by Buenrostro et al. [111]), and 25 µL NEBNext High-Fidelity 2x PCR Master Mix (New England Biolabs, #M0541L). Thermal cycle settings for a PCR are given in the **Table 3.2**.

**Table 3.2.** Thermocycler settings for pre-amplification during ATAC-seq library preparation.

| Step | Temp | Duration | Cycle |
|---|---|---|---|
| Pre-warming | 72 °C | 5 min | |
| Initial denaturation | 98 °C | 30 s | |
| Denaturation | 98 °C | 10 s | 5 |
| Annealing | 63 °C | 30 s | |
| Extension | 72 °C | 1 min | |
| Hold | 4 °C | ∞ | |

To avoid overamplification, the optimal total number of PCR cycles for each sample was established using quantitative PCR (qPCR). To do this, qPCR was performed with the 5 µL of DNA amplified during initial 5 cycles as in Table 3.2, 4.41 µL nuclease free $H_2O$, 0.25 µL Custom Nextera PCR Primer 1 and 0.25 µL Custom Nextera PCR Primer 2, 0.9 µL 10x SYBR Green I (Applied Biosystems, #4385610) and 5 µL NEBNext High-Fidelity 2x PCR Master Mix. Thermal cycle settings for a qPCR are given in the **Table 3.3**.

**Table 3.3.** Thermo-cycling profile for qPCR.

| Step | Temp | Duration | Cycle |
|---|---|---|---|
| 1 | 98 °C | 30 s | |
| 2 | 98 °C | 10 s | 20 |
| 3 | 63 °C | 30 s | |
| 4 | 72 °C | 1 min | |

The additional number of cycles needed for each sample was calculated by plotting linear Rn (normalised reporter signal, which represents the fluorescence signal from the reporter dye divided by the fluorescence signal from a passive reference dye) against the cycle number and determining the cycle at which the fluorescence reached ¼ of the maximum intensity. The remaining 45 µL of the initial PCR reaction was run according to this value and then amplified libraries were purified with Zymo DNA Clean & Concentrator-5 columns (ZymoResearch, #D4014). AMPure XP beads (Beckman Coulter, #A63881) were used for the size selection to remove primer dimers and fragments over 1000 bp. The quality of purified libraries was assessed using Bioanalyzer 2100 and Bioanalyzer High Sensitivity DNA Analysis kit (Agilent, #5067-4626). The libraries were sequenced in paired-end mode (2 x 76 bp for GL261 cells experiment and 2 x 151 bp for co-culture experiment) using NovaSeq 6000 (Illumina, San Diego, CA, USA) at the Laboratory of Sequencing (Nencki Institute). Two independent biological replicates were analysed per each condition.

### 3.12.4. ATAC-seq data processing

The quality of raw fastq data was evaluated using FASTQC software (https://www.bioinformatics.babraham.ac.uk/projects/fastqc/). Reads were trimmed using Trimmomatic (version 0.36) to remove Illumina-specific adapters and transposase

sequence, short reads and low quality 5' and 3' bases [112]. Then, paired-end reads were aligned to mouse genome (mm10) using bowtie2 aligner (version 2.2.5) with parameters -very sensitive and -X2000 or Hisat2 aligner (version 2.1.0) with parameters -X 2000 [113,114]. Duplicate reads were subsequently identified and removed using Picard Tools 'MarkDuplicates' (http://picard.sourceforge.net) and reads aligned to the mitochondrial genome were also excluded. Only properly paired and uniquely mapped reads were kept for downstream analysis using samtools view with the options -q 30 -f 2 -F 256. Peaks were called using MACS2 (version 2.1.1.2) with parameters set to -f BAPME -q 0.01 –nomodel –shift 0 [115]. The obtained peaks were then filtered for peaks overlapping mm10 ENCODE blacklisted genomic regions. All sequencing tracks were visualised in Integrative Genome Viewer (IGV) using normalised bigWig files, which were generated with deepTools 'bamCoverage' and normalised to genome coverage using the RPGC (Reads Per Genomic Content) method [116,117].

### 3.12.5. Differential analysis of ATAC-seq peaks

Changes in chromatin accessibility were assessed using DESeq2 or edgeR packages in R (version 4.2.2, https://www.r-project.org/) [118,119]. To create a set of consensuses ATAC-seq peaks for the read count matrixes, the following steps were performed. First, peaks for two replicates in each condition were intersected and only peaks with overlap > 200 bp were included. Then, obtained peaks from all conditions were merged with reduction of overlapping regions using the 'reduce' function from the GenomicRanges package, resulting in the generation of consensus peak lists. A matrix of fragment counts within peaks was generated from BAM files using getCounts function in the ChromVar package [120,121]. Peaks with FDR < 0.05 (Benjamini and Hochberg - corrected P-value) and |log2 fold change| >= 0.6 were classified as significantly different.

### 3.12.6. Annotation for differential ATAC-seq peaks to genomic features

The peaks were annotated to genomic features using ChIPseeker, with the promoter region defined as +/- 2,000 bp from the transcription start site (TSS) and the overlap parameter set to 'all' to annotate peaks to the nearest gene. Each peak was annotated to only one genomic feature according to the default annotation priority in ChIPseeker [122]. To assign promoter peaks to all possible genes, a custom-written script in R was used based on biomaRt and GenomicRanges packages. Functional enrichment

analysis of differentially accessible regions nearby genes was performed using enrichGO function from clusterProfiler [123]. Revigo and Cytoscape tool was used to merge redundant GO terms and visualise them, if mentioned [124,125]. Motif enrichment analysis for selected ATAC-seq peaks was performed using HOMER findMotifsGenome.pl (http://homer.ucsd.edu/homer/motif/) for known TFs motifs from HOMER custom database with the option -size given [126]. For local motif analysis in ATAC-seq peaks, FIMO from the MEME suite was used [127]. Enriched motifs shown in figures were filtered to include only those motifs with q-value < 0.01 and where the expression of the transcription factor gene was sufficiently high, defined as a sum of the log2-transformed CPM values across the samples of at least 2.

### 3.13. Chromatin immunoprecipitation (ChIP) with qPCR

The ChIP protocol was adapted from Cook et al., with minor modifications [128]. HCT116 cells were exposed to hypoxia (<0.1% $O_2$) or normoxia for 16 hours. Cells were detached using TrypLE, washed with PBS and subsequently fixed with 1% formaldehyde (Sigma, #F8775) for 10 min at RT. Next, cells were quenched with 0.125 M glycine for 2 min on ice, centrifuged (200 x g, 5 min, 4 °C), washed twice with PBS containing protease inhibitors (Roche, #11836170001), and frozen at –80 °C. For ChIP, $2\times10^6$ cells per condition were lysed with ice-cold buffer (0.32 M sucrose, 15 mM HEPES, pH 7.9, 60 mM KCl, 2 mM EDTA, 0.5 mM EGTA, 0.5% (w/v) BSA, 0.5 mM DTT, protease inhibitors cocktail) and incubated for 20 min on ice. Subsequently nuclei isolated by Dounce homogenization (20 strokes) followed by sucrose gradient in buffer A+ (1.3 M sucrose, 15 mM HEPES, pH 7.9, 60 mM KCl, 2 mM EDTA, 0.5 mM EGTA, 0.5% (w/v) BSA, 0.5 mM DTT, protease inhibitors cocktail). After 5 min of centrifugation at 1000 x g and 4 ºC, nuclear pellets were washed two times with buffer W (10 mM Tris·Cl, pH 7.4, 15 mM NaCl, 60 mM KCl, protease inhibitors cocktail), pelleted by 350 x g centrifugation for 4 min at 4 ºC and resuspended in buffer W supplemented with final 1.2 mM $CaCl_2$. Next, chromatin was digested with micrococcal nuclease (MNase, 15 U, 25 °C, 25 min, 1000 rmp shaking) and then reaction was stopped by adding EDTA and EGTA to final concentration 2.6 mM. Next the chromatin was solubilised with final 0.06% SDS, and diluted in LB3 buffer (1 mM EDTA, 10 mM Tris·Cl, pH 7.5, 1% (w/v) sodium deoxycholate, 0.5% (w/v) sarkosyl, 1% (v/v) Triton X-100). After centrifugation, 200 µL of lysate was set aside as input, and 2000 µL was incubated overnight at 4 °C with 4 µg of one of the following antibodies: H3 (Abcam, #ab1791),

H3K27ac (Cell Signaling, #8173), or control rabbit IgG (Cell Signaling, #2729S). The next day, protein A/G beads were added (2 h, 4 °C), followed by wash steps and chromatin elution. After reverse crosslinking of eluted DNA, RNase A and Proteinase K digestion, DNA was extracted with 25:24:1 (v/v/v) phenol/chloroform/isoamyl alcohol reagent, precipitated from the aqueous phase with 3 volumes of 100% ethanol, 0.1 volume of 3 M sodium acetate, and 1 uL of glycogen. DNA was subsequently purified using Zymo DNA Clean & Concentrator-5 columns (ZymoResearch, #D4014). DNA fragment sizes (100–1000 bp) were assessed using TapeStation system (High Sensitivity D1000 ScreenTape Assay, Agilent). Input and ChIP DNA were analyzed by qPCR using Fast SYBR Green Master Mix (Applied Biosystems, #4385612) on a QuantStudio 12K Flex system. Primers were used for DDX5 promoter locus (forward primer: ATGTTCCTTCGTCTGCCTCGA, reverse primer: CTTGCTTTTTGTGTGGGGATT) and DDX5 gene body locus (forward primer: TGAAAACACTGCCTGCATTTT, reverse primer: AATTGCAGAAATGACTGCAGT). Percent of input was determined for total H3, H3K27ac and IgG control IP samples (2^- (sample Ct– adjusted input Ct)). Fold enrichment for H3K27ac and IgG was determined relative to H3. Results represent mean ± SD from three biological replicates. Statistical significance was calculated with Student's t-test.

### 3.14. RNA extraction

Total RNA was extracted using RNeasy Mini Kit (Qiagen, #74104) according to manufacturer's protocol followed with QIAshredder column (Qiagen, #79654) and DNase digestion step (Qiagen, #79254). RNA was eluted in 30 µL of high-purity nuclease free water, and quantity and quality of isolated RNA was assessed using NanoDrop 2000 Spectrophotometer (Thermo Fisher). Samples were stored at -80 °C.

### 3.15. Reverse Transcription Quantitative Polymerase Chain Reaction (RT-qPCR)

200-500 ng of total RNA, 1 µL of 50 µM oligo$(dT)_{15}$, 1 µL 50 µM of random hexamer (Invitrogen™, #N8080127), 1 µL of 10 mM dNTPs mix (Promega) and sterile RNase-free water were mixed into a final volume of 12 µL. The mix was incubated at 65°C for 5 min and placed immediately on ice. Master mix containing 4 µL 5X First-Strand Buffer, 1 µL of 0.1M DTT, 0.5 µL SuperScript IV Reverse Transcriptase (200 U/µL, Invitrogen™, #18090050) and 2.5 µL sterile RNase-free water was added to the mRNA mix. cDNA synthesis was then carried out for 10 min at 50 °C, and enzyme

inactivation for further 10 min at 80°C. The obtained cDNA was then diluted 1:10 and used as a template for the quantitative PCR (qPCR) with 5 µL SYBR Green detection reagents (Fast SYBR™ Green Master Mix, Applied Biosystems, #4385612) and 1 µL of 1 µM primers listed in **Table 3.4**. The PCR program is given in **Table 3.5**. The amplified product was normalised to the endogenous expression of 18S rRNA and represented as mRNA fold change, calculated using $2^{-\Delta\Delta Ct}$ method.

**Table 3.4. Primer sequences used for RT-qPCRs.** Gene names in capitals indicate primers for human genes, all other primers are for the mouse genes.

| Target | Sequence |
|---|---|
| *Rn18s* | Forward 5' - CGGACATCTAAGGGCATCACA |
| | Reverse 5' - AACGAACGAGACTCTGGCATG |
| *Lgals3* | Forward 5' - AACACGAAGCAGGACAATAACTGG |
| | Reverse 5' - GCAGTAGGTGAGCATCGTTGAC |
| *Vegfa* | Forward 5' - GTCCGATTGAGACCCTGGTG |
| | Reverse 5' - GCTGGCTTTGGTGAGGTTTG |
| *Glut1* | Forward 5' - ATCCCATCCACCACACTCAC |
| | Reverse 5' - GAGAAGCCCATAAGCACAGC |
| *P2ry12* | Forward 5' - CAAGGGGTGGCATCTACCTG |
| | Reverse 5' - GCCTTGAGTGTTTCTGTAGGGT |
| *Tmem119* | Forward 5' - ACTACCCATCCTCGTTCCCTGA |
| | Reverse 5' - TAGCAGCCAGAATGTCAGCCTG |
| *Ddx1* | Forward 5' - GGTGTCGACTGGAAAGCTCA |
| | Reverse 5' - ATCTGGTTGTGCATCCGGTT |
| *Dhx15* | Forward 5' - AGCAGCAATTCGGACAGTGA |
| | Reverse 5' - CTGCTGGGGTGGAAGTGTAG |
| *Dhx9* | Forward 5' - ATACTTCCACGCCCTCATGC |
| | Reverse 5' - AAGCCAAAACCACATCACGC |
| *Thoc1* | Forward 5' - CATTCTATTCTGCTGGCAAAAATTAT |
| | Reverse 5' - AAAGAGTTGAATTCTTCCACAGAAAAC |
| *Srsf7* | Forward 5' - GATTGCAGGCAGAGGAGGTT |
| | Reverse 5' - GTTTCTCCTCCATACCGCCC |
| *Hnrnpk* | Forward 5' - GTGCTGCCCTCACTCTACTG |
| | Reverse 5' - AGGTTGTGCACGTCCTTTGA |
| *Hnrnpu* | Forward 5' - ACAACAGAGGTGGAATGCCC |
| | Reverse 5' - CCCTGCTGCCACTGATTGTA |
| *Alyref2* | Forward 5' - GTTTTCCTGGGTGCTGTTGTG |
| | Reverse 5' - GTCATGTGTTCTGTCCATAAAAGT |
| *Sfpq* | Forward 5' - TGTCGGTTGTTTGTGGGGAA |
| | Reverse 5' – GTGTGTGGCAAATCGAACCC |

| | |
|---|---|
| *Srsf1* | Forward 5’ - GTGGTTGTCTCTGGACTGCC |
| | Reverse 5’ - GTTGCTTCTGCTACGGCTTC |
| *DDX5* | Forward 5’ - GTGTCATCGGTGTCCTTCCT |
| | Reverse 5’ - TAGAAAAGCGTGCGACAAGT |
| *VEGF* | Forward 5’ - CTACCTCCACCATGCCAAGT |
| | Reverse 5’ - CTCGATTGGATGGCAGTAGC |

**Table 3.5. Thermocycler settings for RT-qPCR.**

| Step | Temp | Duration | Cycle |
|---|---|---|---|
| 1 | 95 °C | 20 s | |
| 2 | 95 °C | 1 s | 40 |
| 3 | 60 °C | 20 s | |

## 3.16. RNA sequencing (RNA-seq)

### 3.16.1. Cell fixation with glyoxal and FACS

Cells were washed directly in cell culture plates with PBS, covered with TrypLE and incubated for around 2-3 min at 37 °C. Next, cells suspension was transferred to 1.5 mL Eppendorf tubes and then centrifuged. After discarding the supernatant, pellets were resuspended and fixed on ice with 3% Glyoxal fixation solution (0.31 mL 40% glyoxal (Sigma, #50649), 0.79 mL 100% ethanol, 30 µL acetic acid and 2.8 mL water, pH 4-5) with 1:50 RNasin Plus RNase Inhibitor (RI, Promega, #N2615) for 15 min as described previously [129]. Then, samples were washed with PBS supplemented with 1:100 RI and centrifuged at 500 x g for 3 min at 4˚C. Finally, cells were stained and sorted (see section 3.11), with additional RNase inhibitor (RI) supplementation: 1:50 during blocking and staining steps, 1:1000 during washing, 1:100 during sorting. Sorted cells were then centrifuged at 500 x g for 5 min at 4 °C and RNA was isolated using RNeasy Mini Kit (Qiagen) as described in section 3.14.

### 3.16.2. RNA-seq library preparation

The quality of RNA samples was assessed with Agilent 2100 Bioanalyzer using RNA 6000 Pico Kit (Agilent Technologies, #NC1711873). mRNA libraries were prepared using KAPA Stranded mRNAseq Kit (Roche, #07962142001) according to the manufacturer’s protocol and were sequenced at 2x 151 bp paired-end on NovaSeq 6000 by the Laboratory of Sequencing (Nencki Institute).

### 3.16.3. RNA-seq data processing and analysis

Two independent biological replicates were analysed per each condition. The quality of raw fastq data was evaluated using FASTQC software (https://www.bioinformatics.babraham.ac.uk/projects/fastqc/). Low-quality reads and adapter sequences were removed using Trimmomatic (version 0.36) [112]. The RNA sequencing reads were then aligned to the mm10 reference genome using the STAR aligner (v2.6) [130]. For further analysis, only uniquely mapped and properly paired reads were retained using samtools view -f 2 -q 255. The quantification and gene-level summarisation of mapped reads were conducted with HTSeq-count (version 0.9.1), using the union overlap mode and reverse stranded mode (-m union -s reverse) [131]. Raw read counts were processes for further analysis using R (version 4.2.2). All sequencing track were visualised in Integrative Genome Viewer (IGV) using a normalised bigWig file created with DeepTools (version 3.5.4) 'bamCoverage' and normalised to genome coverage – RPKM (Reads Per Kilobase Million) [116,117]. The averaged signal across all regions for the two replicates in each condition was calculated using DeepTools 'bigwigCompare' to generate a combined BigWig file [117].

### 3.16.4. Differential gene expression analysis

Analysis was performed in R (version 4.2.2) using Bioconductor package DESeq2 with model that includes all groups [118]. Genes that had significant (Benjamini and Hochberg-corrected P-value <0.05 and |log2 fold change| >=1) changes in their expression levels were called as differentially expressed. Gene ontology (GO) enrichment analysis was done using enrichGO form clusterProfiler [123]. Revigo and Cytoscape (version 3.10.2, https://cytoscape.org/) were used to summarise and visualise the GO-enriched terms [124,125]. Motif enrichment analysis for selected genes was performed using HOMER findMotifs.pl (http://homer.ucsd.edu/homer/motif/) for known TF motifs with the default parameters [126].

## 3.17. Cleavage Under Targets and Release Using Nuclease (CUT&RUN)

### 3.17.1. Samples processing

CUT&RUN was performed on BV2 cells exposed to hypoxic (<0.1% $O_2$) or normoxic condition for 16 hours, as described in direct co-culture section (section 3.3), using EpiCypher CUTANA ChIC/CUT&RUN Kit (Version 4, EpiCypher, 14-1048),

with slight modification to the manufacturer's protocol. Briefly, cells were mildly crosslinked with 1% formaldehyde for 3 min, followed by FACS (see section 3.11). Subsequently, 5 x $10^5$ cells per reaction were washed with PBS and stored at -80°C. Nuclei were isolated using nuclear extraction buffer containing 20 mM HEPES pH 7.9, 10 mM KCl, 0.1% Triton X-100, 20% glycerol, 1 mM MnCl2, 1 x cOmplete Mini protease inhibitor tablet and 0.5 mM spermidine. Activated concanavalin A (ConA) beads were added directly to the to the nuclear suspensions, followed by overnight incubation at 4°C with H3K27ac (Cell Signaling, #8173S). Chromatin digestion was carried out using protein pAG-MNase, and DNA fragments were released and recovered, followed by reverse crosslinking overnight at 55°C in the presence 0.094% SDS and 0.24 mg/mL proteinase K (Thermo Fisher Scientific, #EO0492). Sequencing libraries were generated using the QIAseq® Ultralow Input Library Kit (Qiagen, #180492), according to the manufacturer's instructions. Libraries were size-selected with AMPure XP beads (Beckman Coulter, #A63881) using a 1X bead to sample ratio, and quality assessed using an Agilent Bioanalyzer with the High Sensitivity DNA kit (Agilent Technologies, #5067-4626). Paired-end sequencing (2 × 150 bp) was performed on an Illumina NovaSeq 6000 platform at the Laboratory of Sequencing (Nencki Institute). Two independent biological replicates were analysed per each condition.

### 3.17.2. CUT&RUN data processing and analysis

Quality control of raw sequencing data was performed using FASTQC software (https://www.bioinformatics.babraham.ac.uk/projects/fastqc/). Adapter sequences and low-quality bases at the 5′ and 3′ ends were removed using Trimmomatic [112]. The resulting paired-end reads were aligned to mouse reference genome (mm10) using Bowtie2 with parameters --very-sensitive --no-mixed --no-discordant -I 10 -X 800 [113]. PCR duplicates were identified and removed using Picard's MarkDuplicates tool, and only uniquely mapped reads were kept for downstream analysis. Coverage signal files (bigWig format) were generated from BAM files using bamCoverage with CPM normalisation, allowing direct comparisons of signal between samples. Signal heatmaps were generated for individual conditions using CPM-normalised bigWig files and computeMatrix (reference-point mode). For direct comparison between conditions, $\log_2$ ratio tracks were generated with bigwigCompare and further processed with computeMatrix. Resulting signal matrices were exported and visualised in R

(version 4.2.2), using custom scripts to generate average signal plots. All signal-processing steps were performed using tools from the deepTools v2 package [117].

### 3.18. IvyGAP human glioblastoma data

Expression of selected genes was tested in the transcriptional atlas of human glioblastoma (Ivy Glioblastoma Atlas Project; http://glioblastoma.alleninstitute.org/), where samples for the RNAseq analysis had been collected via microdissection from distinct anatomic structures within GBM biopsies, including: perinecrotic regions considered as hypoxic, vascularised areas, tumour leading edge, infiltrative tumour or cellular tumour [132]. The z-score values were downloaded for the above genes. The violin plots or heatmaps showing the expression z-scores were generated in R (version 4.2.2).

### 3.19. Analysis of human and mouse scRNA-seq data

The analysis of scRNA-seq data was carried out by Patrycja Rosa, M.Sc., from the Laboratory of Molecular Neurobiology as a collaboration, and is included here as a supportive data. UMAP plots were created using single-cell RNA sequencing data from mouse tumour-associated macrophages and two human tumour-associated macrophage datasets from Antunes et al., (all available at GSE163120) [102]. The data were analysed in R (version 4.2.2) using Seurat (version 5.0.1) [133]. UMAP dimensions and cell labelling were applied as described in the original publication [102]. Visualizations were generated using functions from Seurat, ggplot2, Nebulosa, scCustomize and RColorBrewer. The "hypoxia score" module was computed using the Addmodulescore() function from the Seurat library. Correlations between selected marker genes and "hypoxia score" were calculated using the Spearman correlation coefficient with the cor() function. Heatmaps were generated using pheatmap package.

### 3.20. Statistical analysis

Statistical significance for western blotting quantification, qPCR, ChIP-qPCR, and immunofluorescent intensity data were assessed using Student's t-test and/or ANOVA as indicated in figure legends. Analyses were performed using GraphPad Prism. Data are presented as mean ± standard deviation (SD) or standard error of the mean (SEM) from at least three independent biological replicates, as indicated in the figure legends. A P-value of less than 0.05 was considered statistically significant.

The P-value ranges were shown in figures as follows: non-significant (ns), $P < 0.05$ (*), $P < 0.01$ (**), $P < 0.001$ (***), and $P < 0.0001$ (****) or as exact values.

### 3.21. Data availability

All sequencing data generated in this PhD project are available at the NCBI platform (https://www.ncbi.nlm.nih.gov/geo) under accession numbers: GSE200757 (ATAC-seq data files for GL261 cells), GSE279538 (ATAC-seq data files for BV2), GSE279536 (RNA-seq data files) and GSE300328 (CUT&RUN data files).

### 3.22. Illustrations graphical schemes

Graphical schemes in the figures were generated with BioRender.com.

# 4. Results

## 4.1. Oxygen-dependent changes of chromatin landscape in GL261 cells

Hypoxia induces extensive epigenetic alterations, for example through its effect on oxygen-dependent histone and DNA demethylases [72]. To investigate the impact of hypoxic stress on chromatin alterations, the murine glioblastoma model GL261 was used. The presence of hypoxic regions was confirmed in the orthotopic GL261 xenografts by injecting a pimonidazole probe, a hypoxia-specific marker that accumulates in cells under low oxygen tension (**Figure 4.1A**). Histone methylation changes were also verified in GL261 cells exposed to either moderate (1% $O_2$) or more severe (<0.1% $O_2$) hypoxia. As expected, an increase in H3K9me3 and H3K27me3 marks, associated with a repressive heterochromatin state, was observed. Importantly, hypoxia also induced an activating histone mark H3K4me3. Overall, histone methylation was increasing as the oxygen tension was decreasing and was the most pronounced at < 0.1% $O_2$ (**Figure 4.1B**). Next, the dynamics of histone methylation were evaluated in hypoxia followed by reoxygenation to 21% $O_2$. Notably, in all cases, histone methylation returned to the levels observed under normoxic conditions within 1-24 h after reoxygenation (**Figure 4.1C**). In addition, histone acetylation was assessed by examining H3K27ac, a marker which labels active promoters and enhancers. The data showed that hypoxia led to a loss of this mark, which began to re-appear 24 hours after reoxygenation (**Figure 4.1C**).

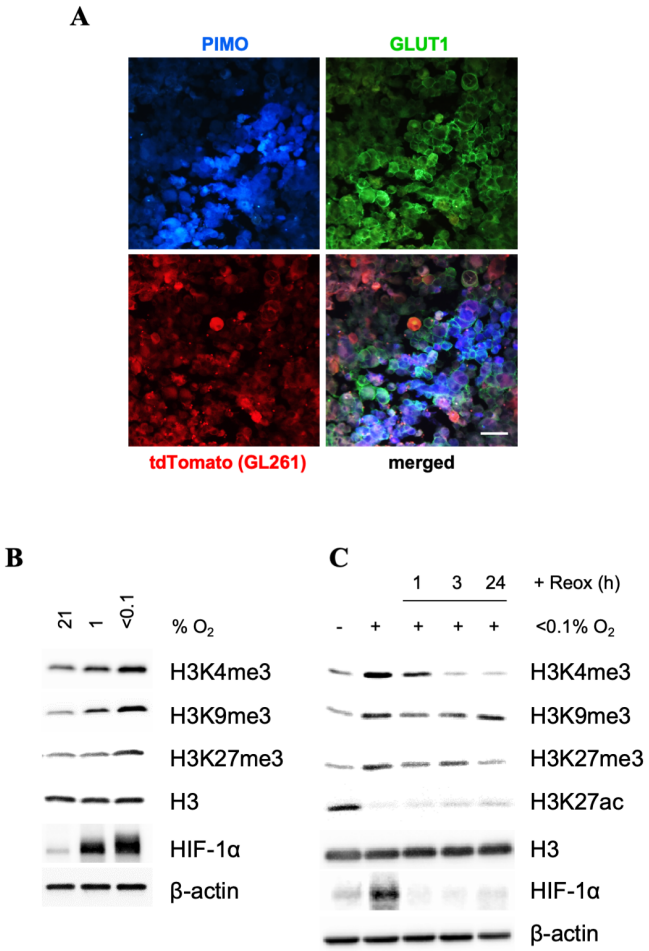


**Figure 4.1. Oxygen sensitivity in histone marks in GL261 cells. (A)** Immunofluorescent staining of GL261 glioma xenograft tissue demonstrating hypoxic zones, marked by the combined detection of pimonidazole (PIMO, Pacific Blue, shown in blue) and GLUT1 (Alexa Fluor 488, shown in green). GL261 glioma cells expressed tdTomato (shown in red). Scale bar = 20 µm. **(B-C)** Immunoblot analysis of the histone modifications in GL261 cells after exposed to **(B)** 21%, 1% or < 0.1% $O_2$ for 16 hours and **(C)** to hypoxia (<0.1% $O_2$) for 24 hours followed by 1, 3, 24 hours of reoxygenation (21% $O_2$). A representative western blot of three biological replicates is shown. HIF-1α served as hypoxia marker, β-actin and total histone H3 was used as endogenous control.

These data emphasised the oxygen-dependent changes in chromatin in glioma cells. However, since hypoxia-depended increases in methylation marks can have either repressive or activating influence on the regulation of gene expression (e.g. H3K27me3 vs H3K4me3), it remains unclear, how these alterations might impact the global chromatin properties, e.g. chromatin availability for the transcription machinery. In order to determine the chromatin accessibility in response to hypoxia in glioma cells, ATAC-seq analysis was carried out on GL261 cells exposed to hypoxic (1 and < 0.1% $O_2$) or normoxic (21% $O_2$) conditions. To prevent chromatin alterations caused by sample reoxygenation during processing (as demonstrated in **Figure 4.1C**), a modified

ATAC-seq protocol was implemented utilizing fixed cells, to preserve native chromatin accessibility profiles [110]. Data quality was assessed by performing principal component analysis (PCA), which demonstrated clear separation between normoxic and hypoxic conditions, as well as high reproducibility among biological replicates (**Figure 4.2A**). A total of 41733 ATAC-seq peaks (representing open chromatin regions) were identified across all conditions. Of these 67.3% were shared in all conditions, while 2.25% were unique to normoxia, 8.23% to 1% $O_2$, and 6.6% to < 0.1% $O_2$ conditions (**Figure 4.2B**). Next, differential analysis of open chromatin regions was preformed to assess the site-specific changes in response to hypoxia in GL261 cells. Under mild hypoxia (1% $O_2$), 5920 peaks with altered chromatin accessibility were identified compared to the normoxic control, and among these, 3091 peaks showed significantly increased accessibility, while 2829 peaks were significantly decreased (**Figure 4.2C**). In severe hypoxia (<0.1% $O_2$), 9792 peaks with differential chromatin accessibility were detected relative to normoxia. Of these, 4948 peaks showed significantly increased accessibility, and 4844 peaks were significantly decreased at <0.1% $O_2$ (**Figure 4.2D**). The presented data showed that severe hypoxia (<0.1% $O_2$) resulted in the highest number of significant ATAC-seq peak changes, supporting hypothesis that oxygen-dependent changes in histone methylation may be reflected by the changes in chromatin accessibility.

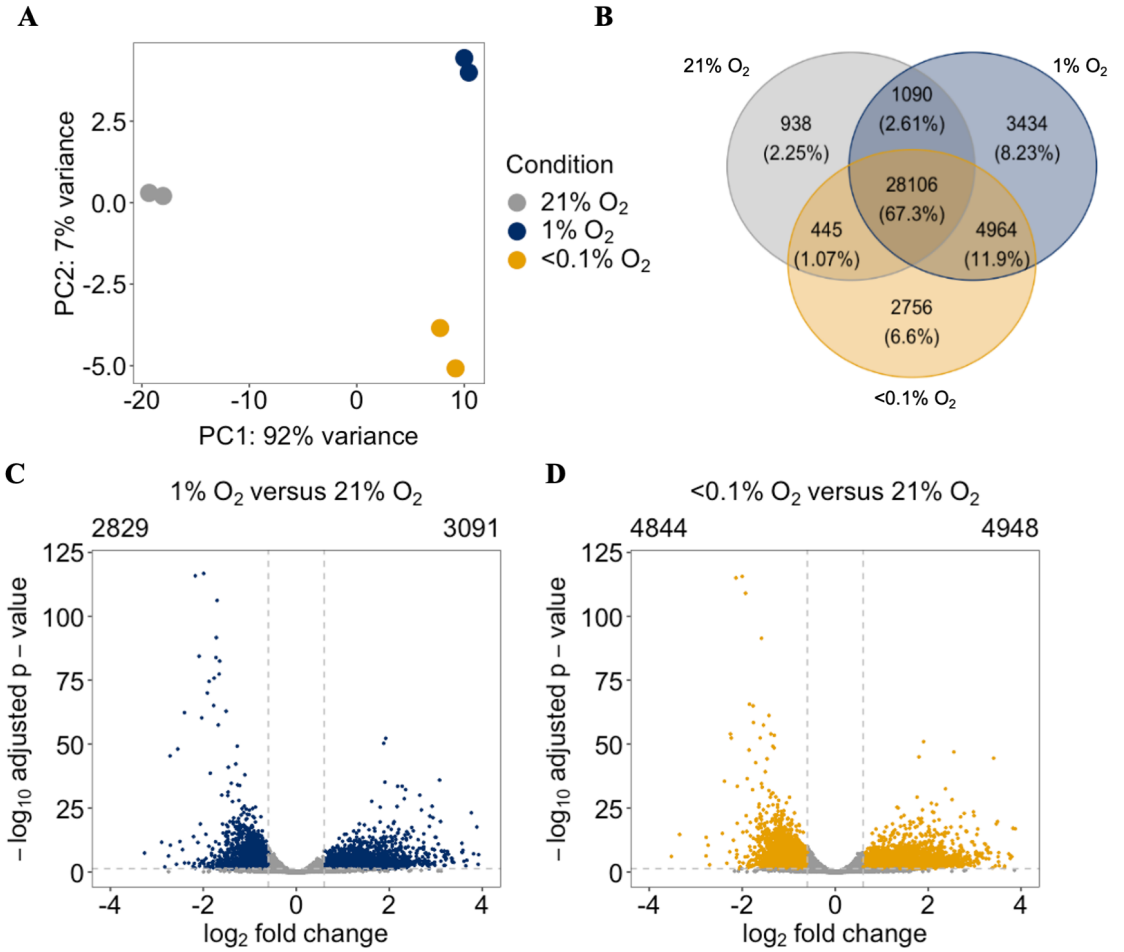


**Figure 4.2. Overview of the ATAC-seq results in GL261 cells. (A)** Principal component analysis of ATAC-seq signal for the three oxygen tensions. **(B)** Venn diagram showing overlap of unique or common peaks (open regions) detected for all oxygen conditions. The percentage of peaks in the total number of peaks is shown for each condition. **(C-D)** A volcano plot showing differentially altered ATAC-seq peaks in GL261 cells exposed to **(C)** 1% $O_2$ versus 21% $O_2$ **(D)** <0.1% $O_2$ versus 21% $O_2$. Each point on the plot corresponds to one peak. The X-axis shows the log2-fold differences between the groups and the Y-axis presents the corresponding adjusted p-values, -log10 (adj. p-value). Statistically significant peaks with FDR < 0.05 and |log2 fold change| ≥ 0.6 are marked in navy for 1% $O_2$ or in yellow for <0.1% $O_2$. The numbers of peaks significantly decreased- or increased are written above each plot.

Next, to link chromatin accessibility with gene regulation, genomic annotations to differentially altered regions in hypoxia were assigned. The data demonstrated that the greatest number of regions located within promoters was among peaks with reduced chromatin accessibility under both hypoxic conditions compared to normoxia (**Figure 4.3A**). Furthermore, a comparison between severe (< 0.1% $O_2$) and moderate (1% $O_2$) hypoxia demonstrated a marked increase in the number of promoters with decreased chromatin accessibility peaks under severe hypoxia - over 3000 peaks reduced in <0.1% $O_2$ and around 1000 peaks reduced 1% $O_2$ (**Figure 4.3A**). At the same time, the

number of accessible chromatin peaks increased with the drop of oxygen at introns and distal intergenic regions (**Figure 4.3A**). The oxygen dependency effect on chromatin accessibility was further supported by evaluating the ratio of the percentage of increased and decreased peaks at specific genomic annotations in severe versus moderate hypoxia (**Figure 4.3B-C**). Collectively, these results suggest that severe hypoxia preferentially decreases chromatin accessibility at gene promoters and increases chromatin accessibility at introns and intergenic regions, potentially contributing to broader transcriptional regulation under extreme oxygen deprivation.

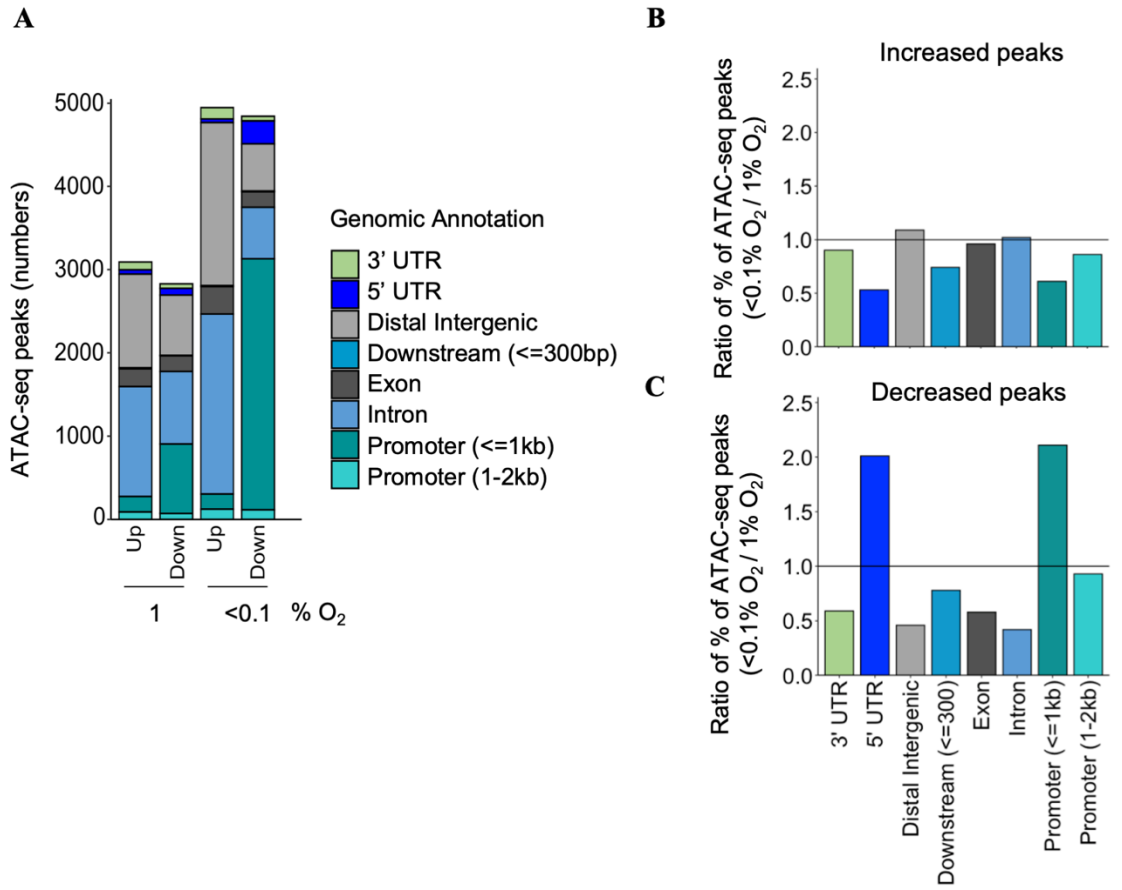


**Figure 4.3. Genomic location of ATAC-seq peaks. (A)** A stacked bar chart showing number of differentially regulated ATAC-seq peaks annotated to different genomic regions. 'Up' or 'Down' marks significantly increased or decreased peaks, respectively, at 1% or <0.1% $O_2$ in relation to normoxic control. **(B-C)** The ratio of the percentage of significantly increased **(B)** and decreased **(C)** ATAC-seq peaks under <0.1% $O_2$ hypoxia compared to 1% $O_2$ across distinct genomic regions.

Since severe hypoxia resulted in the greatest loss of accessible promoter regions, a functional enrichment analysis was performed on the genes assigned to peaks with significantly reduced chromatin accessibility at their promoters. This analysis, based on Gene Ontology (GO) biological processes terms, revealed downregulation of functions associated with RNA processing and metabolism, including ribonucleotide complex biogenesis, ncRNA metabolic process, or mRNA or ncRNA processing and splicing (**Figure 4.4A**). To validate the ATAC-seq findings, the expression of selected splicing-related genes with reduced chromatin accessibility at promoter regions was assessed by qPCR in GL261 cells (**Figure 4.4B**). These genes are components of the RNA splicing pathway (GO:0008380) and were previously shown to be dysregulated under hypoxic conditions [134]. It was found that some of these genes were clearly repressed at the mRNA level in hypoxia, e.g. *Sfpq, Alyref2, Thoc1, HnrnpU, HrnpK, Ddx1* etc., as compared to *Slc2a1 (Glut1)* or *Vegfa,* which are known HIF-1α target genes induced under hypoxic conditions (**Figure 4.4C**). Overall, these data demonstrate that hypoxia induces global changes in chromatin remodelling in GL261, leading to repression of multiple pathways. The correlation between reduced promoter accessibility and decreased mRNA expression further supports the functional impact of hypoxia-induced chromatin changes.

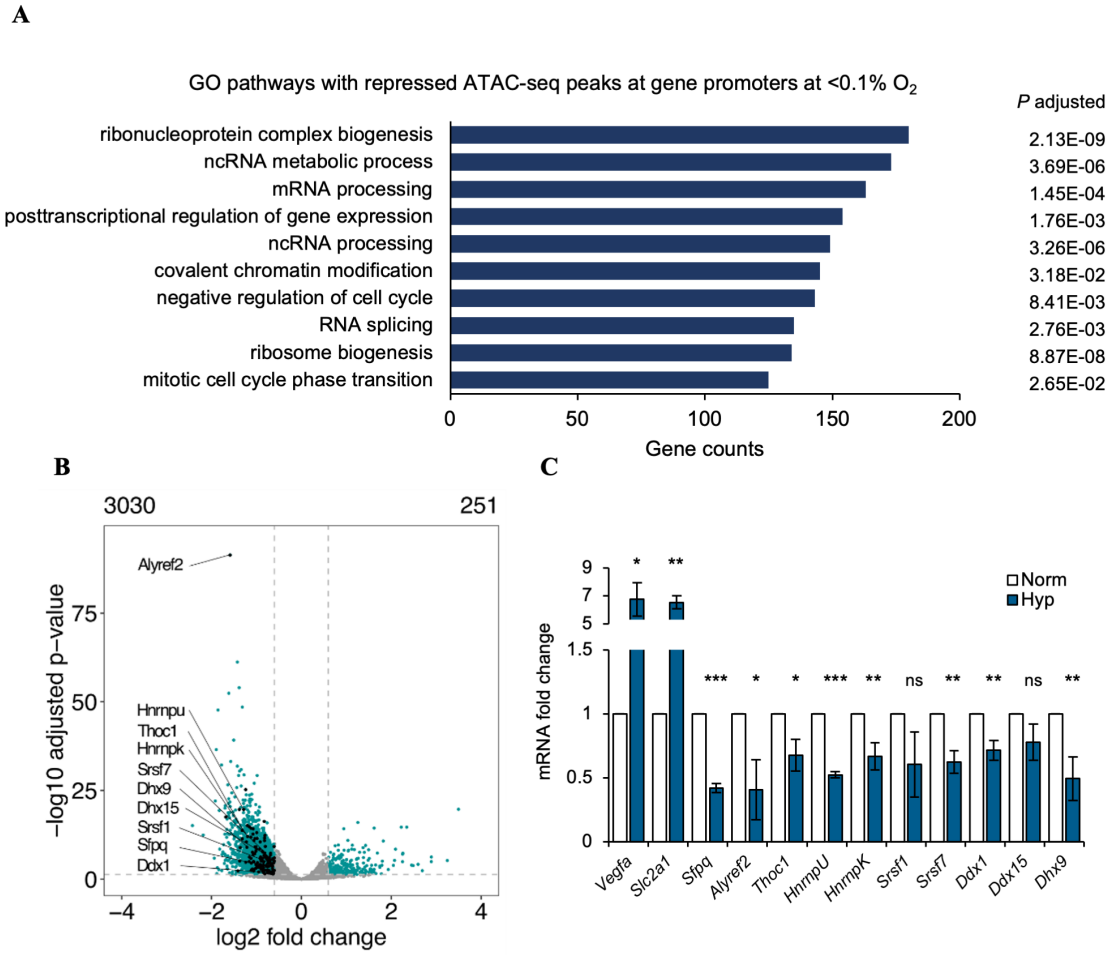


**Figure 4.4 Functional analysis of chromatin changes in BV2 cells under hypoxic conditions. (A)** Over-representation analysis of genes with decreased ATAC-seq peaks at their promoters. Top 10 gene sets, ranked by the highest gene count, are shown. The adjusted P-value indicates statistical significance of each pathway. **(B)** Volcano plots for ATAC-seq peaks located at the gene promoters in GL261 cells exposed to < 0.1% $O_2$ versus 21% $O_2$. Each point represents an individual promoter-associated peak. Black dots mark all significantly downregulated peaks for gene promoters from the GO pathway 'RNA splicing' (GO:0008380). The total number of significantly decreased and increased peaks is indicated above each plot. **(C)** Validation of hypoxia-dependent suppression of splicing-related genes using qPCR in GL261 cell line under 16 hours at < 0.1% $O_2$ treatment. *Vegfa* and *Slc2a1 (Glut1)* were used as hypoxia controls. Data are presented as mean ± SD from three biological repeats. Statistical significance was calculated with two-tailed Student's test.

A closer examination of the RNA-processing factor genes with decreased accessibility at their promoters revealed that many of them are known R-loop–associated factors (including *Ddx1/5/39b, Dhx9/15, Srsf1*). To determine whether ATAC-seq changes observed under hypoxic stress in glioma cells correspond to changes in the expression of identified R-loop interactome genes, the transcriptional data from the Ivy Glioblastoma Atlas Project (IvyGAP, http://glioblastoma.alleninstitute.org/) were analysed [132]. In IvyGAP, the gene expression was studied in samples collected by microdissection from different spatial locations in human GBM, including

"Microvascular Proliferation" regions and "Pseudopalisading Cells Around Necrosis", which should clearly distinguish between oxygenated and hypoxic regions, respectively. The Ivy GAP datasets showed that known hypoxia-inducible genes (*VEGFA*, *SLC2A1*, *CA9*, *BNIP3*, *BNIP3L*, and *LDHA*) had a high gene expression in "Pseudopalisading Cells Around Necrosis", as it was expected. On the other hand, many genes associated with R-loop regulation, exhibited decreased mRNA expression in human glioblastoma samples from "Pseudopalisading Cells Around Necrosis", highlighting the clinical significance of the ATAC-seq results (**Figure 4.5**). Among the hypoxia-repressed targets identified in our ATAC-seq analysis and validated using the IvyGAP dataset, was DDX5, as this RNA helicase has recently been recognised as a key factor in resolving R-loops [135].

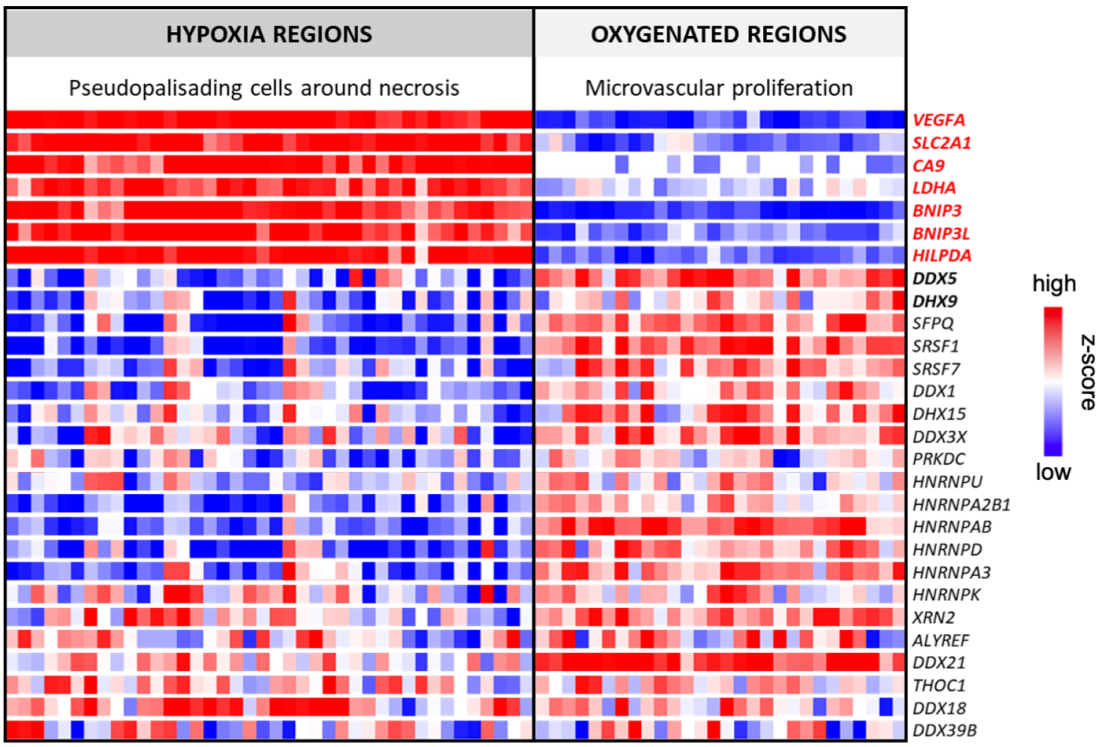


**Figure 4.5. Transcriptomic profiling of R-loop interactome genes under hypoxia.** RNA-seq from Ivy Glioblastoma Atlas Project (Ivy GAP). A heatmap showing a z-score expression of hypoxia markers and RNA processing factors from two anatomic features including 'microvascular proliferation' region and 'pseudopalisading cells around necrosis'. Each column represents a sample in a particular region, and the rows show the expression of selected genes in those samples.

To further confirm the link between chromatin accessibility and *DDX5* expression under hypoxia, ChIP-qPCR for H3K27ac was performed (**Figure 4.6A-C**). The results showed that H3K27ac, which is a histone modification marker of active promoter and enhancer regions, was significantly enriched at the promoter of DDX5 locus in normoxic conditions compared to hypoxia (**Figure 4.6A**). In contrast, no significant changes in H3K27ac enrichment were observed within the DDX5 gene body under (**Figure 4.6B**). Altogether ATAC-seq, ChIP-seq, RNAseq expression in IvyGAP human dataset and qPCR data (the latter tested in multiple cell lines in hypoxia, performed by co-authors of the publication [136]), suggest that hypoxia decreases DDX5 expression potentially through a decrease in H3K27ac, and ultimately, a decrease in chromatin accessibility at the promoter region. Finally, it was assessed whether the changes in DDX5 chromatin accessibility and gene expression under hypoxic conditions were reflected at the protein level. Western blot analysis demonstrated that DDX5 protein levels were reduced in response to hypoxia and returned to baseline levels upon re-exposure to oxygen (**Figure 4.6D**). Additionally, immunofluorescence staining of GL261 glioma xenograft from mice injected with pimonidazole, confirmed a reduced DDX5 protein expression in hypoxic tumour regions (**Figure 4.6E-F**).

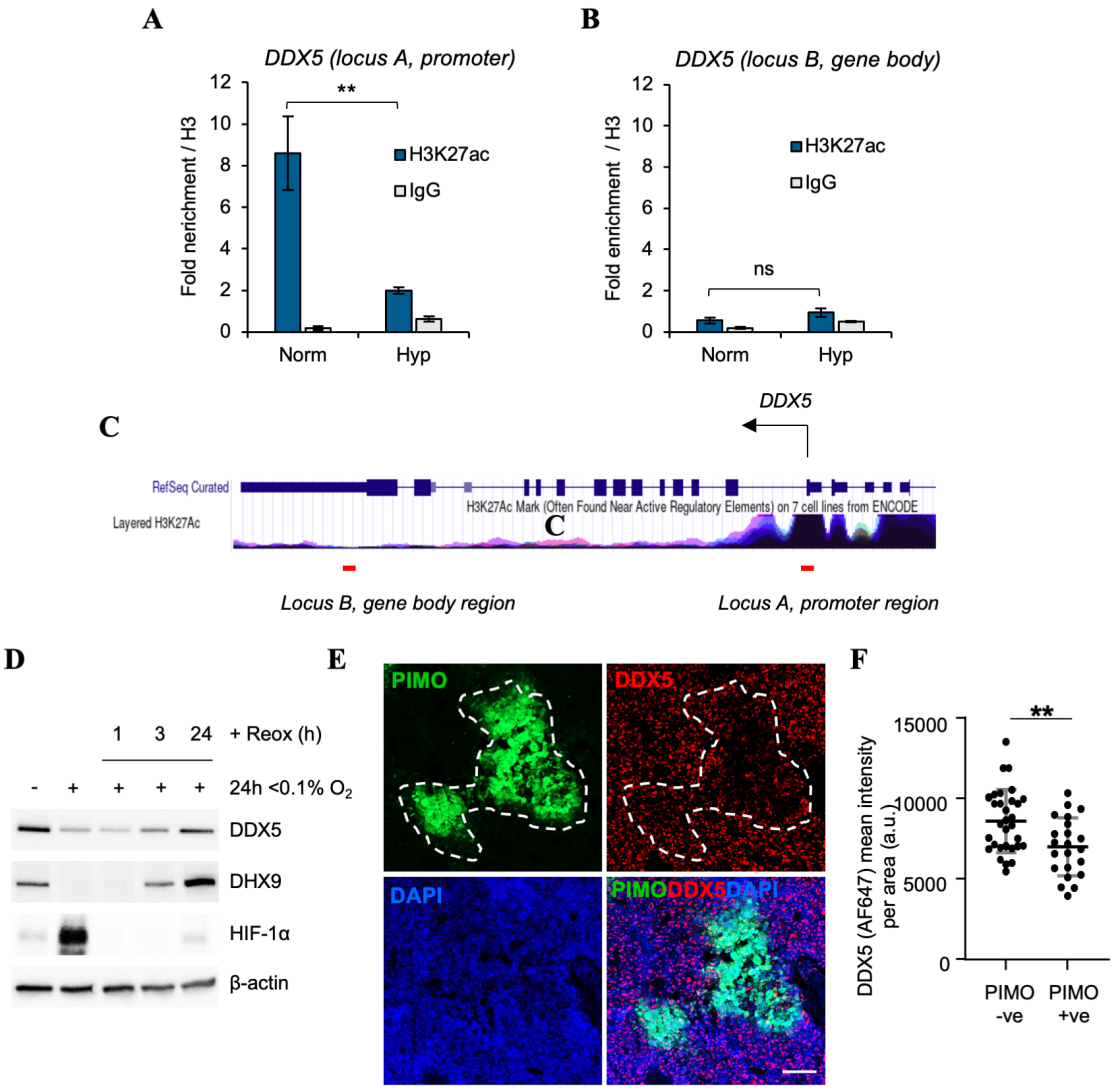


**Figure 4.6. Validation of DDX5 regulation under hypoxic conditions. (A-C)** ChIP-qPCR for H3K27ac in DDX5 locus in HCT116 cells exposed to hypoxia (< 0.1% $O_2$) or normoxia for 16 h followed by chromatin immunoprecipitation with H3K27ac, H3 and control IgG antibodies. All fold enrichment values were normalised to H3 levels and are presented as mean ± SD from three independent experiments for **(A)** promoter and **(B)** gene body regions of DDX5. Statistical significance was determined using two-tailed Student's t-test. **(C)** The UCSC Genome Browser view of the DDX5 locus aligned to the human GRCh37/hg19 genome, displays the H3K27ac profile that aided ChIP-qPCR primer design. Red lines indicate the biding sites for primers used in ChIP-qPCR, targeting either the promoter or the gene body region. **(D)** Western blot analysis of DDX5 and DHX9 protein in GL261 after exposed to hypoxia (0.1% $O_2$) for 24 hours followed by 1, 3, 24 hours of reoxygenation (to 21% $O_2$). HIF-1α served as hypoxia marker, β-actin was used as endogenous control. **(E)** Immunofluorescent staining for pimonidazole (PIMO, green) and DDX5 (red) in GL261 tumor-bearing mice. Nuclei were stained with DAPI (blue). Scale bar = 100 um. The outline of PIMO-positive staining (labelled with Alexa Fluor-488) is shown by the dashed white line. **(F)** Mean fluorescence intensity of DDX5 signal in GL261 tumors was measured in hypoxic (PIMO +ve) and normoxic (PIMO -ve) image areas using ZEN2 software (Zeiss). A total of 22 hypoxic areas and 31 normoxic areas were analysed. Statistical significance was calculated with two-tailed nonparametric Mann–Whitney test.

Together, these findings indicate that hypoxia leads to chromatin remodelling, including gene promoters, resulting in the repression of several functional pathways in cancer cells, including RNA splicing, and the R-loop interactome. The results presented in the section 4.1 were included in the manuscript, which tested the mechanisms of gene repression in hypoxic conditions and focused on the function of DDX5. As shown by co-authors, the loss of DDX5 in hypoxic conditions prevents further accumulation of R-loop levels and replication stress [136].

## 4.2. Hypoxia dysregulates expression of microglia and macrophage markers in myeloid cells in vitro and in GAMs in vivo

The main aim of the project was to explore the effect of hypoxia on myeloid cells, which are key immune cells present within the glioma microenvironment [137]. To address this, the expression levels of monocytic/macrophage marker *Lgals3,* as well as typical microglial markers *P2ry12* and *Tmem119,* were assessed under hypoxic condition in various murine myeloid cells. These included BV2 cells (an immortalized microglial cell line), RAW 264.7 cells (a tumour-derived macrophage cell line) and BMDMs (primary bone marrow-derived macrophages). All of the tested cells had increased *Lgals3* expression under severe hypoxic conditions (<0.1% $O_2$), together with well-known hypoxia-inducible genes such as *Vegfa* and *Glut1* (**Figure 4.7A**). These transcriptional changes were also confirmed at the protein level (**Figure 4.7B-C**). In addition, the expression of *Lgals3* mRNA and protein was slightly increased by exposure to mild hypoxia (1% $O_2$) and treatment with cobalt chloride ($CoCl_2$) (**Figure 4.7D-F**), a hypoxia-mimetic agent that inactivates prolyl hydroxylase and consequently stabilises HIF-1α in normoxic conditions [138]. These observations demonstrate that *Lgals3* is highly responsive to oxygen deprivation, and to some extent, to HIF-1α stabilisation.

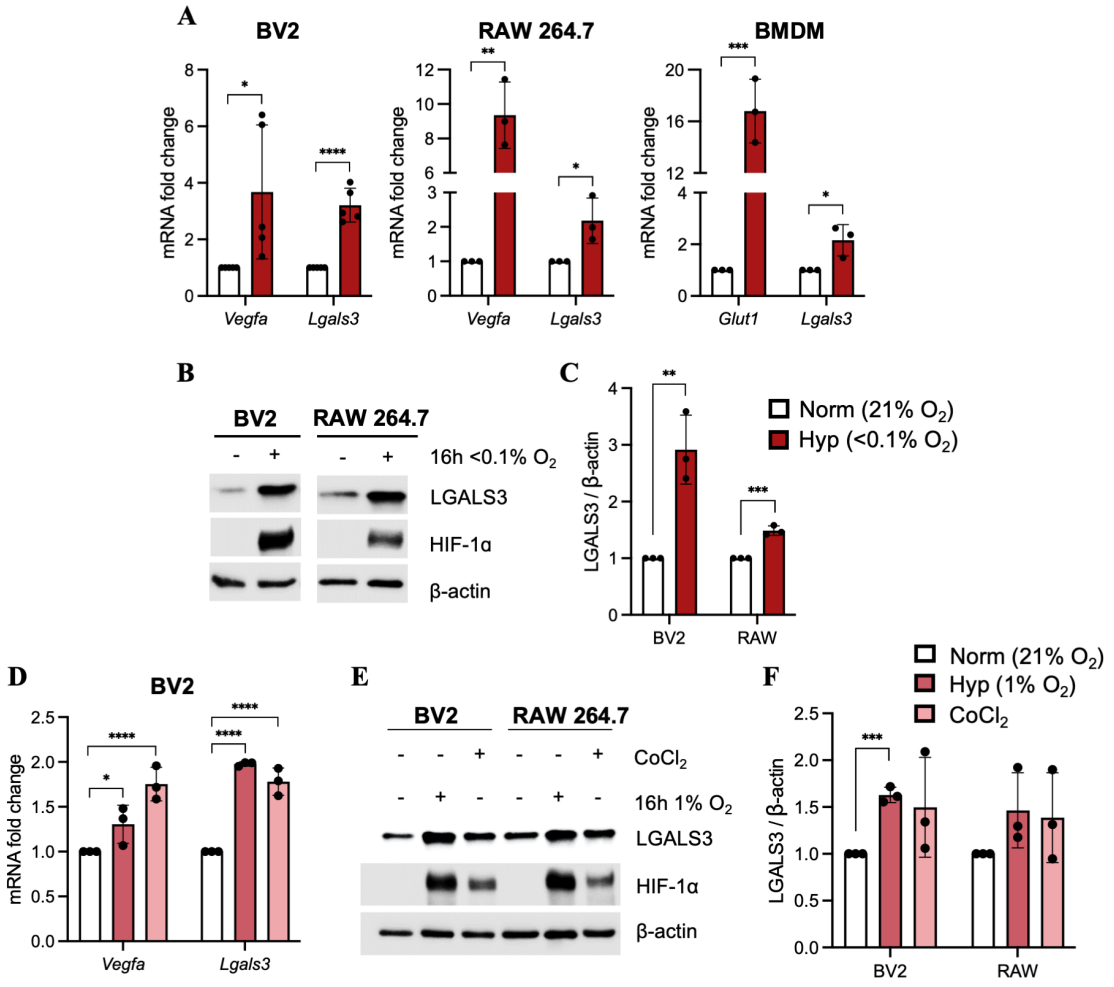


**Figure 4.7. Hypoxia increases the expression of *Lgals3* in myeloid cells**. **(A)** qPCR analysis of *Lgals3* in BV2, RAW 264.6 and BMBM cells exposed to <0.1% $O_2$ for 16h, in relation to *Rn18s* housekeeping gene. *Glut1* (*Slc2a1*) and *Vegfa* were used as hypoxia controls. **(B)** Western blot analysis of LGALS3 in BV2 and RAW 264.7 cell lines treated as in (A). HIF-1α was used as a hypoxia control **(C)** Densitometric analysis of LGALS3 relative to β-actin from (B). **(D)** qPCR analysis of *Lgals3* in BV2 cells exposed to 1% $O_2$ or $CoCl_2$ for 16 hours in relation to *Rn18s* housekeeping gene. Vegfa was used as hypoxia control. **(E)** Western blot analysis of LGALS3 in BV2 and RAW 264.7 cell lines treated as in (D). HIF-1α was used as a hypoxia control **(F)** Densitometric analysis of LGALS3 relative to β-actin from (E). All graphs show mean ± SD from at least three independent experiments. Student's t test was used to determine statistical significance.

Notably, the expression of the canonical microglial markers, *P2ry12* and *Tmem119*, was significantly reduced under the same hypoxia or hypoxia-mimicking conditions (**Figure 4.8A-B**). While these genes are considered microglia-specific markers, their baseline expression was also observed in RAW 264.7 and BMDM cells, and was further reduced by hypoxia.

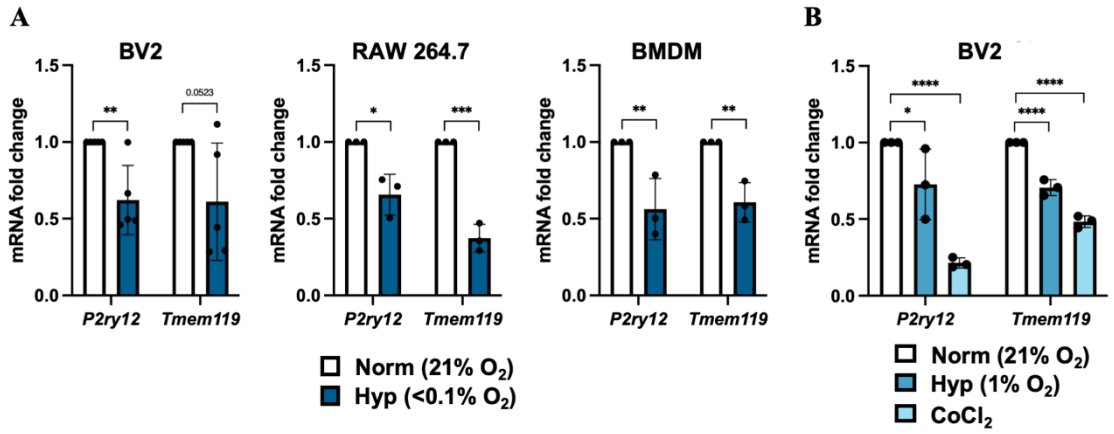


**Figure 4.8. Hypoxia decreases the expression of *P2ry12* and *Tmem119* in myeloid cells. (A-B)** qPCR analysis of *P2ry12* and *Tmem119* in **(A)** BV2, RAW 264.6 and BMDM cells exposed to <0.1% $O_2$ for 16h and in **(B)** BV2 exposed to 1% $O_2$ or $CoCl_2$ for 16 hours in relation to *Rn18s* housekeeping gene. The mean fold change ± SD is shown from at least three independent biological replicates. Two-tailed student t-test determined the statistical significance.

Altogether, these findings indicate that hypoxic stress differentially regulates the expression of selected microglial and macrophage markers, leading to the upregulation of *Lgals3* and downregulation of *P2ry12* and *Tmem119*. Such changes suggest that hypoxia can reshape the gene expression program, including the key genes defining the myeloid cell identity and function.

To further verify the expression of these genes *in vivo*, publicly available scRNA-seq datasets of murine and human GBM GAMs from Antunes *at al.* were analysed in collaboration with Patrycja Rosa, M.Sc. ( Laboratory of Molecular Neurobiology, Nencki Institute) (**Figure 4.9**) [102]. This study provided annotation of multiple GAM sub-clusters, including microglia, monocytes, lipid-associated, proliferative, interferon-responsive (IFN), and hypoxic clusters (**Figure 4.9A**, in the original Antunes publication, the term TAMs, tumor-associated myeloid cells, was used rather than GAMs; this terminology is used here for consistency with the published dataset) [102]. Based on the published cluster annotations (**Figure 4.9A**), *Lgals3* expression was found to be highly enriched in cells within the hypoxic cluster (green) (**Figure 4.9A-B**). Additionally, cells in this cluster were predominantly assigned within the Mo-TAM clusters rather than the Mg-TAM clusters (**Figure 4.9A**).

To more precisely identify genes that define hypoxic TAMs, the hypoxia-enriched cluster from another scRNA-seq GBM dataset published by Wang et al. was extracted [103]. These genes were then combined with those from the hypoxic cluster in Antunes dataset to create an extended "hypoxia score," resulting in a 42-gene set (**Table 4.1**).

**Table 4.1. List of genes included in the hypoxia score.** Genes were extracted from publicly available scRNA-seq datasets [102,103]. Notably, 17 of these genes (40 %, marked in bold) were shared between the two datasets, indicating substantial overlap between the independent hypoxic TAM signatures. The remaining genes highly expressed in hypoxic clusters in each study were incorporated to provide broader representation of hypoxia-associated genes.

| "Hypoxia score" genes |
|---|
| *Arg1,* ***Adam8****, Mif, Aldoa, Gapdh, Ldha, Tpi1, Srgn, Pgam1,* ***Bnip3****, Pkm, Vim, Lgals3, Gpi1, Ftl1, Cstb,* ***Adm****,* ***Bnip3l****, Eno2,* ***Fam162a****, Rala,* ***Cytip****, Cd109,* ***Eno1b****, Scd4,* ***Plp2****, Rab42,* ***S100a10****, S100a6,* ***Hk2****,* ***Slc2a1****,* ***Cxcl3****,* ***Lgals1****, Timp1, Plin2, Ctsl,* ***Ndrg1****,* ***Hilpda****,* ***Ero1a****, Nupr1,* ***Mt2*** |

Next, the average expression of these hypoxia-associated genes (hypoxia score) was calculated across all TAM subclusters in the scRNA-seq Antunes dataset. In addition to the originally annotated hypoxic Mo-TAMs cluster (**Figure 4.9A**), elevated hypoxia score was also observed in other TAM populations, particularly in the lipid, transitory and proliferative Mo-TAMs, as well as in a small subset of Mg-TAMs (**Figure 4.9A** and **Figure 4.9C**). The expression of *Lgasls3* was stronger in the entire Mo-TAMs compared to Mg-TAMs, as previously reported in other studies [101]. However, it was additionally upregulated in cells with the increased hypoxia score, such as proliferative, lipid, monocytic and transitory Mo-TAMs, as well as the hypoxic subset of Mg-TAMs (**Figure 4.9A-C**). In contrast, the expression of *P2ry12* and *Tmem119* was elevated in Mg-TAMs compared to Mo-TAMs, but showed a marked decrease in cells with high hypoxia score (**Figure 4.9D-F**). The correlation of expression between the genes defining the hypoxia score and *Lgals3* was significantly positive, while for *Tmem119* and *P2ry12* it was significantly negative, particularly in Mg-TAMs (**Figure 4.9F**). Importantly, these observations were consistent across both the murine and human TAM scRNA-seq datasets, including samples from newly diagnosed and recurrent GBM cases analysed in the Antunes study.

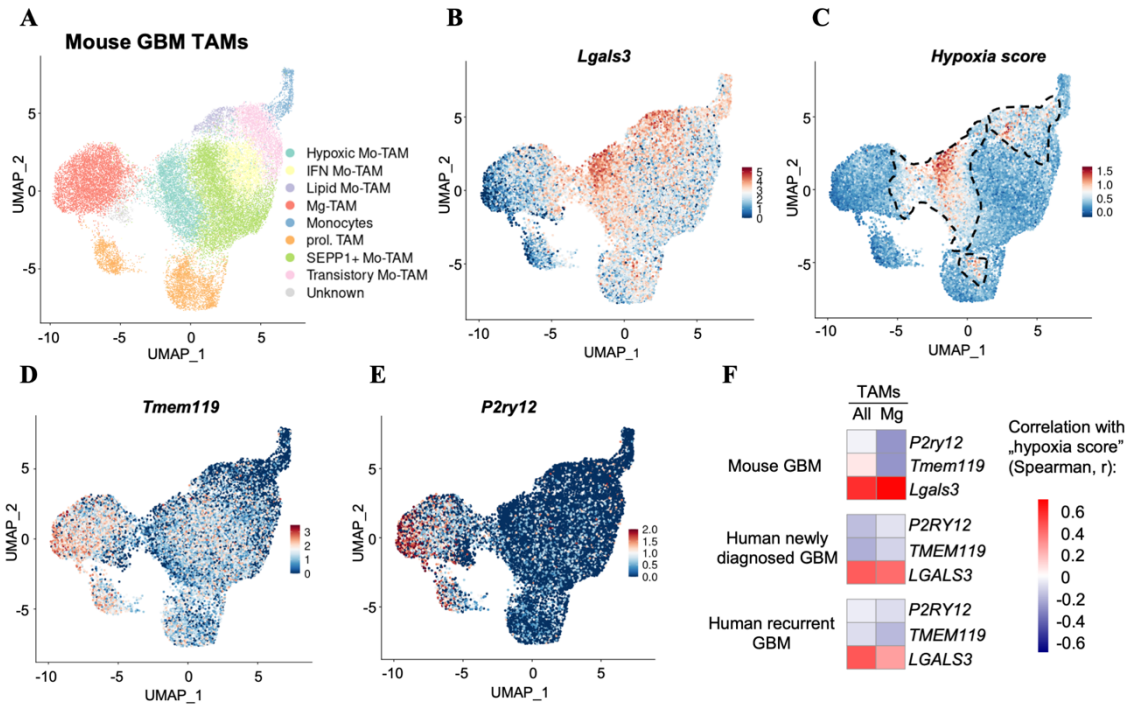


**Figure 4.9. Hypoxia dysregulates the expression of *Lgals3*, *P2ry12* and *Tmem119* in myeloid cells in GBM samples *in vivo*. (A)** UMAP plot demonstrating monocytes and TAM subpopulations clusters from mouse GL261 tumours as identified in the public scRNA-seq dataset (GSE163120). **(B)** UMAP plots showing the expression of *Lgals3* in the dataset from (A). **(C)** UMAP plot showing the average expression of genes defined as hypoxia score in the dataset from (A). **(D-E)** UMAP plots showing the expression of **(D)** *Tmem119* and **(E)** *P2ry12* in the dataset from (A). **(F)** Heatmaps showing the Spearman's correlation between gene expression of hypoxia score and *P2ry12*, *Tmem119* and *Lgals3* in mouse GL261 tumours, human newly diagnosed GBM and human recurrent GBM scRNA-seq Antunes-datasets (all data from GSE163120). The analysis was done in collaboration with Patrycja Rosa, M.Sc. from the Laboratory of Molecular Neurobiology, Nencki Institute.

To further validate aforementioned results, the transcriptional data from the IvyGAP glioblastoma project (http://glioblastoma.alleninstitute.org/) were also analysed. The expression of *LGALS3* was the strongest in the perinecrotic and pseudopalisading regions (CTpnz and CTpcan), mirroring the expression patterns of some typical hypoxic markers such as *SLC2A1 (GLUT1)* or *VEGFA* (**Figure 4.10**). In contrast, the expression of *TMEM119* and *P2RY12* was the lowest at the hypoxic perinecrotic and pseudopalisading areas and the most abundant in the infiltrating tumour (IT) and tumour leading edge (LE) (**Figure 4.10**). While this may indicate that the cells expressing *TMEM119* or *P2RY12* are less abundant in the perinecrotic regions, this data also suggests that hypoxia can strongly dysregulate the expression of the tested genes in tumours *in vivo*, irrespectively of the cell types exposed to hypoxic stress.

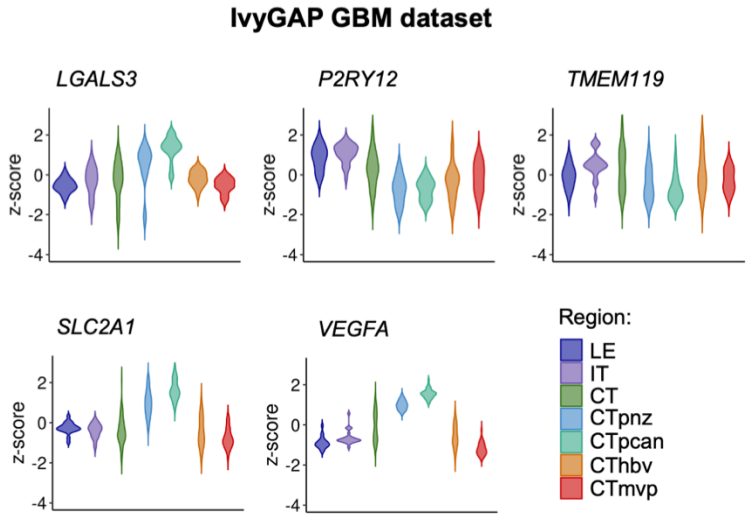


**Figure 4.10. RNAseq from Ivy Glioblastoma Atlas Project (Ivy GAP).** Violin plots showing z-score expression of *LGALS3, P2RY12* and *TMEM119* genes, as well as hypoxia-inducible genes *SLC2A1* and *VEGFA* in different anatomical features of GBM samples from Ivy GBM Atlas Project dataset (Ivy GAP; https://glioblastoma.alleninstitute.org/). LE, leading edge; IT, infiltrating tumour; CT, cellular tumour; CTpnz, perinecrotic zone; CTpcan, pseudopalisading cells around necrosis; CThbv, hyperplastic blood vessels in cellular tumour; CTmvp, microvascular proliferation.

## 4.3. Transcriptomic changes in BV2 microglial cells induced by hypoxia and glioma interaction

To better understand how hypoxic stress shapes the gene expression landscape in tumour-associated myeloid cells, direct microglia-glioma co-cultures have been employed. This model effectively recapitulates microglia-tumour interactions during glioma progression (see the co-culture summarised in a scheme in the Methods Section 3.3). To prevent reoxygenation and preserve hypoxia-induced gene expression levels, the co-coculture was fixed with glyoxal immediately after hypoxic exposure. For clarity, the tested conditions are referred to as: CC_N for BV2 cells isolated from normoxic co-cultures with glioma, CC_H for BV2 cells isolated from hypoxic co-cultures with glioma, Ctrl_N for BV2 monocultures in normoxia and Ctrl_H for BV2 monocultures in hypoxia. Before proceeding with transcriptomic analyses, a series of quality control steps were carried out to ensure the data reliability. Firstly, apoptosis levels in BV2 cells after 16 hours of hypoxia were assessed and estimated at approximately 6%, indicating that cell death was unlikely to significantly affect gene expression analyses (**Figure 4.11A** and **Figure 4.11B**; N.B. In the assays, cells were always used after the PBS wash, which removed the majority of potentially apoptotic cells). In addition, a high RNA integrity was confirmed in glyoxal-fixed samples, along with the induction of hypoxia-responsive

genes, as assessed by qPCR (**Figure 4.11C-D**). In addition, microglia co-cultured with glioma cells, underwent morphological changes characterised by more elongated shapes in hypoxic conditions, which was assessed using phalloidin staining of F-Actin (**Figure 4.11E**).

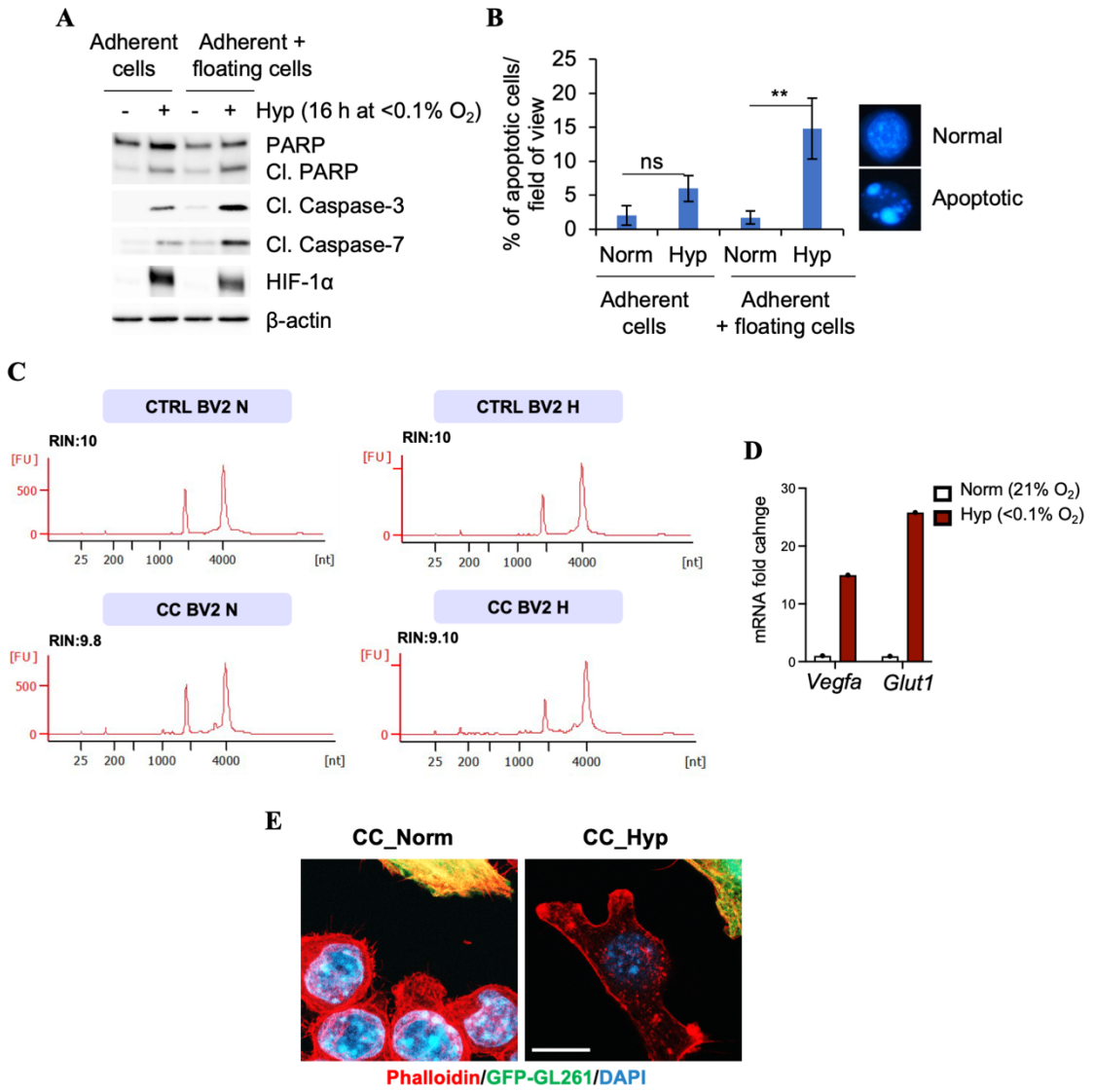


**Figure 4.11. Qualitative assessment of BV2 microglia cells exposed to hypoxia. (A)** BV2 cells were exposed to 21% or <0.1% $O_2$ for 16 hours and cellular lysates were subjected to western blotting to detect apoptosis markers, such as cleaved (cl.) PARP, cl. Caspase-3 and cl. Caspase-7, as well as HIF-1α (hypoxic marker) and β-actin (loading control). **(B)** BV2 cells were treated as in (A), and the percentage of apoptotic cells was quantified in adherent only or total (combined adherent and floating cells from the media) across 15 randomly selected fields of view. Data are presented as mean ± SEM. Statistical significance was determined using two-way ANOVA followed by Tukey's post hoc test. **(C)** Bioanalyzer profiles of total RNA derived from BV2 cells after glyoxal fixation. **(D)** Expression analysis (qPCR) of *Vegfa* and *Glut1* in BV2 cells after glyoxal fixation, as indicated in relation to *Rn18s* housekeeping gene. **(E)** Immunofluorescent images of BV2 and GL261 (stably expressing GFP) cells co-cultured in normoxic or hypoxic conditions as in (A). Red colour visualises actin cytoskeleton stained with phalloidin and blue colour marks nuclei stained with DAPI. Green to yellow cells represent GL261 while red-only positive cells (negative for GFP) are microglia cells. Scale bar, 10 μm.

To confirm that sorted BV2 microglia were not contaminated with glioma cells (potentially resulting from cell fusion or phagocytosis during co-culture), the expression of EGFP (expressed by GL261 glioma cells only) was assessed in BV2 samples. No significant alignment to the EGFP was detected in BV2 cells from co-cultures with glioma cells and BV2 monocultures, confirming the purity of the microglial population (**Figure 4.12A-B**). The PCA of gene expression revealed a clear separation across all four tested conditions. Hypoxic stress was the dominant factor driving transcriptional changes, as indicated by the separation of samples along PC1, while the co-culture effect contributed less to the variance, with samples separating along PC2 (**Figure 4.12C**). Next, the differential gene expression analysis was performed, focusing on three distinct comparisons: CC_H vs CC_N (assessing the impact of hypoxia on co-cultured microglia), Ctrl_H vs Ctrl_N (evaluating the effect of hypoxia on microglia in monoculture, i.e., hypoxia alone) and CC_N vs Ctrl_N (examining the effect of glioma presence on microglia). Minor changes in gene expression were detected in BV2 cells treated with glioma cells in normoxia (412 up and 44 down; CC_N versus Ctrl_N; **Figure 4.12D**). Exposure of BV2-GL261 co-cultures to hypoxia caused many more transcriptomic changes in BV2 cells, in comparison to the normoxic co-culture, with 2605 upregulated and 1942 downregulated genes (CC_H versus CC_N, **Figure 4.12E**). BV2 cells exposed to hypoxia alone also had a large number of transcriptomic changes (2267 up and 1786 down; Ctrl_H versus Ctrl_N, **Figure 4.12F**). The majority of the hypoxia-imposed gene expression changes were also altered by hypoxia in co-cultures, with common 1788 genes up- and 1382 down-regulated (**Figure 4.12G**).

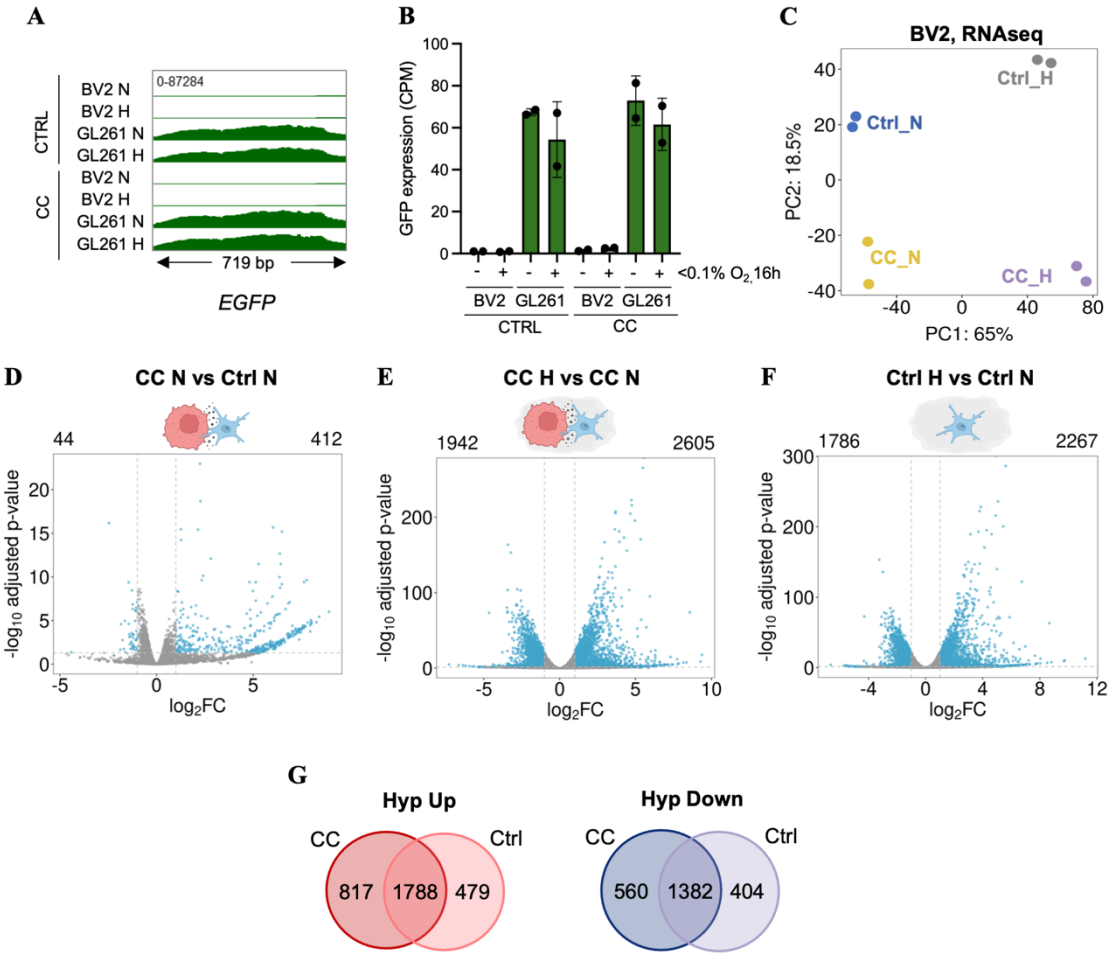


**Figure 4.12. Gene expression analysis in BV2 microglial cells exposed to glioma cells and hypoxia.** **(A)** Integrative Genomics Viewer (IGV) snapshot displaying RNA-seq read alignment to the GFP sequence in BV2 and GL261 cells. **(B)** GFP expression in hypoxia-treated BV2 and GL261 cells cultured either alone (Ctrl) or in co-culture with glioma cells (CC). Expression levels are shown as counts per million (CPM). **(C)** A principal component plot of normalised gene expression in BV2 cells in normoxia (Ctrl_N), hypoxia (Ctrl_H), normoxic co-cultures with glioma (CC_N) or in hypoxic co-cultures with glioma (CC_H). **(D-F)** Volcano plots showing expression changes in tested conditions, as indicated above each plot. Each point on a plot corresponds to one gene. Genes with significantly altered expression levels (adj. p-value<0.05 and |log fold change |≥1) were marked in blue. The numbers of genes significantly down- or upregulated are written above the plots. **(G)** Venn diagrams summarising the overlap between differentially downregulated (left) and upregulated (right) genes in BV2 cells after exposure to hypoxia in the presence (CC) or absence (Ctrl) of glioma cells.

To verify that cellular hypoxia pathways driven by HIF transcription factors were activated in BV2 cells under hypoxic conditions, the expression of genes from a validated 48-gene HIF signature ("HIF metagene" score) was assessed [139]. The HIF metagene expression was significantly increased in the transcriptome of BV2 under hypoxic conditions (**Figure 4.13A**). In addition, the analysis of TFs motifs enriched in the promoters of up-regulated genes identified those, that are known to be active in hypoxic conditions, including HIF-1α, HIF-2α, Krüppel-like factors (KLFs), ATF3 or ATF4

(**Figure 4.13B**). Next, the Gene Ontology (GO) analysis of biological processes of significantly differentially expressed genes in BV2 microglia co-cultured with glioma cells under hypoxia was carried out. As expected, among the upregulated genes, pathways associated with cellular response to oxygen levels, endoplasmic reticulum (ER) stress, and unfolded protein response were identified as significantly enriched. In addition, the enrichment of chemotaxis, cell motility and blood vessels morphogenesis processes were observed (**Figure 4.13C**). These transcriptional changes were consistent with the morphological changes detected in hypoxia-exposed BV2 cells within the glioma co-culture, including elongated lamellipodia- or filopodia-like structures (**Figure 4.11E**). On the contrary, the downregulated genes in hypoxic BV2 cells from glioma co-cultures were linked to biological pathways commonly suppressed under low oxygen conditions, including ribosome biogenesis, RNA processing, and DNA replication (**Figure 4.13D**) [33,134,136].

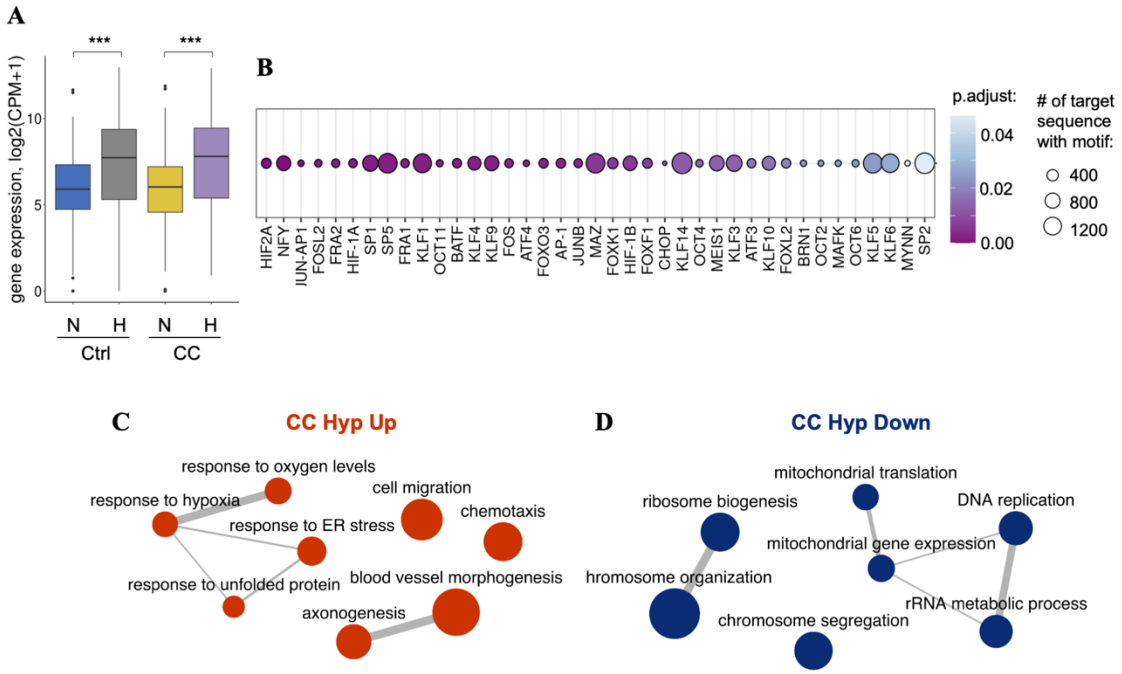


**Figure 4.13. Functional analysis of gene expression in BV2 microglia cells. (A)** HIF metagene expression analysis in the RNA-seq data from BV2 cells treated with hypoxia as monocultures (Ctrl) or co-cultures with glioma (CC). HIF metagene set was defined by Lombardi et al. [139]. The average gene expression signal of the HIF metagene signature is represented as read counts per million. Student's t test was used to determine statistical significance. **(B)** Transcription factor motif enrichment analysis using HOMER tool on the promoters of significantly upregulated genes in BV2 cells after hypoxic co-culture with glioma cells in relation to normoxic co-culture. **(C-D)** Dot plots of enriched GO pathways for gene sets significantly upregulated **(C)** or downregulated **(D)** after exposure to hypoxia in coculture with glioma cells (CC). The top 15 GO pathways were selected based on the lowest adjusted p-values, and closely related terms were merged using REVIGO.

Next, a closer examination of genes that were more upregulated after hypoxia in BV2 cells cultured with glioma cells, compared to BV2 monoculture was carried out (**Figure 4.14A-B**). Genes increased in hypoxic BV2 in co-culture as compared to monoculture were related to processes such as axon formation, axon development, and changes in cell morphology (e.g. *Lamc2, Ddr1, Map1b, Ngfr, Gdnf, Fgfr3, Lama5, Plxnb3, Myo5b, Map6*, **Figure 4.14B**, right panel). On the other hand, a group of genes more downregulated under combined hypoxia and co-culture (compared to monocultures) were involved in leukocyte and myeloid cell differentiation (e.g. *Mef2c, Tnfrsf11a, Rassf2, Lfng, Slc9b2, Nfam1, Ighm*, and *Dyrk3* (**Figure 4.14B**, left panel). These results suggest that hypoxia may suppress the expression of certain myeloid genes, and this effect is likely further shaped by the contacts with glioma cells.

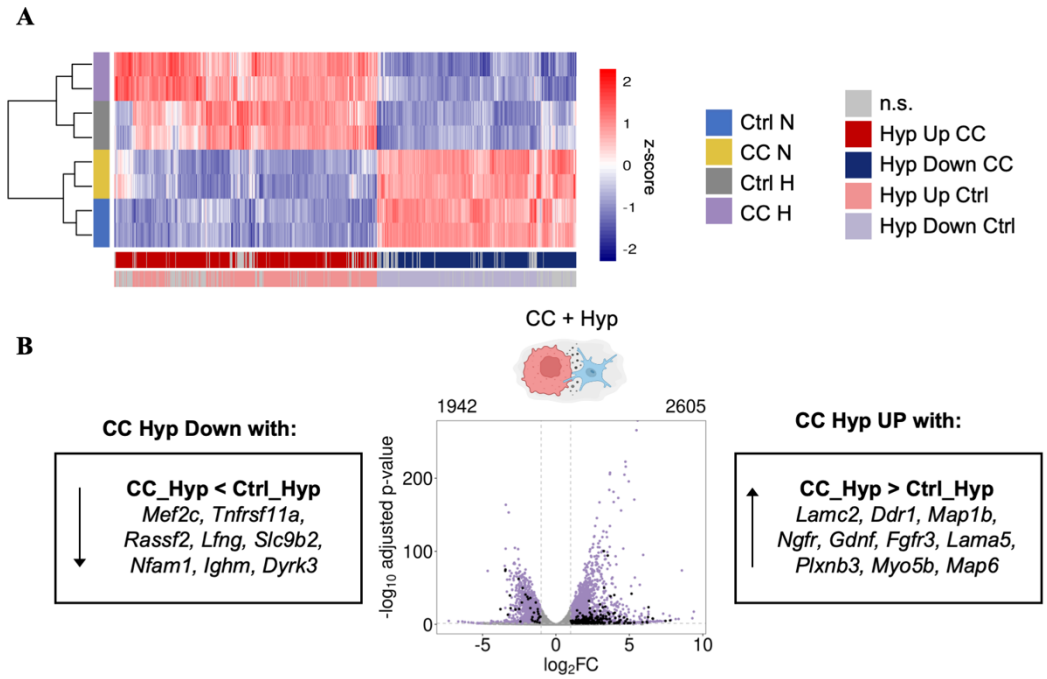


**Figure 4.14. Detailed analysis of genes further upregulated in BV2 by hypoxia in co-coculture then in monoculture. (A)** A heatmap showing z-score expression for genes up- or downregulated by hypoxia in CC (projected in red or blue, respectively) or Ctrl hypoxic cells (projected in light red and light blue, respectively). **(B)** A volcano plot with gene expression changes in glioma co-cultured (CC) BV2 cells in hypoxia compared to normoxia (with 1942 down and 2606 upregulated genes projected in purple). Genes with increased or decreased expression in CC versus Ctrl hypoxic conditions are projected in black. Left and right box panels show examples of genes additionally decreased or increased in CC versus Ctrl, respectively.

### 4.4. Changes in expression of multiple known monocyte/macrophage and microglial marker genes under hypoxia

Since the selected Mo/Mφ marker genes were found to be dysregulated under hypoxic stress (**Figure 4.7**, **Figure 4.8**, **Figure 4.9**), a broader transcriptomic analysis was performed in BV2 cells using RNA-seq data from the co-culture model. Firstly, a list of genes highly expressed in distinct GAM subsets was compiled based on previously published scRNA-seq datasets in which Mg-GAMs and Mo-GAMs, as well as functionally specialised Mo/Mφ-GAM subpopulations, including hypoxic, lipid-associated, phagocytic, chemotactic, interferon-responsive, ribosomal, and transitory clusters, had been identified [101–103]. Then, expression of those selected genes was analysed in BV2 cells in three distinct comparisons including CC_N vs Ctrl_N (CC), CC_H vs CC_N (CC + Hyp) and Ctrl_H vs Ctrl_N (Hyp) (**Figure 4.15**). As expected, the majority of genes associated with the hypoxic-GAMs and defined earlier as hypoxia score, were upregulated in BV2 cells after hypoxia treatment (**Figure 4.15A**). Among Mg-GAM marker genes were either up or downregulated by hypoxia, while the Mo/Mφ-GAM-associated genes were mainly upregulated by hypoxia (**Figure 4.15B**). Additionally, a number of genes defining functional subclusters were significantly altered by hypoxia in BV2 microglia cells (**Figure 4.15C**). Specifically, genes from lipid-associated GAM cluster were predominantly upregulated under hypoxic conditions, both in co-culture and monocultures (**Figure 4.15C**). Similarly, genes linked to chemotaxis and phagocytosis activity of GAMs were also increased, suggesting enhanced cytoskeletal remodelling and motility of myeloid cells, potentially supporting their migration and clearance of necrotic debris [54,106]. In contrast, hypoxia led to the downregulation of IFN-responsive, transitory and ribosomal (Ribo-GAMs) gene signatures (**Figure 4.15C**), which is consistent with previous studies showing hypoxia-mediated repression of ribosomal biogenies and RNA processing genes [136]. Next, to better understand the regulation of those markers in microglial cells, TF motif analysis was performed on promoters of hypoxia affected myeloid marker genes. As expected, binding sites for known hypoxia-responsive TFs were detected in promoters of hypoxia upregulated genes, including HIF-1/2A along with myc-associated factor X (MAX), runt-related transcription factor (RUNX), nuclear factor kappa-light-chain-enhancer of activated B cells (NF-κB), activator protein 1 (AP1), and others (**Figure 4.15D**). In contrast, the promoters of downregulated genes were enriched for interferon stimulated

response element (ISRE), B-cell lymphoma 6 (BCL6) and ETS Variant Transcription Factor 1 (ETV1) motifs (**Figure 4.15D**).

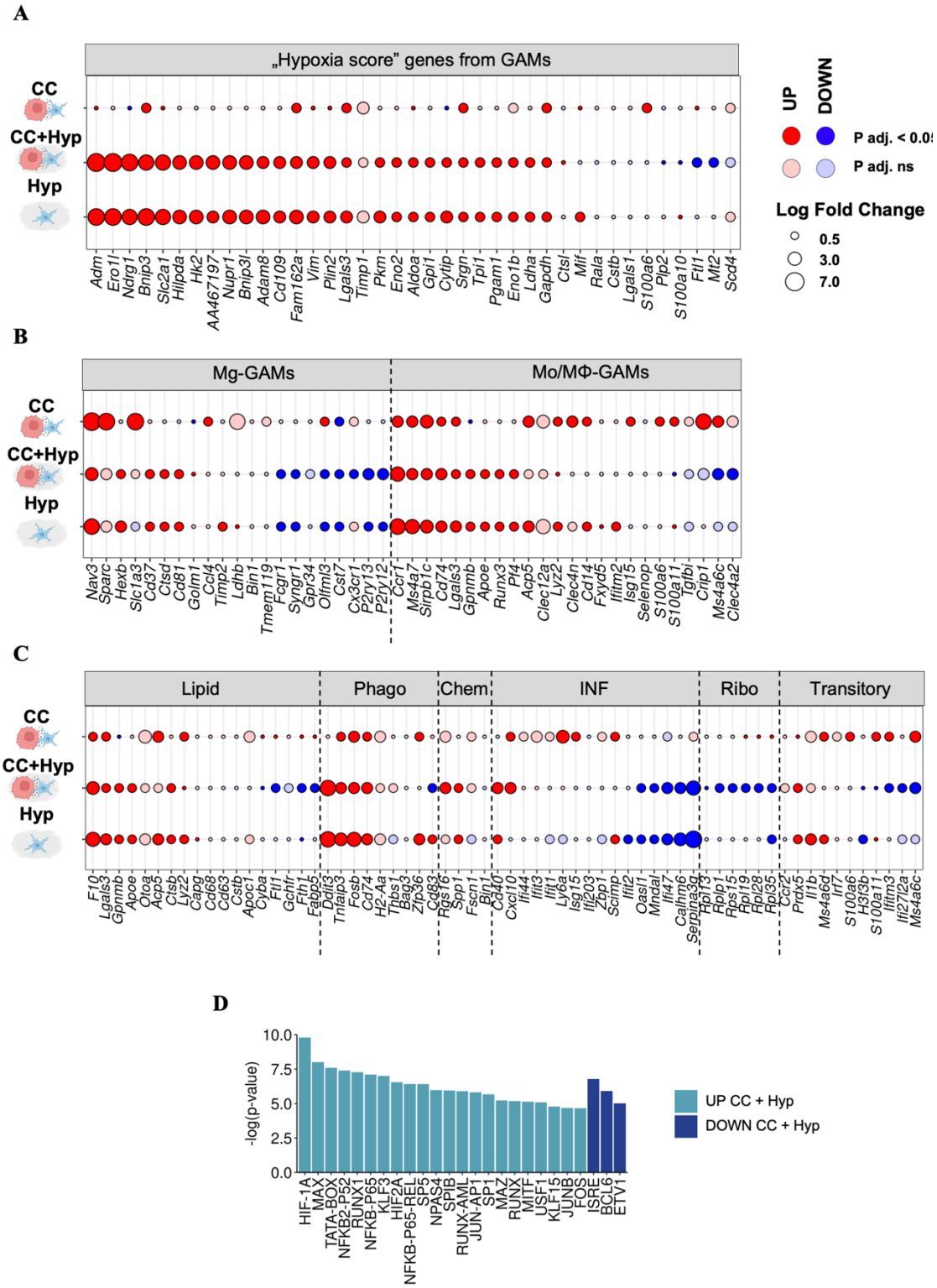


**Figure 4.15. Hypoxia dysregulates the expression of multiple monocytic and microglial GAM subcluster marker genes in BV2 cells. (A-C)** Gene expression changes in BV2 cells in response to co-culture with glioma GL261 cells in normoxia (CC), in response to co-culture with glioma GL261 cells in hypoxia (CC+Hyp) and in response to hypoxia only (Hyp) are shown for **(A)** "hypoxia score" genes for GAMs, **(B)** Mg-GAMs and Mo-GAM marker genes, **(C)** myeloid marker genes representing specific subpopulations of Mo-GAMs, including lipid, phagocytic (Phago), chemotactic (Chem), interferon (IFN),

ribosomal (Ribo) or transitory monocytes. The size of the circle indicates the fold change in a particular comparison. Dark blue and red colours indicate statistically significant gene expression changes (with p adjusted value < 0.05), while pale blue and pale red colours indicate non-significant regulation (with p adjusted value > 0.05). **(D)** Transcription factors motif enrichment analysis for promoters of differentially changed genes from (A-C).

To verify if the above findings on hypoxia-dependent gene expression in glioma co-culture were specific to BV2 cells, a similar analysis was carried out in an alternative co-culture model using bone marrow-derived macrophages (BMDMs), which were differentiated from monocytes and expressed characteristic macrophage markers, including *Itgam*, *Adgre1* and *Cd68* (**Figure 4.16A**). The direct BMDMs-GL261 co-cultures have been carried out. Similarly, as BV2 cells, BMDMs exhibited increased expression of hypoxia-responsive genes (**Figure 4.16B**). Most Mg-GAM markers were downregulated under hypoxia, while Mo/Mφ-GAM-associated genes were either up or downregulated (**Figure 4.16C**). Regarding specific GAM phenotype-associated genes, hypoxia induced the upregulation genes involved in phagocytosis and lipid metabolism under both co-culture or monoculture conditions, while genes related to interferon responses were predominantly downregulated (**Figure 4.16D**). Moreover, the hypoxia-induced upregulation of phagocytosis-related genes was functionally validated using a phagocytosis assay. BMDMs were exposed to hypoxic conditions or stimulated with LPS (as positive control for phagocytosis). Under both conditions, BMDMs exhibited enhanced phagocytic activity, as evidenced by an increased uptake of fluorescent latex beads (**Figure 4.16E-F**). Overall, the data confirmed that hypoxic stress dysregulates the expression of many GAM markers in both BV2 and BMDM cells, affecting the functions of multiple myeloid cell populations within the tumour microenvironment.

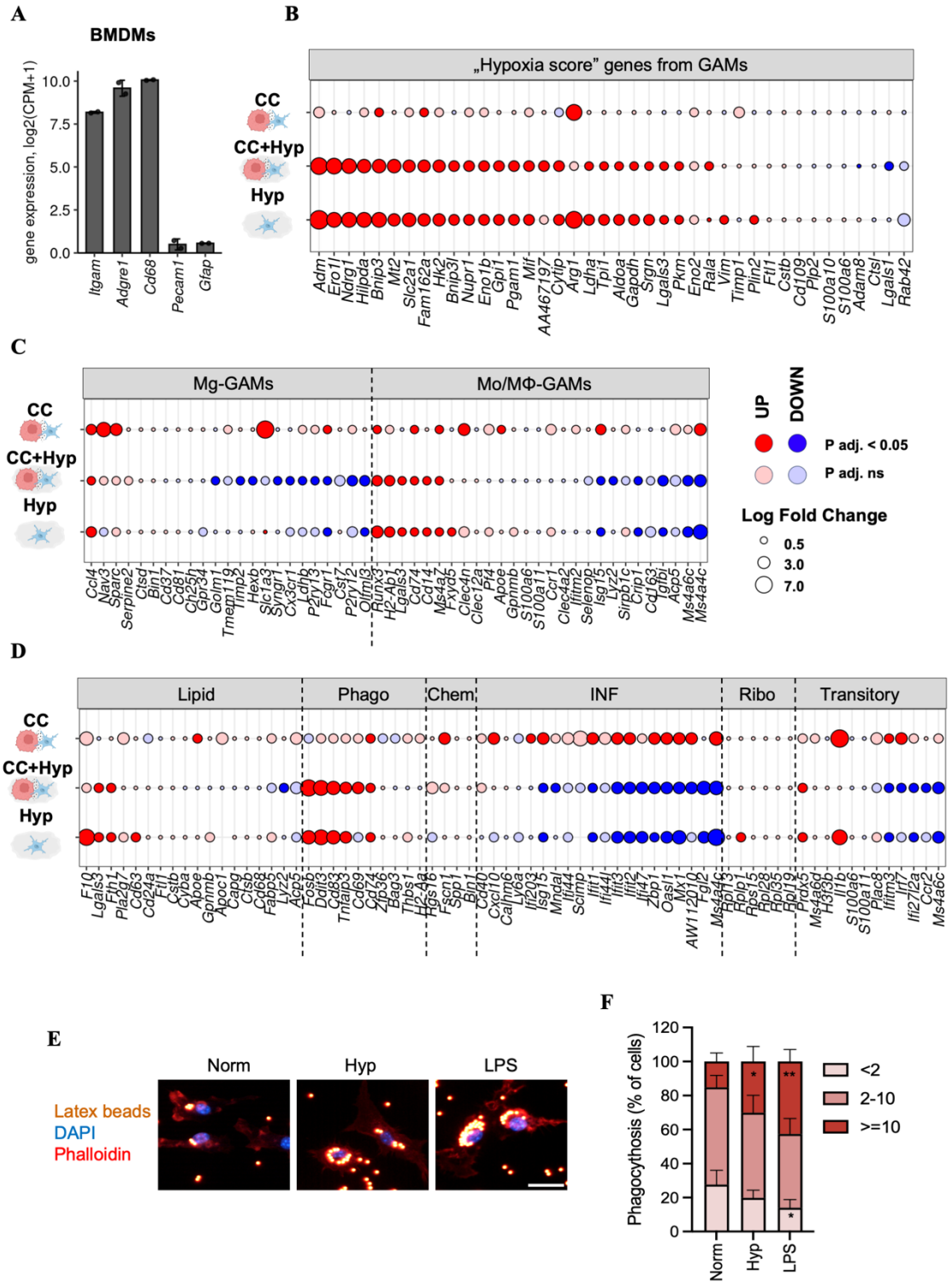


**Figure 4.16. Hypoxia dysregulates the expression of multiple monocytic and microglial GAM subcluster marker genes in BMDM cells. (A)** Gene expression levels of selected cell-type markers in BMDM cells. A bar plot shows $\log_2$-transformed counts per million (CPM+1) for canonical BMDM markers (*Itgam, Adgre1, Cd68*) along with endothelial marker (*Pecam1*), and astrocytic marker (*Gfap*) used as negative controls in RNAseq dataset. Data are shown as mean ± SD from two replicates. **(B-D)** Gene expression changes in BMDM cells in response to co-culture with glioma GL261 cells in normoxia (CC), in response to co-culture with glioma GL261 cells in hypoxia (CC+Hyp) and in response to hypoxia only (Hyp) are shown for **(B)** genes from hypoxia score in GAMs, **(C)** top Mg-GAM and Mo-GAM marker genes, **(D)** top myeloid marker genes representing specific subpopulations of Mo-GAMs, including lipid, phagocytic (Phago), chemotactic (Chem), interferon (IFN), ribosomal (Ribo) or transitory monocytes.

The size of the circle indicates the fold change in a particular comparison. Dark blue and red colours indicate statistically significant gene expression changes (with p adjusted value < 0.05), while pale blue and pale red colours indicate non-significant regulation (with p adjusted value > 0.05). **(E)** Phagocytosis of fluorescently labelled latex beads (red dots) by BMDMs in response to normoxia, hypoxia (< 0.1% $O_2$) and LPS conditions. The representative pictures of phagocytic BMDMs were taken using fluorescent microscope after staining actin cytoskeleton with phalloidin and nuclei with DAPI. Scale bar, 10 μm. **(F)** Quantification of phagocytic activity of BMDM cells. BMDMs taking up <2, 2–10, or >10 fluorescent beads were counted in 15 randomly selected fields. Data are presented as the mean ± SD from three experiments. Student's t test was used to determine statistical significance.

Since the above data clearly show that hypoxia strongly influences the expression the lipid-associated genes in both BV2 cells and in BMDMs (**Figure 4.15C**, **Figure 4.16D**), other genes involved in key lipid metabolic processes, including cholesterol biosynthesis, fatty acid (FA) synthesis and uptake, triacylglycerol (TG) synthesis, lipid storage or transport, lipolysis and lipophagy were analysed (**Figure 4.17A-B**). Many genes related to cholesterol biosynthesis were downregulated in BMDMs under hypoxia, whereas in BV2 cells showed a mixed pattern, for example *Fdft1* was upregulated, while *Dhcr7* was downregulated in response to hypoxia. The regulation of FA synthesis genes was mixed. While some genes, such as *Nr1h2* and *Srebf1*, were upregulated in both cell types, others like *Fasn* and *Acaca* were downregulated under hypoxic conditions. Genes associated with FA uptake (*Fabp3/4/5/7*) were largely downregulated in both cell lines in response to hypoxia. Interestingly, genes involved in TG synthesis, such as *Lpin1/2/3* and *Gpat3*, were consistently upregulated under hypoxia in both cell types, suggesting enhanced lipid droplet formation. Supporting this observation, genes related to lipid storage (e.g. *Lgals3*, *Plin2*, *Plin3*, *Hilpda*, *Soat1*) were also upregulated in both BV2 cells and BMDMs. Furthermore, genes associated with lipid transport were upregulated by hypoxia, particularly in BV2 cells, indicating increased lipid trafficking. Finally, genes associated with the lipid breakdown processes, including lipolysis and lipophagy (e.g. *Ppard*, *Lamp2*, *Map1lc3b*), were also mainly upregulated under hypoxia, suggesting increased lipid turnover in these cells. Overall, these results were indicating that hypoxia induces widespread reprogramming of lipid metabolic genes in myeloid cells, supporting lipid accumulation, transport and degradation.

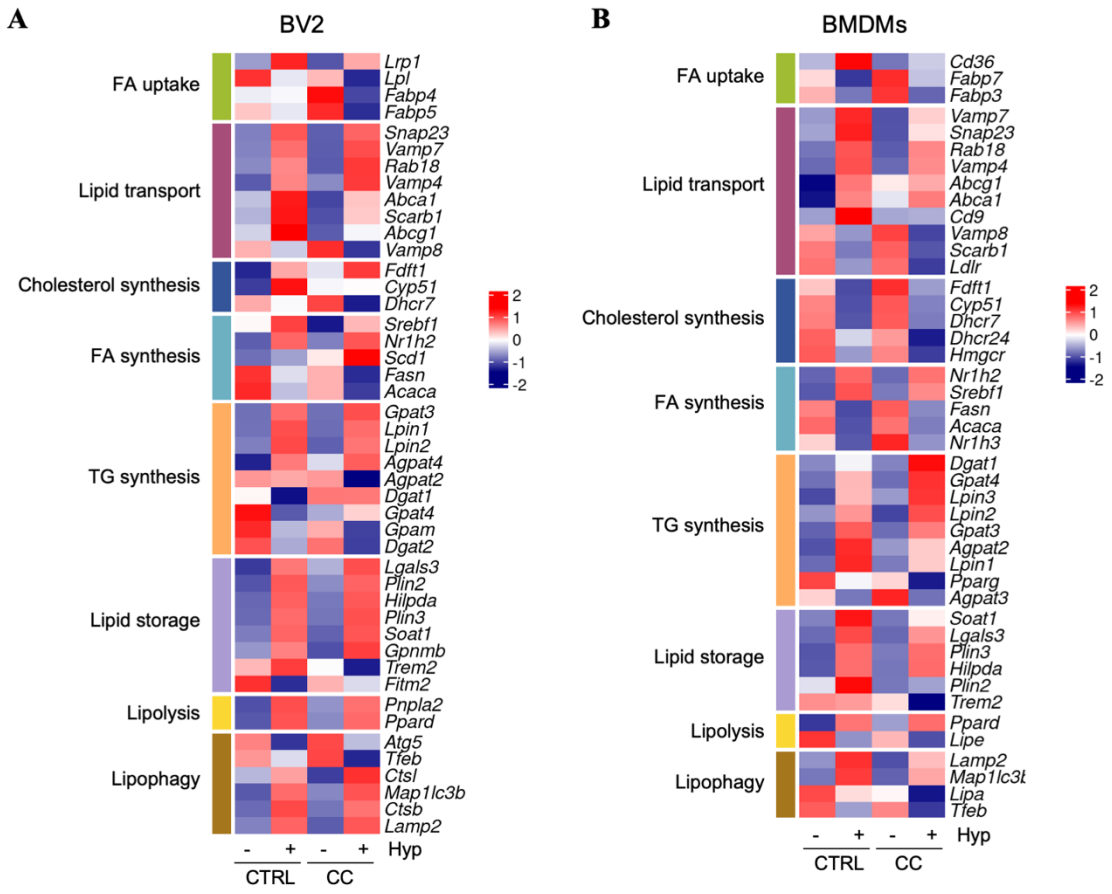


**Figure 4.17. Expression of lipid-related genes in GAMs exposed to hypoxia. (A-B)** A heatmap showing z-score–normalised expression profiles of genes associated with distinct lipid metabolic processes, which were significantly changed (adj. p-value<0.05) in response to hypoxia (< 0.1% $O_2$) compared to normoxia in at least one treated culture condition (Ctrl or CC) in **(A)** BV2 and **(B)** BMDM cells. FA – Fatty acid; TG – Triacylglycerol.

## 4.5. Characterizing the chromatin accessibility in BV2 microglia cells under glioma and hypoxic conditions

As shown in this study (**Figure 4.1** - **Figure 4.3**) and supported by previous findings, hypoxic stress can substantially remodel the chromatin landscape in cancer cells, leading to widespread changes in gene regulation [59,136,140]. To determine whether similar epigenetic changes occur in myeloid cells, the impact of hypoxia on chromatin regulation in BV2 microglia was examined *in vitro*. Initial immunofluorescence analysis confirmed that hypoxia modulated key histone H3 methylations in microglia co-cultured with glioma cells, resulting in a global significant increase in H3K27me3 (**Figure 4.18A** and **Figure 4.18C**) and H3K9me3 marks (**Figure 4.18B** and **Figure 4.18D**).

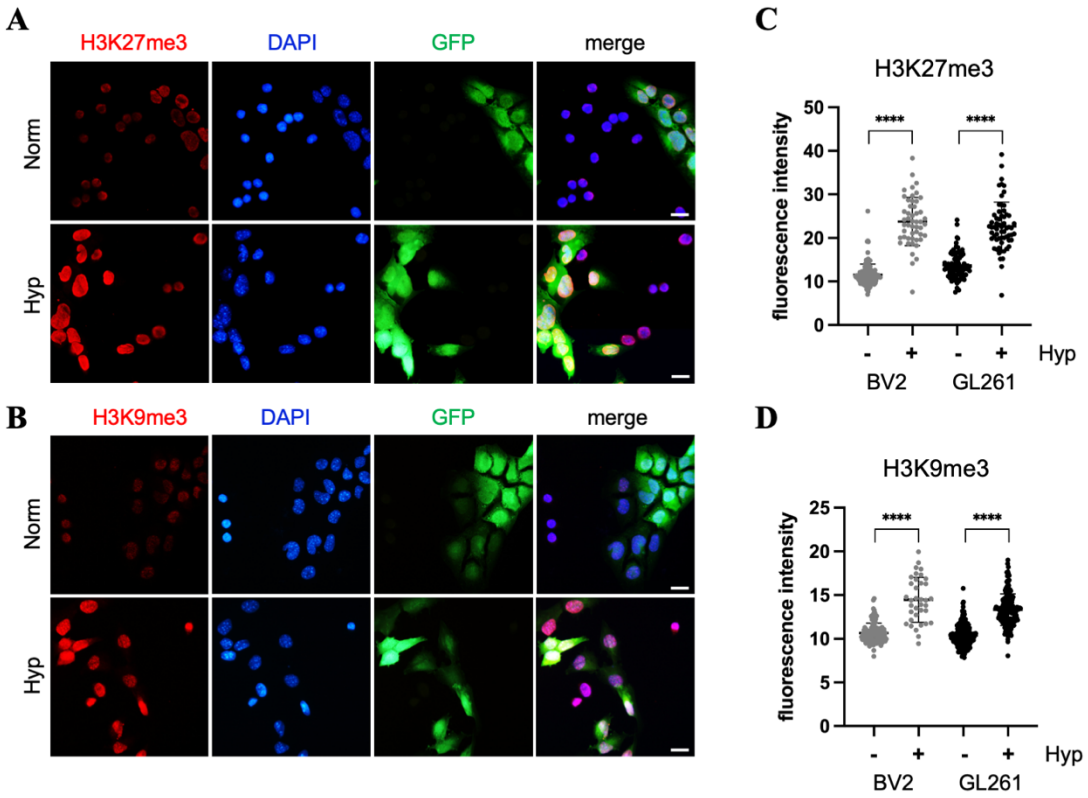


**Figure 4.18. Histone H3 methylation changes in microglia co-cultured with glioma cells. (A-B)** Immunofluorescent staining of **(A)** H3K27me3 or **(B)** H3K9me3 (red) and nuclei (DAPI, blue) was performed in BV2-GL261 co-cultures in hypoxia (Hyp) and normoxia (Norm). Representative images show BV2 (microglia) and GL261 (glioma GFP+, green) cells. Scale bar, 20 µm. **(C-D)** Quantitation of nuclear fluorescence intensity of **(C)** H3K27me3 staining from (A) or **(D)** H3K9me3 staining from (B) was preformed and five different fields of view were analysed in each condition. Unpaired two-tailed student's t test was used to determine statistical significance. A representative experiment of three independent biological repeats is shown.

Next, the chromatin accessibility changes were assessed in normoxic and hypoxic condition using ATAC-seq assay on formaldehyde-fixed cells. Interestingly, the PCA of ATAC-seq peaks data revealed that chromatin accessibility in BV2 cells was more strongly influenced by co-culture with glioma cells than by hypoxia, as reflected by the separation along the PC1 axis versus PC2 axis, respectively (**Figure 4.19A**). A total of 26718 ATAC-seq peaks, representing regions of open chromatin, were identified across all experimental conditions, of which 0.1% were unique to Ctrl_N, 6.5% to CC_N, 14.5% to Ctrl_H and 11.3% to CC_H (**Figure 4.19B**). Next, the differential open region analysis was preformed to assess the site-specific changes in BV2 cells. In normoxic conditions, co-culture with glioma cells led to a greater number of regions with increased chromatin accessibility (2173 peaks) than regions with decreased accessibility (716 peaks) (**Figure 4.19C**). When co-cultures were exposed to hypoxia, chromatin accessibility in BV2 cells

was further altered, with 4418 peaks showing increased accessibility and 3885 peaks showing decreased accessibility in comparison to normoxic co-culture (**Figure 4.19D**). For hypoxic BV2 from monoculture, 1831 peaks were increased and 1514 were decreased (**Figure 4.19E**).

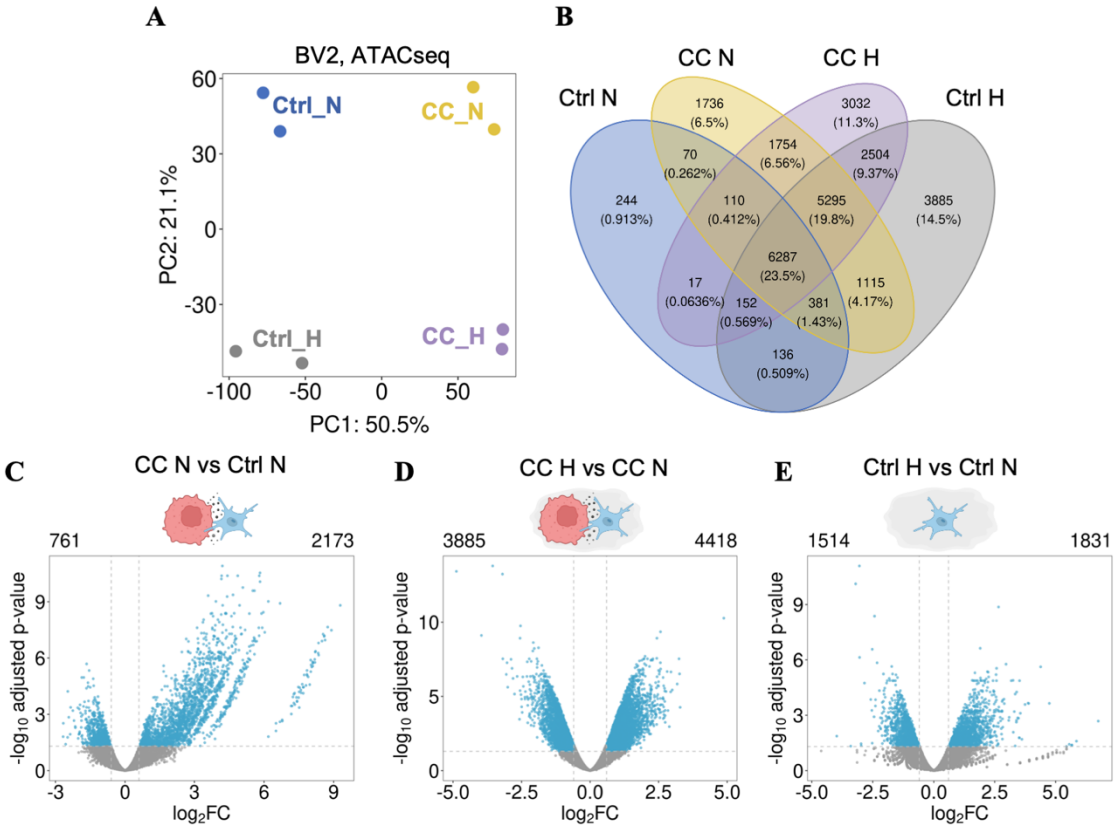


**Figure 4.19. Differential chromatin accessibility analysis in BV2 cells exposed to glioma cells and hypoxia. (A)** A principal component plot on identified ATAC-seq peaks in BV2 cells treated with hypoxia (<0.1% $O_2$) or normoxia in the presence (CC) or absence (Ctrl) of glioma cells**. (B)** Venn diagram showing specific or common ATAC-seq peaks detected in all conditions tested, as indicated. The percentage of peaks in the total amount of peaks is shown in brackets for each condition. **(C-E)** Volcano plots showing differentially altered ATAC-seq peaks in glioma co-cultured BV2 cells versus monocultures **(C)**, glioma co-cultured BV2 cells in hypoxia versus normoxia **(D)**, BV2 monocultures in hypoxia versus normoxia **(E)**. Each point on the plot corresponds to one peak. Statistically significant peaks with FDR < 0.05 and |log2 fold change| ≥ 0.6 are marked in blue. The numbers of chromatin accessibility peaks significantly increased or decreased are written above the plots.

Further, genomic annotation of differentially altered regions was examined. In the normoxic co-cultures, increased accessibility was predominantly found at promoter, intronic, and distal intergenic regions (**Figure 4.20,** left panel), whereas hypoxia alone primarily reduced the promoter accessibility (**Figure 4.20**, right panel). When both factors were applied simultaneously (hypoxia and co-culture), a similar distribution of upregulated and downregulated peaks across these genomic regions was observed

(**Figure 4.20**, middle panel). A more detailed analysis of upregulated peaks at the promoter regions revealed that out of 1680 CC_Hyp UP peaks, only 109 (6.49%) were also increased in response to hypoxia alone, whereas the majority - 1515 peaks (90,18%) - required combined exposure to both hypoxia and glioma to become more accessible (**Figure 4.20B**). In contrast, among 1439 promoter-associated downregulated peaks, 483 (33.56%) were also reduced by hypoxia alone, while 951 peaks (66,09%) were specifically repressed only under the combined influence of hypoxia and glioma co-culture (**Figure 4.20C**). These findings indicate that hypoxia alone had a stronger influence on reducing the promoter accessibility than on increasing it. On the other hand, the gaining of more accessible promoter regions appeared to be primarily driven by the synergistic effect of both hypoxic stress and interaction with glioma.

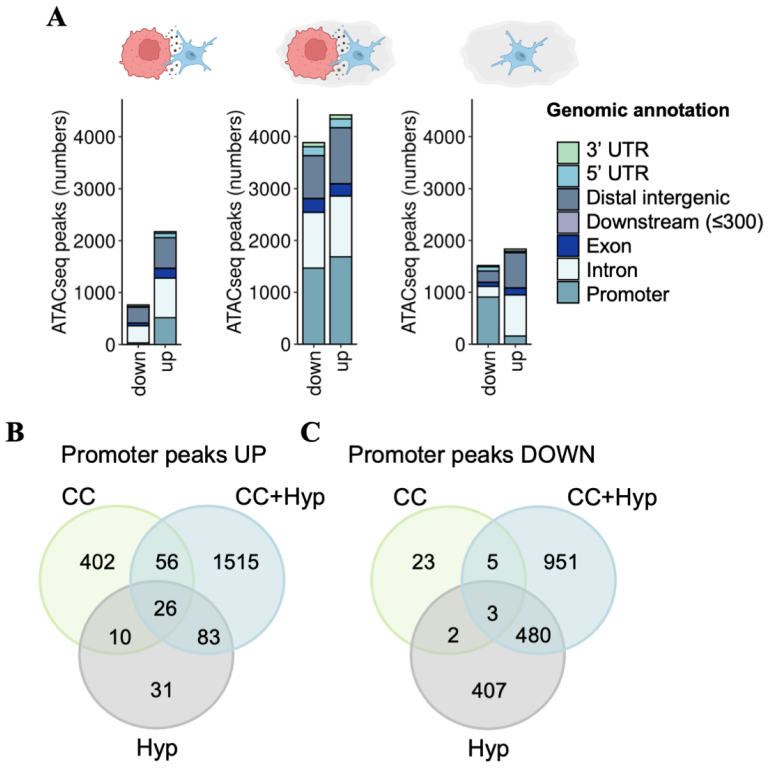


**Figure 4.20. Genomic annotation analysis of ATAC-seq peaks. (A)** Bar plots showing differentially regulated ATAC-seq peak counts annotated to specific genomic regions, as indicated in the figure legend. Three differential analyses were performed for chromatin accessibility in BV2 cells: in response to co-culture with glioma GL261 cells in normoxia (CC; left graph), BV2 in response to co-culture with glioma GL261 cells in hypoxia (CC+Hyp; middle graph) and in response to hypoxia only (Hyp; right graph). **(B-C)** Venn diagrams summarising common and distinct significantly increased **(B)** or decreased **(C)** ATAC-seq peaks at promoters in BV2 cells.

To determine whether HIF signature ("HIF metagene" score) was reflected in chromatin accessibility landscape in BV2, ATAC-seq signal was examined across promoter and gene body region of HIF-inducible genes [139]. While hypoxia did not significantly increase accessibility at promoters alone (**Figure 4.21A**, left panel), a notable increase of ATAC-seq signal was observed when the analysis included also gene bodies (genic regions, **Figure 4.21A**, left panel). These findings suggest that hypoxia-driven chromatin changes at HIF target genes predominantly occur outside of promoters. This finding was further supported by the transcription factors (TFs) motif enrichment analysis of peaks with increased accessibility under hypoxia. In monocultured hypoxic cells, HIF-1A and HIF-2A motifs were enriched specifically in genic regions (promoters and gene bodies), but not in promoters only (**Figure 4.21B**). Moreover, several other known hypoxia-responsive TFs motifs were detected in genic peaks of BV2 cells after hypoxia, including those for AP1 (FOS/JUN family), ATF1-4, FRA1-2, CHOP, and others (**Figure 4.21B**) [27,141]. Notably, TF motifs specifically enriched in hypoxic co-culture conditions compared to monocultures, included several factors previously linked to myeloid cell function (**Figure 4.21B**). Among these the most interesting were motifs recognised by KLF4 and KLF3, both associated with anti-inflammatory phenotype [142,143]; KLF6, early growth response 1 (EGR1) and specificity protein 1 (SP1) which promote inflammatory gene programs [143–145]; KLF9 involved in regulating oxidative-stress responses in macrophage [146]; and mothers against decapentaplegic homolog 3 (SMAD3), the downstream effector of TGF-β signalling that regulates quiescent microglial phenotype and homeostatic identity [147]. GO analysis of biological processes, performed on genes with significantly decreased chromatin accessibility at their genic regions in hypoxic BV2 co-culture, indicated enrichment of terms related to mitotic cell division, GTPase activity, DNA replication and various RNA processing mechanisms, similar to RNA-seq data (**Figure 4.21C**). For increased genic ATAC-seq peaks, processes associated with histone modification, dendrite development, autophagy, vesicle organisation were showed (**Figure 4.21D**).

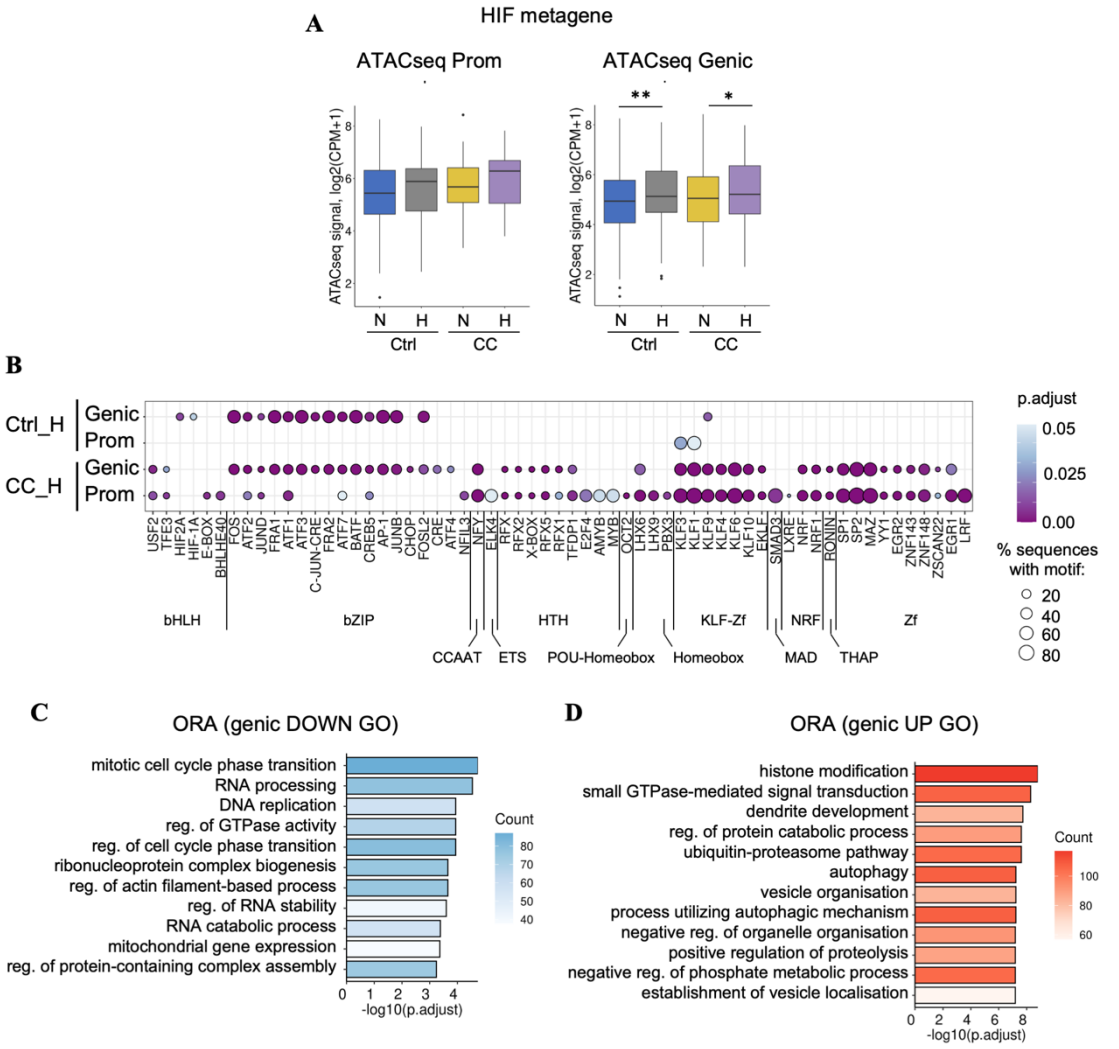


**Figure 4.21. Functional analysis of chromatin changes in BV2 cells under hypoxic conditions.** **(A)** Analysis of HIF metagene score [139] in ATAC-seq pekas at the gene promoter (left panel) and promoters and gene bodies (denoted as genic, right panel) in BV2 cell in hypoxia. The average ATAC-seq signal of the HIF metagene score is represented as read counts per million. Student's t test was used to determine statistical significance. **(B)** Enrichment of TF motifs in ATAC-seq peaks at the gene promoter or genic regions that increased in BV2 cells treated with hypoxia in co-culture with GL261 (CC) or alone (Ctrl) in comparison to respective CC or Ctrl normoxic cells. Circle size indicates the percentage of sequences in the subset with the motif, while the colour gradient reflects the significance of enrichment. All indicated enriched TF motifs are statistically significant (p adjusted <0.05). At the bottom part of the graph, the TFs are additionally grouped into respective TF families: bHLH - basic Helix-Loop-Helix; bZIP - basic Leucine Zipper; CCAAT - TF that specifically bind to the CCAAT box; ETS - E26 Transformation-Specific; HTH - Helix-Turn-Helix; POU-Homeobox - TFs that contain both POU-specific domain and a homeodomain; Homeobox - TF that contain homeodomain; KLF-Zf - Krüppel-Like Factors, Zinc Finger; MAD – 'mothers against decapentaplegic'; NRF - Nuclear Respiratory Factor; THAP - Thanatos Associated Proteins; Zf - Zinc Finger. **(C-D)** Overrepresentation analysis showing GO processes in significantly decreased **(C)** or increased **(D)** genic ATAC-seq peaks. The top 15 GO processes were selected based on the lowest adjusted p-values, and closely related terms were merged using REVIGO. The gradient of colours indicates the number of genes in each associated process.

Since the data above showed that glioma co-culture has a stronger impact on the chromatin accessibility in microglia under hypoxic conditions (**Figure 4.20A**), the peaks and associated biological processes, which were more enriched in the hypoxic co-culture compared to hypoxic monocultures, were exanimated. Out of 4418 peaks increased in co-cultured hypoxic BV2, 2257 (51,09%) were more enhanced in hypoxia co-culture in comparison to hypoxic BV2 monocultures (**Figure 4.22A**). For 3385 significantly decreased chromatin accessibility regions in co-culture, 1638 (48,39%) were even more decreased in hypoxia co-culture in comparison to hypoxic BV2 monocultures (**Figure 4.22A**). Genomic annotation of these peaks indicated that, in BV2 cells, the combined exposure to hypoxia and glioma co-culture - relative to hypoxia alone - was associated with increased chromatin accessibility at promoter regions and reduced accessibility within intronic and distal intergenic sites. GO analysis of promoter-associated peaks specifically altered in hypoxic co-cultured BV2 cells revealed enrichment of pathways related to autophagy, histone modifications, and other cellular processes (**Figure 4.22C-D**). Interestingly, peaks with reduced chromatin accessibility were associated with pathways involved in neuroinflammatory, defence responses, and leukocyte activation (**Figure 4.22C-D**). These findings suggest that combined exposure to hypoxia and glioma may promote the immunosuppressive phenotype in BV2 cells by reducing chromatin accessibility at genes involved in immune activation.

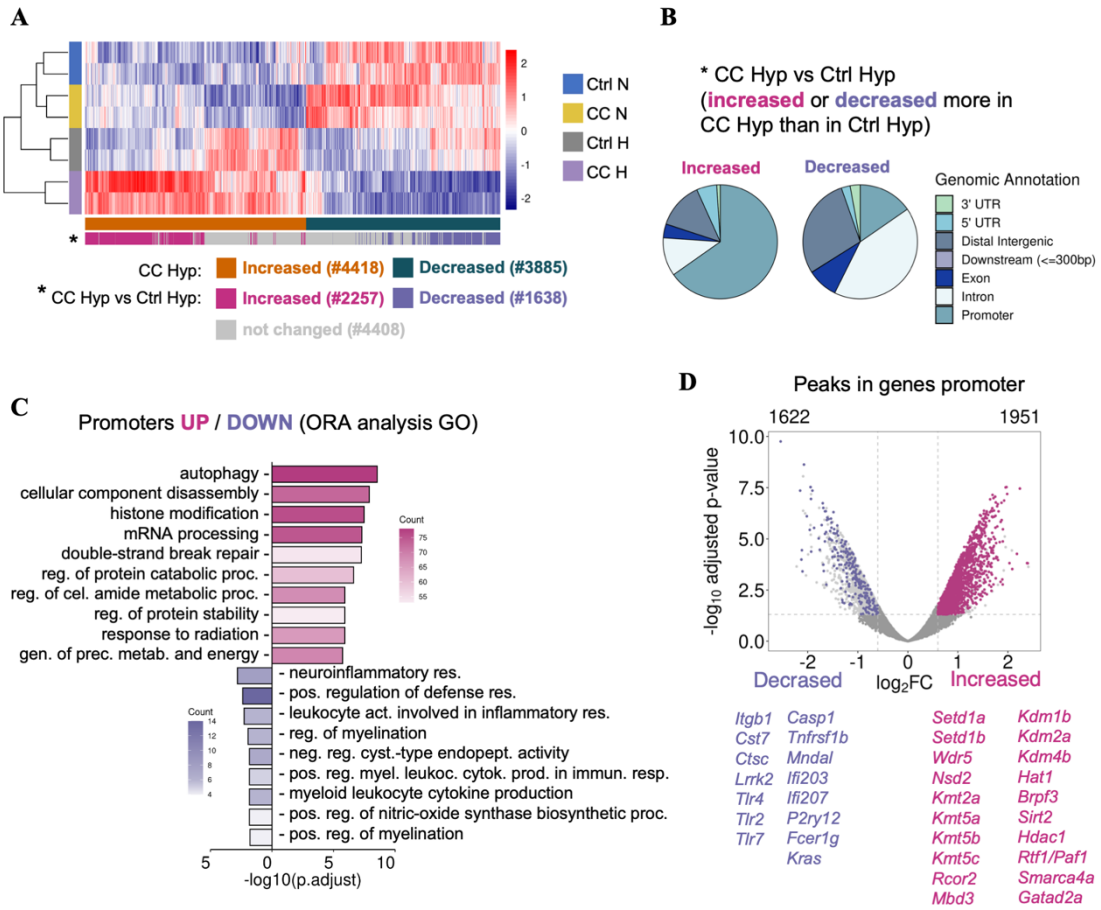


**Figure 4.22. Changes in chromatin accessibility in BV2 cells enhanced by combined glioma co-culture in hypoxic conditions when compared to hypoxia alone. (A)** A heatmap showing z-scores for peaks increased (orange) or decreased (dark green) in BV2 cells co-cultured (CC) with glioma cells. Peaks which were additionally increased or decreased in CC versus Ctrl hypoxic BV2 cells are projected in magenta or pale blue, respectively. **(B)** A pie chart showing differentially regulated ATAC-seq peaks from (A) annotated to specific genomic regions, as indicated in the figure legend. **(C)** Overrepresentation analysis showing GO processes in peaks which were additionally decreased or increased in CC versus Ctrl hypoxic BV2 promoter regions. The top 15 GO processes were selected based on the lowest adjusted p-values; closely related terms were merged using REVIGO. The colour gradient reflects the gene count in each associated process. **(D)** A volcano plot showing differentially altered ATAC-seq peaks occurring at promoter regions in glioma co-cultured (CC) microglial cells in hypoxia versus normoxia (numbers written above the plot). Each point on the plot corresponds to one peak. Statistically significant peaks are defined as FDR < 0.05 and |log2 fold change| ≥ 0.6. Additionally, the promoter peaks that were even more decreased or increased in CC versus Ctrl in hypoxic conditions are projected in pale blue or magenta, respectively. Examples of genes associated with those peaks are written below the plot.

## 4.6. Concordant hypoxia-dependent transcriptomic and epigenetic changes in glioma-cocultured BV2 cells

To assess the correspondence between changes in gene expression and chromatin accessibility, RNA-seq and ATAC-seq datasets were compared in glioma-co-cultured BV2 cells. For ATAC-seq data, a maximum peak values per gene were used while assigning peaks to genes. Pearson and Spearman correlation coefficients ($r = 0.24$) revealed a moderate but statistically significant correlation, indicating that a subset of genes was consistently affected at both the transcriptional and chromatin accessibility levels (**Figure 4.23A**). The detailed analysis showed that 24.76% of upregulated genes and 17.76% of downregulated genes in response to hypoxia also displayed corresponding changes in chromatin accessibility (**Figure 4.23B**). The top biological processes identified by over-representation analysis of commonly upregulated genes included not only the response to low oxygen levels, but also a range of diverse cellular processes (**Figure 4.23C**). Among the downregulated genes, enrichment was observed for processes typically associated with hypoxic suppression, including ribosome biogenesis, DNA replication, cell cycle division (**Figure 4.23D**). However, a closer investigation of genes which were additionally decreased in BV2 cells co-cultured with glioma in hypoxia when compared to hypoxia alone revealed only 10 genes (**Figure 4.23E**), which were related with the processes such as semaphorin-plexin signalling pathway involved in neuron projection guidance, signal release and myeloid leukocyte differentiation.

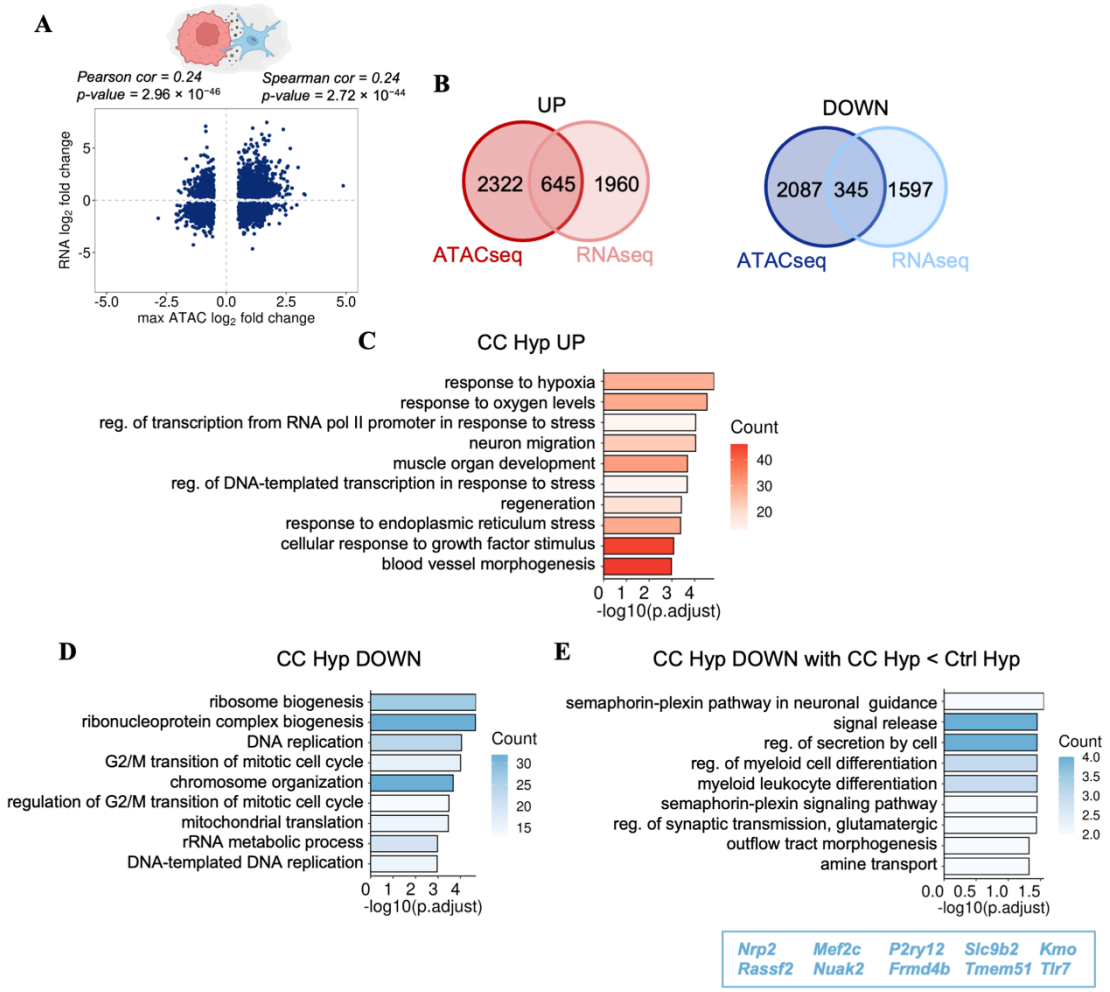


**Figure 4.23. Concordant hypoxia-dependent transcriptomic and epigenetic changes in glioma-co-cultured BV2 cells. (A)** Dot plot showing the correlation of expression changes versus maximal ATAC-seq peak fold changes per gene. Pearson and spearman correlation coefficient values are shown above**. (B)** Venn diagrams showing concordantly upregulated (left panel) or downregulated (right panel) gene expression and corresponding genic ATAC-seq peaks in BV2 cells treated with hypoxic coculture with glioma cells. The rectangular frames indicate myeloid marker genes identified in the concordant ATAC-seq and RNA-seq changes. **(C-E)** Overrepresentation analysis showing GO processes in concordant (mRNA and chromatin accessibility changes) upregulated **(C)** or downregulated **(D)** genes in BV2 cells co-cultured with glioma cells in hypoxic conditions. In **(E)** are shown processes that were downregulated in hypoxic co-cultures (CC Hyp) and additionally downregulated in hypoxic co-cultures in comparison to hypoxic monocultures (CC Hyp < Ctrl Hyp). The box shows the genes that were identified.

Since RNA-seq data revealed changes in numerous genes associated with myeloid cell identity and function, particularly those involved in lipid metabolism (**Figure 4.17**), in the next step the concordant regulation of gene expression and chromatin accessibility in genes from particular GAM clusters and lipid metabolic pathways were assessed. Among the concordantly upregulated genes, 18 were identified as defining different GAM-associated markers, especially those linked to hypoxia-related and lipid-related GAMs (**Figure 4.24A**, red). In addition, many other genes involved in lipid metabolic

processes also showed alterations in chromatin accessibility (**Figure 4.24B**, red). One example is *Lgals3*, which exhibited significantly increased expression and chromatin accessibility at the promoter region in BV2 cells under hypoxic conditions, both in glioma co-culture and monoculture settings (**Figure 4.24C**). This genes encodes Galectin-3 (Gal-3) and is involved in facilitating cancer cell motility and invasiveness, as well as driving an immunosuppressive state in microglia [148]. To better understand the mechanism of transcriptional regulation by changes in chromatin accessibility, the ATAC-seq peaks were scanned for the presence of specific TF motifs. The biding motifs for AP-1 (formed by FOS and JUN family proteins) and ATF3 TFs were found and are known to play important roles in oncogenesis, anti-inflammatory responses and lipid metabolism regulation [149–151]. Expression of *Atf3* was also increased under hypoxic condition, which may further regulate immunosuppressive phenotype of myeloid cells. Additionally, both AP-1 and ATF3 are known to be active under low-oxygen tensions and may contribute significantly to the regulation of hypoxic microglial functions [152,153]. Another example, *Gpnmb* (**Figure 4.24D**), was shown to be involved in the modulation of the pro-tumorigenic phenotype of GAMs and its deletion increased the pro-inflammatory response and reduced the tumour size [99]. The increased accessible chromatin region in the *Gpnmb* promoter was abundant with binding motifs for nuclear factor IB (NFIB) and NFIC, as well as SMAD2 and SMAD4, which mediate TGF-β signalling in both glioma cells and myeloid cells, promoting tumour invasion and an immunosuppressive phenotype [154].

For 32 downregulated GAM-associated marker genes in BV2 cells, only 5 (15.6%) had concordant changes in the chromatin accessibility (**Figure 4.24B**, blue). Among them was *P2ry12*, Mg-GAM marker gene, with almost complete loss of accessible chromatin in promoter region after glioma co-culture and hypoxic conditions (**Figure 4.24E**). Notably, the TFs which may potentially bind in this region include SPI1 (known as PU.1) and interferon regulatory factor 8 (IRF8), which play a key role in regulating microglia identity and maintenance of homeostasis [155]. Moreover, expression of *Spi1* was also significantly decreased in hypoxic condition based on the RNA-seq analysis, which may additionally contribute to the suppression of *P2ry12* under hypoxia. Motif for other TFs were also observed, and among them SRY-box 4 (SOX4) and ETS-family members are known to be hypoxia-responsive [103,156]. Another example with decreased chromatin accessibility and downregulated expression in hypoxic BV2 cells was *Olfml3* (**Figure 4.24F**). Co-culture with glioma cells increased the expression of

*Olfml3*, which was then decreased in response to hypoxic stress. Motif analysis of this peak at the 3'UTR region revealed an enrichment of TFs like SP1, IRF3 and ETS2, which are known to mediate the regulation of immune responses in myeloid cells[145,157,158].

Finally, the reported here GAM-associated marker genes showing coordinated regulation at both chromatin and transcriptomic levels in hypoxic co-cultures in BV2 cells (18 up and 5 down), were checked for the correlation with the hypoxic score in glioma-associated myeloid cells (GAMs) *in vivo,* using mouse and human GBM datasets from Antunes et al. (**Figure 4.24G**) [102]. The analysis revealed that the expression of certain genes, such as *P2ry12* and *Olfml3*, was negatively correlated with the hypoxic score, whereas *Gpnmb, Lgals3* and several known hypoxic TAM markers were positively correlated, either across the total TAM population or specifically within Mg-TAM subsets in all datasets. Several genes displayed opposite correlation patterns compared to those observed in the *in vitro* co-culture model under hypoxia (e.g. *Mndal*, *Cd37*, and *S100a11*). This may suggest that additional factors present in the tumor microenvironment *in vivo* may influence their regulation under hypoxic conditions.

A

| Concordant changes of myeloid markers genes | |
|---|---|
| Hypoxia-GAMs | *Aldoa Ldha Srgn Pgam1 Pkm Adm Bnip3l Ndrg1 Hilpda Nupr1* |
| Mg-GAMs | *Cd37 P2ry12 Olfml3 Cst7* |
| Mo/MΦ-GAMs | *S100a11* |
| Lipid-GAMs | *Gpnmb Lgals3 F10* |
| INF-GAMs | *Cxcl10 Mndal* |
| Phago-GAMs | *Cd74 Fosb Tnfaip3* |

B

| Concordant changes of lipid metabolism related genes | |
|---|---|
| FA uptake | *Lrp1* |
| Lipid storage | *Soat1 Hilpda Lgals3 Gpnmb* |
| Lipolysis | *Ppard* |
| Lipophagy | *Lamp2* |
| TG synthesis | *Lpin2* |
| Lipid transport | *Snap23* |

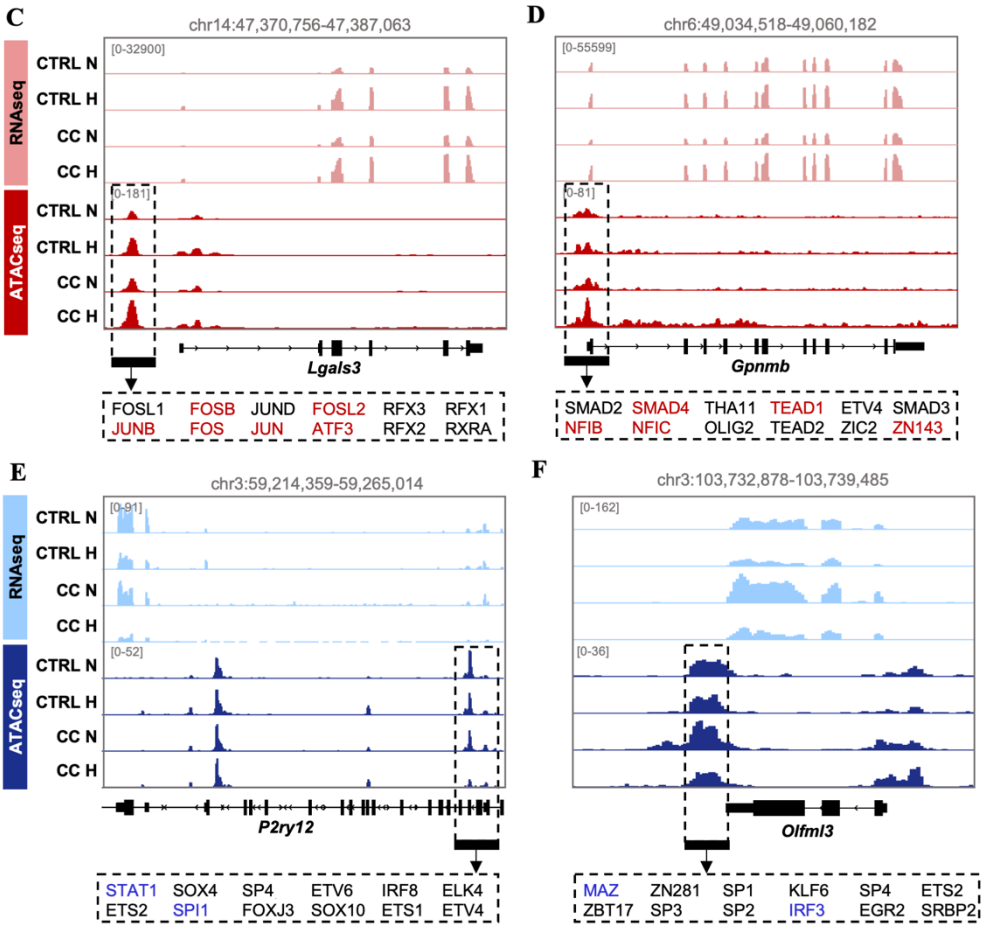


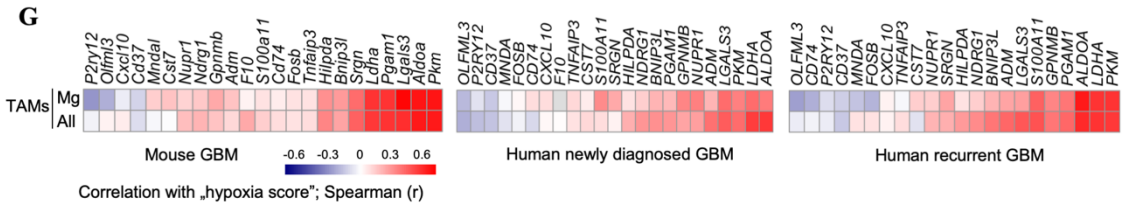


**Figure 4.24. Concordant RNA-seq and ATAC-seq changes of myeloid cell functional marker genes and lipid-related genes in hypoxic glioma-co-cultured BV2 cells. (A)** Table with concordantly changed myeloid markers genes from Figure 4.15A-C. **(B)** Table with concordantly changed lipid-related genes from Figure 4.17A. **(C-F)** The mRNA expression (RNA-seq) and ATAC-seq profiles (from Integrative Genomics Viewer, IGV) of selected concordantly upregulated genes including **(C)** *Lgals3* and **(D)** *Gpnmb* and downregulated genes including **(E)** *P2ry12* and **(F)** *Olfml3* in BV2 cells. The FIMO analysis was used for the selected ATAC-seq peaks, to identify available motifs for TFs, as indicated in rectangular boxes under each gene. The IGV tracks show the average from two biological repeats.

**(G)** Heatmaps representing the correlation between hypoxia score and concordantly hypoxia-regulated genes at the expression and chromatin level indicated in Figure 4.23B in scRNA-seq datasets for mouse TAMs (left panel), TAMs in human newly diagnosed GBM (middle panel) and TAMs in human recurrent GBM (right panel).

## 4.7. Epigenetic regulation of hypoxia-induced lipid accumulation in GAMs

As previously demonstrated by us and others, hypoxia increases histone methylation, due to impaired activity of oxygen-dependent histone demethylases [72,136]. In contrast, histone acetylation has been shown to decrease under hypoxic conditions, primarily due to reduced levels of acetyl-CoA and increased activity of HDACs [77]. To confirm whether this also applies to myeloid cells, CUT&RUN assay was preformed and the levels of H3K27ac in BV2 cells were assessed. As expected, a global reduction in H3K27ac was observed under hypoxic conditions across most genomic loci both in monocultured BV2 cells and in glioma co-cultures (**Figure 4.25A-B**), which was also confirmed by western blot on total cell lysates (**Figure 4.25C**). To corroborate the possibility that the loss of acetylation is involved in the regulation of expression of GAM markers, the histone acetylation levels were restored pharmacologically. Therefore, BV2 cells were treated with the pan-HDAC inhibitor (HDACi), Panobinostat, and subsequently exposed to hypoxic conditions. Interestingly, hypoxia-induced upregulation of *Lgals3* was attenuated by HDACi treatment, both at the mRNA and protein levels (**Figure 4.25D-F**). In contrast, Panobinostat treatment restored the expression of the hypoxia-repressed microglial marker *Tmem119*, while expression of *P2ry12* was not changed (**Figure 4.25D**).

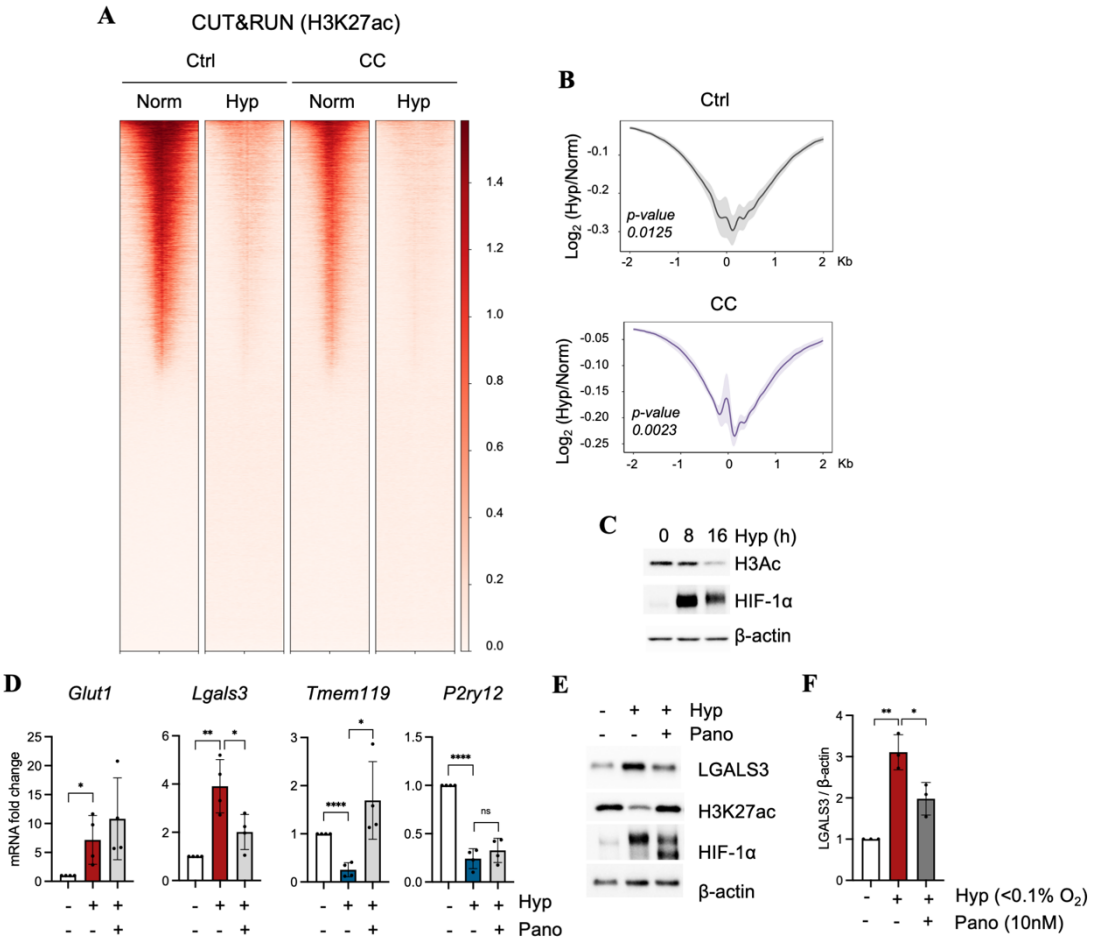


**Figure 4.25. Hypoxia and HDACi affects expression of myeloid markers in BV2 cells.** **(A)** Heatmap showing H3K27ac enrichment within ± 2 kb of transcription start sites (TSS) in BV2 cells cultured either alone (Ctrl) or co-cultured with GL261 glioma cells (CC) under normoxic (21% $O_2$) or hypoxic (< 0.1% $O_2$) conditions. **(B)** Profile plot showing the ratio of H3K27ac signal under hypoxic versus normoxic conditions within ±2 kb of TSS, averaged across three biological replicates. Shading indicates the standard error of the mean (SEM). Assessment of statistical significance was performed using one-sample t-test. **(C)** A time-dependent decrease in H3ac in BV2 cells exposed to <0.1% $O_2$ hypoxia was verified by western blotting. HIF-1α and β-actin were used as hypoxia and loading control, respectively. **(D)** Expression analysis of selected genes (*Glut1, Lgals3, Tmem119* and *P2ry12*) validated by qPCR in BV2 exposed to 21%, <0.1% $O_2$ or <0.1% $O_2$ combined with 10nM Panobinostat for 16 hours. Gene expression was normalised to the *Rn18s* housekeeping gene. Data are presented as a mean fold change ± SD from at least three independent biological replicates. Statistical significance was assessed using an unpaired t-test. Experiment and analysis were performed by Gabriela Smyk. **(E)** Western blot analysis of LGALS3 and H3K27ac in BV2 cells treated as in (D). HIF-1α and β-actin were used as hypoxia and loading control, respectively. **(F)** Densitometric analysis of LGALS3 relative to β-actin shown as mean ± SD from at least three independent experiments. Student's t test was used to determine statistical significance.

To assess the genome-wide impact of Panobinostat on myeloid cells in hypoxic condition, the RNA-seq analysis was performed in BV2 and BMDM cells (**Figure 4.26A-B**). Analysis of GAM-associated marker genes (from **Figure 4.15** and **Figure 4.16**), revealed that some of the hypoxia-regulated microglial markers, e.g. *Tmem119,* and lipid cluster genes, e.g. *Lgals3*, *F10, Apoe,* exhibited clearly reversed expression pattern following Panobinostat treatment in hypoxia (**Figure 4.26C-D**). This effect was more pronounced in BV2 cells than in BMDMs (**Figure 4.26C**). However, closer examination of genes involved in key lipid metabolic pathways showed that Panobinostat also reduced the expression of other lipid storage-associated genes, such as *Plin3* and *Soat2*, in both BV2 and BMDM cells (**Figure 4.26E-F**).

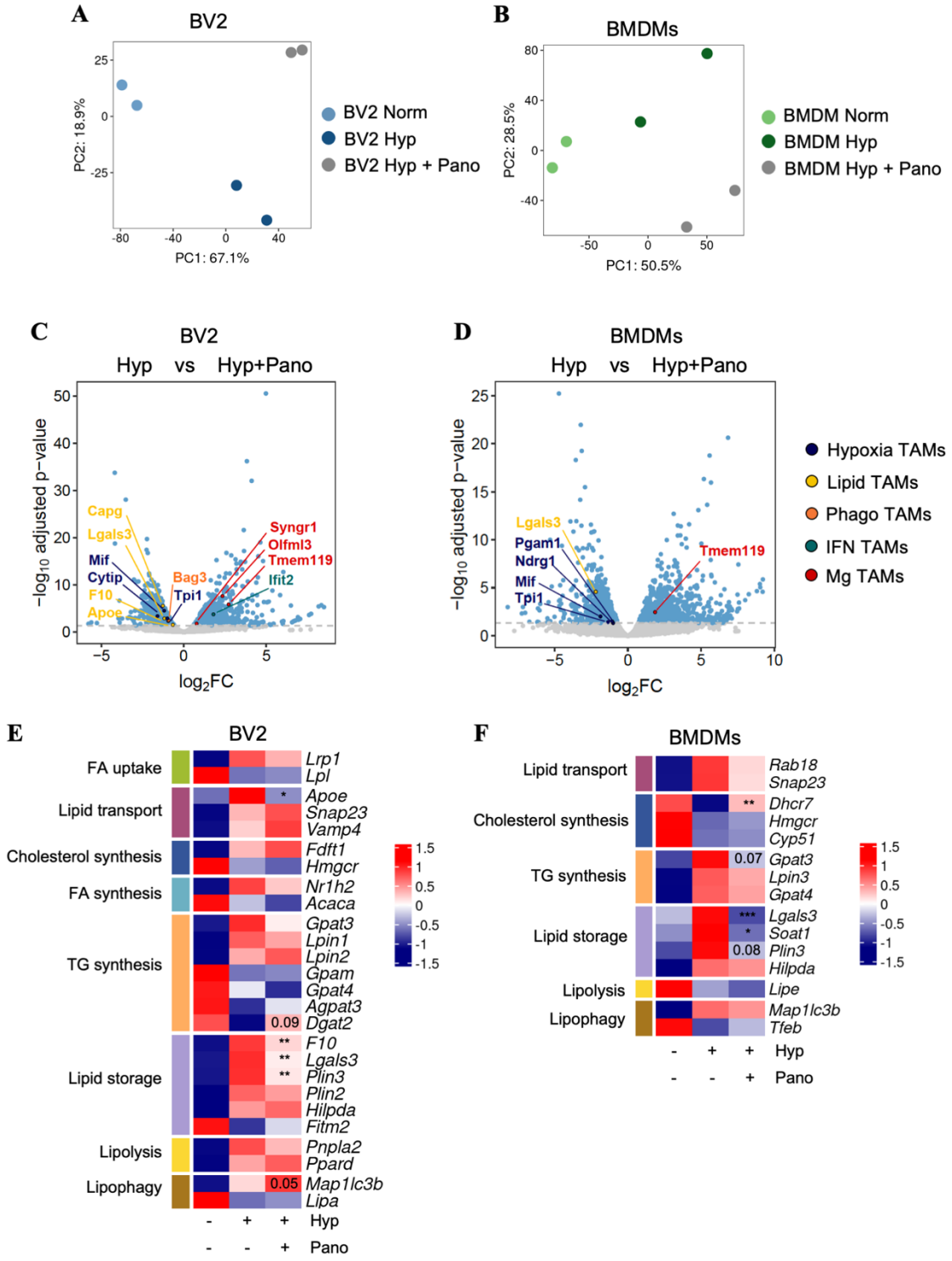


**Figure 4.26. Transcriptomic and lipid changes in GAMs after panobinostat treatment. (A-B)** PCA of normalised gene expression in BV2 **(A)** cells and BMDM **(B)** cells cultured under normoxia, hypoxia (<0.1% O2), or hypoxia with panobinostat (10 nM) treatment for 16 hours. **(C-D)** A volcano plot showing differentially expressed genes (adj. p-value <0.05) in BV2 **(C)** and BMDMs **(D)** cells treated with Panobinostat under hypoxic conditions, compared to hypoxia alone. Genes from Figure 4.15 and Figure 4.16 altered by hypoxia and reversed by Panobinostat are highlighted in colours according to phenotypes. **(E-F)** Heatmap showing z-score expression of lipid metabolism-related genes that were significantly altered after hypoxia compared to normoxia in (E) BV2 and (F) BMDM cells. Genes additionally affected by Panobinostat treatment have the p-adj. values indicate don the heatmap. FA – fatty acid; TG – Triacylglycerol.

To assess whether these transcriptional changes were functionally relevant, lipid droplet formation was assessed using BODIPY, a lipid-biding fluorescent dye. As expected, hypoxia significancy increased the levels of lipid droplets, as reflected by the increased number, total volume, and overall fluorescence intensity per cell in both BV2 (**Figure 4.27A** and **Figure 4.27C**) and BMDM cells (**Figure 4.27B** and **Figure 4.27D**). Notably, Panobinostat treatment reduced the hypoxia-induced lipid droplet levels, which was statistically significant in BV2 cells (**Figure 4.27C**), and showed a similar trend in BMDMs, although not statistically significant in the latter one (**Figure 4.27D**). These results further support functional link between epigenetic regulation and lipid metabolism under hypoxic stress. Specifically, modulation of acetylation alters the expression of lipid-associated genes such as *Lgals3*, which in turn may have immunosuppressive consequences linked with the role of lipid metabolism, as suggested by other studies [109].

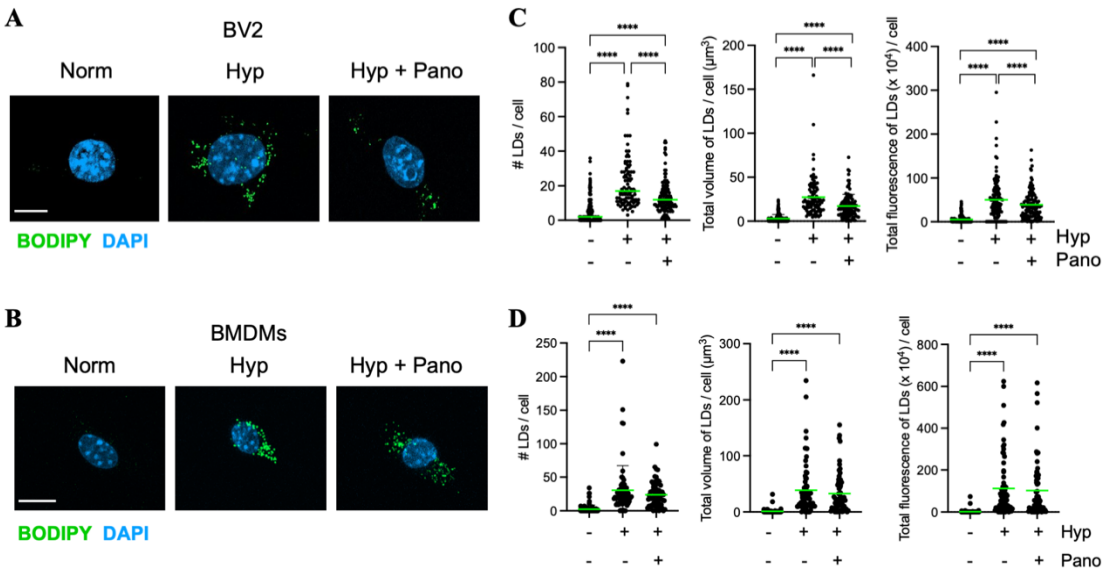


**Figure 4.27. Intracellular changes in lipid droplet accumulation after hypoxia and Panobinostat treatment in BV2 and BMDM cells. (A-B)** BV2 **(A)** or BMDMs **(B)** were seeded on coverslips and, after 24 h, exposed to normoxia, hypoxia or hypoxia combined with 10 nM panobinostat for 16 hours. Lipid droplets and cell nuclei were stained using BODIPY 493/503 (green) DAPI (blue), respectively, and imaged by confocal microscopy, as shown in the representative images. Scale bar, 10 µm. **(C-D)** Quantification of lipid droplet number per cell, total lipid droplets volume per cell, and total lipid droplet fluorescence per cell (calculated as sum of volume × mean intensity for all detected droplets) was performed using Imaris software in BV2 **(C)** and BMDM **(D)** cell treated as in (A-B). For each condition, five Z-stack images were collected from three independent experiments. Data are shown as mean ± SD from all cell measurements. Statistical significance was assessed using an unpaired t-test.

### 4.8. Validation of hypoxia-responsive myeloid markers in human GBM

Finally, to validate the observed findings in human clinical samples, multiplex immunostaining using co-detection by indexing (CODEX) system was performed on a tissue microarray (TMA) from patients' samples. The TMA included 80 cores, comprising 70 glioblastoma and 10 normal brain (cerebrum) samples (**Figure 4.28A**). Markers for hypoxia (GLUT-1), endothelial cells/blood vessels (CD31), immune cells (CD45) and microglia/macrophages/monocytes (CD68) were used alongside TMEM119, LGALS3 and GPNMB identified here as affected by hypoxia *in vitro*. Out of 70 GBM cores, hypoxic areas (defined as GLUT-1 positive cells) were identified in 43 samples (**Figure 4.28B**). These regions were further analysed for TMEM119, LGALS3 and GPNMB. Consistent with *in vitro* data, TMEM119 protein was found to be markedly downregulated in GAMs located in hypoxic regions of GBM cores. This reduction was observed in 39 out of 43 hypoxic cores, while its expression remained high in normoxic regions of the same samples (**Figure 4.28C-D**). LGALS3 protein levels were generally upregulated in hypoxic areas (29 out of 43 hypoxic cores); however, this upregulation was not restricted to myeloid cells (**Figure 4.28C-D**). This supports the hypothesis that LGALS3 is a hypoxia-inducible gene and its expression may also be high in other cell types, including cancer cells [159,160]. Additionally, GPNMB protein was found to be strongly upregulated specifically in GAMs within hypoxic regions in 32 out of the 43 hypoxic cores (**Figure 4.28C-D**). This spatial validation supports the relevance of the *in vitro* findings from glioma-myeloid cells co-culture model and highlights the impact of the hypoxic microenvironment on shaping the identity and functions of GAMs *in vivo*.

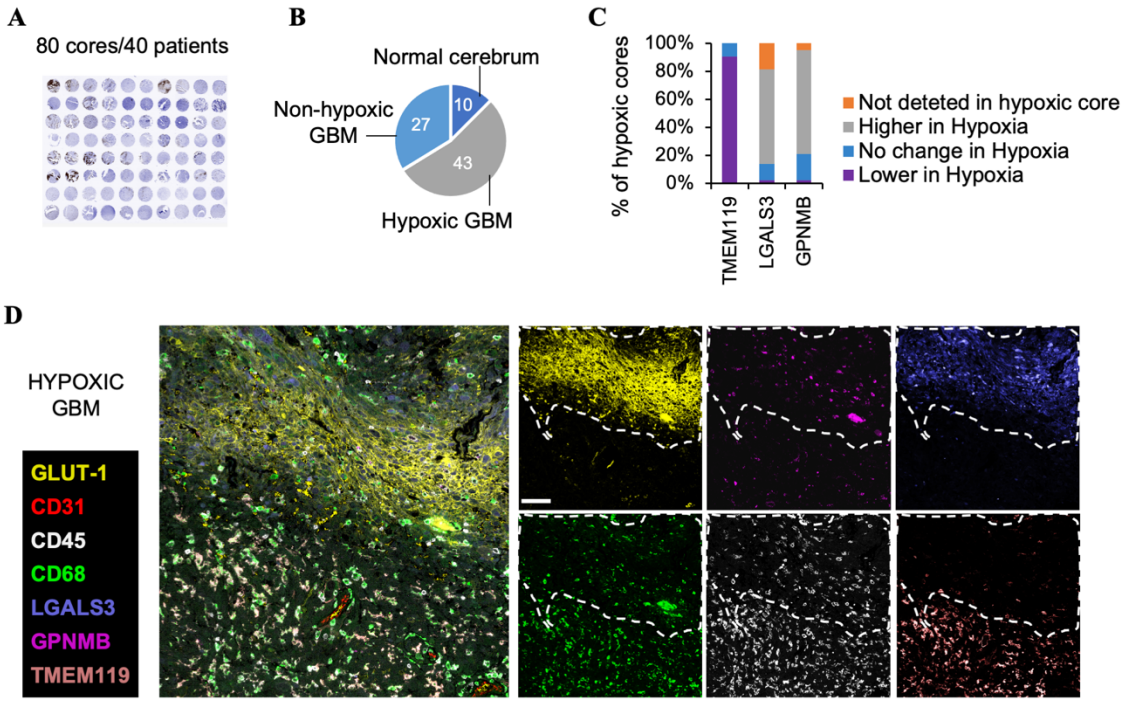


**Figure 4.28. Validation of hypoxia-affected myeloid markers in patient's samples with GBM using CODEX. (A)** A tissue microarray (TMA) consisting of glioblastoma and normal cerebrum samples was used for multiplexed immunofluorescence (IF) using the CODEX system. The TMA slide included 80 cores derived from 40 patients. **(B)** Pie chart showing the quantification of tissue cores on the TMA slide with hypoxic areas, defined by GLUT-1 staining. **(C)** Percentage of hypoxic areas in glioblastoma cores showing higher, lower, unchanged, or undetectable levels of specific protein markers. **(D)** Representative multiplexed CODEX immunofluorescence image of a TMA core, showing hypoxic cells (GLUT-1), endothelial cells/blood vessels (CD31), all immune cells (CD45), glioma-associated microglia/macrophages (GAMs) and monocytes (CD68), along with staining for LGALS3, GPNMB and TMEM119. Colours in the images correspond to those indicated in the legend. Scale bar 100 µm.

# 5. Discussion

Glioblastoma is highly aggressive brain tumour characterised by the extensive hypoxic regions, a feature strongly associated with adverse therapeutic outcomes. This physiological stress contributes to tumour progression by inducing genomic instability, promoting invasion, suppressing anti-tumour immunity, and driving therapy resistance [10]. One major response to hypoxia is the epigenetic reprogramming, which alters chromatin accessibility and reshapes transcriptional profiles, thereby activating or silencing specific gene networks [8,59,77,140,161]. Advances in whole-genome transcriptomics, epigenomics, and integrative computational approaches have greatly improved the resolution at which glioblastoma biology is currently understood. These technologies allowed the dissection of tumour heterogeneity at the cellular level and uncovered dynamic interactions within the TME. Notably, huge advances have been made in the characterisation of the immune compartment, including GAMs. The functional diversity of GAMs, and particularly the immunosuppressive phenotype of GAMs, is increasingly recognised as a key driver of glioma progression [85–87,101–103]. In addition, GAMs were identified in all regions within glioblastoma, including hypoxic areas, which can further reinforce their tumour-promoting functions [107]. In the present doctoral thesis, the impact of hypoxia on the epigenetic and transcriptomic profiles within the glioma TME has been examined. Firstly, it has been shown that hypoxic stress decreases chromatin accessibility in glioma cells, particularly at the gene promoters, with functional consequences for pathways such as RNA splicing and the R-loop interactome. Secondly, by focusing on GAMs, it has been demonstrated that hypoxia alters expression of some of the key identity markers of GAMs as well as functional genes related to lipid metabolism, phagocytosis, chemotaxis, ribosomal biogenesis or interferon-related response. Some of the hypoxia-induced changes in GAMs are fine-tuned through the chromatin remodelling and can be reversed through epigenetic targeting with drugs, i.e. HDAC inhibitors. Collectively, these findings underscore the hypoxic stress as a critical regulator of glioma and myeloid cell function within the glioma TME.

## 5.1. Hypoxia dysregulates chromatin accessibility in GL261 cells

The presented results demonstrated that in GL261 glioma cells, hypoxia significantly affects the histone methylation and acetylation marks (**Figure 4.1B-C**). These results are consistent with the previous observations in other cancer cell lines

exposed to hypoxia [70,71,75,161]. Notably, changes in histone marks were dependent on the severity of hypoxia (**Figure 4.1B**). In addition, these modifications were rapidly reversed upon restoration to normal oxygen levels, underscoring the remarkable plasticity of chromatin structure in response to fluctuating oxygen availability (**Figure 4.1C**). This is particularly relevant in the TME, where unstable oxygen levels and cycles of hypoxia and reoxygenation occur frequently due to transient changes in blood vessel perfusion [11]. Such hypoxia-induced epigenetic remodelling can magnify transcriptional dysregulation, allowing for the persistence of highly adaptive and aggressive tumour cells.

Since hypoxia affects histone PTMs that are associated with the euchromatic (open) and heterochromatic (closed) state, the ATAC-seq was used to genome-wide determine the accessible and closed chromatin regions. The results revealed widespread oxygen-dependent remodelling of chromatin accessibility in GL261 cells under hypoxic conditions and the greatest changes were observed under condition of severe hypoxia (<0.1%) (**Figure 4.2C-D**). In addition, analysis of promoter regions, which correlate with gene expression regulation, revealed a global loss in chromatin accessibility at these genomic sites under hypoxic conditions (**Figure 4.3A-C**). During the time while this research was conducted, other studies were published that characterised the alterations in chromatin accessibility under hypoxic conditions in diverse pathophysiological settings, including response to high-altitudes, tissue hypoxia in cardiomyocytes or in some other cancer cell types [59,140,162–164]. These data showed that hypoxia may lead to either chromatin condensation and reduced accessibility or to enhanced chromatin openness. For instance, Batie et al. reported that in HeLa cells exposed hypoxia, a greater proportion of chromatin changes corresponds to increased rather than decreased chromatin accessibility (474 increased and 162 decreased ATAC-seq peaks) [140]. At the same oxygen tension (1% $O_2$) as in Batie et al., our data also revealed both increases and decreases in chromatin accessibility. In fact, our data identified a larger number of altered regions (3,091 increased and 2,829 decreased ATAC peaks) using the same threshold parameters for defining the differential accessibility. This discrepancy in the number of identified peaks may be, at least in part, due to differences in the sample processing. In our study, after hypoxia exposure cells were immediately fixed prior to ATAC-seq processing, to avoid any technical artefacts resulting from the oxygen influence on the chromatin wile processing alive cells. As previously described, any reoxygenation of the sample during handling can alter chromatin accessibility and may therefore fail to accurately capture the full chromatin changes induced by hypoxia. Interestingly, Batie et al. reported that most

of the inducible changes were largely dependent on the presence of HIF TFs. Considering the oxygen concentration used (1% $O_2$), this outcome was not unexpected, since under moderate hypoxia, HIF TFs play a major regulatory role [10]. In another ATAC-seq analysis, Miar et al. found that in breast cancer cells 0.1% hypoxia leads to decreased accessibility at 3,138 genomic loci and increased accessibility at 2,439 loci. They have shown that severely low oxygen level suppress the type I interferon pathway through the reduced chromatin accessibility in promoter regions of genes that have binding motifs for two crucial TFs such as STAT1 or IRF3 [59]. In our study, in addition to interferon-related genes, additional pathways were identified as downregulated via changes in chromatin accessibility at promoter regions under hypoxic conditions. These included RNA processing and splicing, and the R-loop interactome (**Figure 4.4A-C**). Recently, some studies reported an increased levels of R-loops under hypoxia [38,76]. This accumulation was linked with the transcriptional and replication stress, triggering downstream activation of additional stress-response signalling pathways. Among the genes involved in R-loop formation and resolution, *DDX5* helicase has been identified as significantly decreased under hypoxia. Notably, in this work it has been shown that decreased expression of *DDX5* under hypoxia is correlated with the loss of H3K27ac and a decrease in chromatin accessibility at the promoter region of this gene (**Figure 4.6A-F**). These findings underscore the critical role of hypoxia-induced epigenetic alterations, which by reshaping the chromatin structure and accessibility, reprogram the gene expression pattern, thereby influencing the key cellular processes such as adaptation to stress, survival, and the acquisition of more aggressive phenotypes in cancer.

## 5.2. Could hypoxia diminish the differences between the identity of macrophages and microglia in GBM?

Recent single-cell transcriptomic studies have largely focused on the detailed definition of distinct GAM populations, providing important insights into their heterogeneity and functional role within GBM [101–103]. Also, distinct markers have been used to clearly distinguish the populations of microglia, monocytes and macrophages present within the GBM. However, data analyses that begin with complex clustering may diminish the significance of certain dependencies induced by hypoxic stress, reducing them to a simplified, predefined hypoxia signature. In addition, the methods used for tissue and sample processing play a critical role, as they may lead to re-oxygenation, loss of hypoxic cell fractions, and consequently, misinterpretation of the data. Furthermore,

technical aspects of sample processing for single-cell transcriptomics may remove discrete hypoxia-exposed cells due to a general removal of dying cells, which again may affect the genuine picture of all hypoxia-exposed cells within the TME of GBM [86]. In our study, a direct co-culture model of myeloid cells with glioma cells was optimised in order to closely mimic the conditions present *in vivo*. In addition, the fixation of the material allowed for the preservation of oxygen-dependent alterations. This approach made it possible to distinguish changes in GAMs that were driven specifically by hypoxic stress from those that are induced by the combined effects of hypoxia and a contact with the glioma cells.

The initial analysis focused on individual genes already assumed as canonical markers of origin of distinct GAM subtypes [101,103,165]. Our analysis showed a clear impact of hypoxia on these genes, including a significant decrease in expression of typical microglia markers such as *P2ry12* and *Tmem119* (**Figure 4.8A-B**). In contrast, *Lgals3*, which in some cases was used to distinguish monocyte/macrophages from microglia [101,103], was increased under hypoxia in both microglia and macrophages cell lines (**Figure 4.7A-F**). As demonstrated in other glioma studies, galectin-3 (encoded by *Lgals3*) expressed in GAMs stimulates tumour cell migration and invasion, promotes an anti-inflammatory phenotype and drives immunosuppression [148]. In addition, studies in breast cancer cells showed that hypoxia induces galectin-3 expression and secretion by tumour-associated macrophages (TAMs), contributing to tumour growth and metastasis [166]. In both contexts, inhibition of galectin-3 shifted myeloid cell activity towards a more tumour-repressive function. Furthermore, other investigations have shown that *Lgals3* is upregulated in tumour cells, including glioma or mammary carcinoma cell lines, under hypoxia, suggesting that it is a genuine hypoxia-inducible gene, irrespective of a cell type [159,160]. Indeed, our study showed that in human GBM patient's samples, galectin-3 levels were upregulated in hypoxic areas and this upregulation was not constricted to myeloid cells (**Figure 4.28C-D**). Therefore, upregulation of galectin-3 in all GAMs under hypoxic conditions and generally in all cells present in hypoxic areas, including tumours cells, may have a cumulative effect on promoting the progression of cancer. These findings suggest that therapeutic targeting of galectin-3 in the context of hypoxia may hold promise, although further investigations are needed to validate this approach.

Our analysis of single maker genes led to a deeper examination of genes characterizing the phenotypic properties of GAMs. The most prominent shift was in the upregulation of genes associated with lipid metabolism and phagocytic activity. In

contrast, genes linked to interferon signalling were predominantly downregulated, emphasizing the role of hypoxia in suppressing immune responses. Importantly, these changes were present in both microglia cells as well as in macrophages, indicating that the effect is not restricted to a single macrophage sub-type (**Figure 4.15C** and **Figure 4.16D**). Furthermore, these hypoxia-dependent gene expression changes have direct functional consequences. It has been shown that hypoxia increase phagocytic capacity (**Figure 4.16E-F**) as well as lipid accumulation in myeloid cells, which was supported by an increased expression of lipid-storage related genes (**Figure 4.17A-B**).

These findings emphasise the strong impact of hypoxia on transcriptional regulation and on shaping the functional phenotypes in myeloid cell. Previous studies, especially in mouse models, have shown that Mg-GAMs mainly reside at the tumour periphery, whereas Mo/Mφ-GAMs are enriched within the tumour core [101,103,105]. Our results show that hypoxic microenvironment can profoundly influence the expression of markers distinguishing the identity of microglia and macrophages and may complicate the accurate characterisation of these populations present in hypoxic areas. Accounting for hypoxia-dependent effects can provide important insights into GAMs biology and refined characterisation of phenotypes identified in single-cell datasets.

### 5.3. Hypoxia fine-tunes the chromatin changes in GAMs

As shown in this work and by others, reduced oxygen availability significantly remodels chromatin properties, and drives widespread transcriptomic changes in cancer cells [59,140,162–164]. However, hypoxia dependent chromatin reprogramming in myeloid cells has not been well investigated to date. To address this, chromatin accessibility was examined using the same direct co-culture model applied for transcriptomic analysis. Initially, global chromatin changes in microglia cells were assessed, revealing that hypoxia alone predominantly reduced promoter accessibility, which was consistent with findings in glioma cells. In contrast, in the presence of tumour cells under hypoxia, a greater number of regions were altered, with larger number of promoters becoming more accessible (**Figure 4.20A**). These results suggest that hypoxia primarily decreases promoter accessibility, while additional presence of glioma cells shifts the response in hypoxia towards the increased promoter openness. This highlights the importance of the co-culture model system used in this study, as it enables the identification of distinct changes driven solely by hypoxia and those resulting from tumour-immune interactions under hypoxic conditions.

A more detailed analysis of genes used to characterise particular GAM populations further demonstrated that hypoxia-depended chromatin reprogramming may function as a master regulator of key transcriptional programs essential for myeloid cell identity (**Figure 4.24A**). For example, a reduced expression of typical microglia marker gene *P2ry12* under hypoxia was accompanied by a marked decrease in chromatin accessibility at its promoter region (**Figure 4.24E**). Notably, this region was enriched in a biding site for the TFs such as IRF8 and SPI1, which are known as central regulators of microglial cell identity. These TFs often bind together to regulatory elements of DNA, forming transcriptional network to regulate microglial-specific gene programs [167,168]. Recent studies reported that IRF8 biding to enhancer region in postnatal microglia is necessary to establish microglia-specific chromatin accessibility sites and DNA methylation patterns, crucial for their homeostatic functions [169]. Data presented here suggests that disruptions of this transcriptional regulation in hypoxia, via changes in SPI1/IRF8 motif accessibility, may affect the identity of microglia, impairing its regulatory capabilities and potentially transforming these cells into a tumour-promoting phenotype. Importantly, the chromatin changes at the *P2ry12* promoter were observed only in microglia co-cultured with glioma cells, and not under hypoxia alone (**Figure 4.24E**). This indicates that *P2ry12* regulation requires additional cues beyond oxygen deprivation, such as direct interaction with glioma cells, to disrupt a chromatin accessibility. Further investigation is necessary to better understand how this co-regulation occurs in GAMs.

Although hypoxia induces widespread shifts in chromatin accessibility in microglia cells, these changes do not always align with the changes observed in the gene expression (**Figure 4.23A-B**). In many cases, gene expression is triggered in hypoxia irrespective of increases in chromatin accessibility. Moreover, not all chromatin accessibility changes are reflected by particular gene expression. Several possible mechanisms may explain these discrepancies. Importantly, reduced oxygen levels rapidly activate the members of HIF family of TFs through the loss of the activity of PHDs, that lead to their degradation. Moreover, other stress-responsive TFs are being active, including NF-κB or ATFs. These TFs initiate adaptive transcriptional programs almost immediately, whereas the chromatin accessibility-dependent changes generally require more time to affect the gene expression [8,170]. In addition, even when certain promoter or enhancer regions become accessible under hypoxia, the additional signals are needed to trigger transcriptional activation. Since hypoxia broadly increases histone methylation,

mainly due to the inactivation of oxygen-dependent histone demethylases, this can promote chromatin bivalency [4,8]. In such case, repressive mark H3K27me3 could coexist with the activating mark H3K4me3 at the same loci, making chromatin accessible but transcriptionally inactive until conditions shift - similarly to the well-described bivalency observed in embryonic stem cells [171]. This mechanism may illustrate how dynamic shifts in histone methylation could induce the plasticity within the evolving TME. Another possibility is that a certain genomic locus may become accessible but occupied by repressive TFs, leading to a decreased gene expression. Furthermore, many hypoxia-induced chromatin alterations may occur at enhancer regions, located far from promoters, with changes in gene expression often mediated through 3D contacts in the chromatin structure [172]. Very recent work has revealed that under hypoxic stress, the zinc fingers and homeoboxes 2 (ZHX2) TF, which is regulated in a similar way as HIFα, through the pVHL E3 ubiquitin ligase, undergoes a phase separation to form dynamic condensates in the nucleus. These condensates recruit a key chromatin organiser CCCTC-binding factor (CTCF) to reshape the chromatin looping, and activate the oncogenic transcription programs driving metastasis in breast cancer cells [173]. Such findings emphasise the profound influence of oxygen availability on genome-wide chromatin architecture and transcriptional regulation. Therefore, future epigenomic studies, particularly those focused on bivalent promoters, enhancer location, and 3D chromatin organisation, will be essential for unravelling the multi-layered mechanisms by which hypoxia reprograms the gene expression in GAMs and contributes to the tumour progression.

### 5.4. Hypoxia induces lipid droplet accumulation in GAMs via increase of specific genes

Lipid metabolism has emerged as a critical regulator of cellular function within the TME [174]. It is well established that hypoxia profoundly alters lipid metabolism in cancer cells. For example, by promoting triglyceride (TG) and lipid accumulation in the form of lipid droplets, through the upregulation of genes such as *Lpin2*, *Plin2 , Fabp3/7* [24,175,176]. This accumulation supports the tumour cell growth and contributes to a more aggressive phenotype. In parallel, recent studies have shown that TAMs also accumulate lipids and display a strong pro-tumorigenic phenotype [177–179]. While the relationship between hypoxia and lipid metabolism has been extensively explored in cancer cells, it remains less understood in TAMs [7,24,175,176]. Recent single-cell multi-omic study by Kloosterman et al. identified a distinct population of so-called “lipid-laden macrophages”

(LLMs) present in gliomas, which are thought to reside in hypoxic niches [109]. These cells promote tumour progression by engulfing lipid-rich myelin debris and transferring these lipids to glioma cells via transporters such as ABCA1 and ABCG1, thereby directly fuelling glioma growth. Our results complement these findings, showing that hypoxia directly affect the numerous lipid-related genes in both microglia and macrophages (**Figure 4.17A-B**). Notably, genes associated to lipid storage, including *Plin2/3, Lgals3* or *Gpnmb*, were markedly upregulated under hypoxic conditions. Further functional analysis confirmed that hypoxia significantly increased the lipid droplet levels in microglia and macrophages that have not been even exposed to glioma cells (**Figure 4.27A-D**). In addition, in hypoxic microglia and macrophages, many lipid transport-associated genes were upregulated including *Rab18, Vamp4/7* or *Snap23* which may play a role in the inter-organelle lipid trafficking [180,181]. Similarly, lipid export genes such as *Abca1* and *Abcg1* were also elevated under hypoxia in both cell lines. These findings may suggest that hypoxic GAMs dynamically redistribute the lipids between the organelles such as ER, mitochondria or lipid droplets, while also exporting lipids extracellularly, a pattern consistent with the LLM study [109]. Moreover, genes involved in lipid degradation pathways were also mainly increased in hypoxia, which could potentially lead to the production of lipid-derived signalling molecules [182]. Nevertheless, further studies will be necessary to clarify whether and how this contributes to the tumour-promoting phenotype of GAMs. On the contrary, the expression of genes involved in extracellular lipid uptake was unchanged or even reduced, despite increased lipid accumulation. Several key lipogenic regulators, such as *Nr1h2* and *Srebf1*, as well as genes involved in triglyceride synthesis *Lpin1/2/3*, were upregulated in hypoxia, which may underlie the observed phenotype. This could reflect an adaptive response, in which cells already overloaded with lipids, limit the further uptake to protect against the lipotoxicity. Notably, in many of these lipid metabolism-related genes, changes in the chromatin accessibility were concordant with the transcriptional response (**Figure 4.24B**). Taken together, these findings underscore the importance of hypoxic stress and chromatin regulation in shaping the lipid metabolic reprogramming of myeloid cells.

### 5.5. Can hypoxia-induced phenotypes be pharmacologically modified?

Presented data demonstrated that chromatin regulation under hypoxia not only affects the myeloid cell identity (**Figure 4.24A-F**), but also has a direct functional consequence, such as in lipid droplet accumulation (**Figure 4.27A-D**). This raised the

question of whether such changes could be modified by epigenetics drugs. Since histone acetylation is markedly reduced in hypoxic myeloid cells (**Figure 4.25A-C**), it was tested whether the treatment with HDAC inhibitor, panobinostat, could not only restore the acetylation but also affect the lipid droplet accumulation. As expected, the panobinostat treatment restored the histone acetylation in hypoxia (**Figure 4.25E**). Furthermore, it led to the reduction in the expression of several genes involved in lipid metabolism and storage, including *Lgals3*, *Plin3*, and *F10* (**Figure 4.26C-F**), and was accompanied by a decreased lipid accumulation in microglia cells (**Figure 4.27A-D**). Since histone acetylation is generally linked to the transcriptional activation, it may seem counterintuitive to note that a global increase in this mark coincided with reduced gene expression. Nevertheless, recent study explaining the regulation of *Lgals3* demonstrated that silencing HDAC7 elevates H3K27ac at the promoter of transcription factor SOX8, leading to its upregulation. Subsequently, SOX8 interacts with the JUN TF and suppresses its transcriptional activity, thereby reducing *Lgals3* expression [183]. In our data, the expression of SOX8 was not changed in hypoxia. However, the promoter region of *Lgals3* was enriched in motif recognised by JUN (**Figure 4.24C**). It is possible that other proteins with similar binding properties and function as SOX8 could mediate these effects. However, such hypothesis requires further research. In addition, the regulation described above was identified in glioma stem cells and may not apply to macrophages. Moreover, the use of panobinostat treatment may not be optimal to explain our hypothesis, as this pan-HDAC inhibitor induces widespread genome-wide changes in histone acetylation, which may result in additional indirect interfering with the SOX8 expression. As a non-selective HDAC inhibitor, it simultaneously blocks multiple HDACs, which broadens the cellular consequences of such treatment [184]. Other more specific drugs should therefore be investigated or direct genetic manipulation with the HDAC7/SOX8 axis. Nevertheless, the results presented here strongly suggest that pharmacological targeting of the chromatin properties may lead to the remodelling of the function of myeloid cells present in the TME of gliomas and could be an interesting approach in boosting response to other treatments, for example, immunotherapy.

# 6. Summary and conclusion

The results presented in this PhD thesis unravel new links between hypoxia, chromatin and gene regulatory networks within TME of glioma, particularly in myeloid cells. Through a series of *in vitro* experiments, bioinformatics analyses, as supportive data from patient's samples, the following conclusions were drawn:

1. Hypoxia increases the chromatin compaction, predominantly at gene promoters of glioma cells and specific pathways are impacted including RNA splicing and the R-loop interactome.
2. Hypoxia alters expression of key identity markers of GAMs, including upregulation of *Lgals3* and downregulation of *P2ry12*, *Tmem119*.
3. Many functional pathways related to lipid metabolism, phagocytosis, chemotaxis, ribosomal biogenesis or interferon-related response in microglia and macrophages are also significantly affected in response to hypoxic-stress.
4. Hypoxia-dependent changes in chromatin accessibility in microglia cells partially contribute to the changes in gene expression profiles and affect expression of some GAM-related genes.
5. Hypoxia induces lipid droplet accumulation in myeloid cells via induced expression of specific lipid-related genes and loss of global histone acetylation.
6. Targeting HDACs restores histone acetylation and reduces lipid accumulation in hypoxic microglia cells.
7. Major changes in gene expression observed in response to hypoxia in glioma-GAM co-culture model are reflected in patient's samples *in vivo.*

These findings are highly significant, as they expand the current understanding of how hypoxia shapes the glioma microenvironment. In particular, they underscore the crucial role of hypoxia-induced epigenetic alterations, whose modulation could enable the reprogramming of myeloid cells toward a more anti-tumour phenotype.

# 7. Research articles resulting from this PhD work

**Dzwigonska, M**., Rosa, P., Lipiec, S., Obrebski, T., Smyk, G., Kaza, B., Cyranowski, S., Ellert-Miklaszewska, A., Kominek, A., Malik, A. R., Piwocka, K., Mieczkowski, J., Kaminska, B., & Leszczynska, K. B. (2025). Hypoxic stress dysregulates functions of glioma-associated myeloid cells through epigenomic and transcriptional programs. **Cell Reports**, 44(9), 116222. https://doi.org/10.1016/j.celrep.2025.116222

Leszczynska, K. B., Freitas-Huhtamäki, A., Jayaprakash, C., **Dzwigonska, M**., Vitorino, F. N. L., Horth, C., Wojnicki, K., Gielniewski, B., Szadkowska, P., Kaza, B., Nazarian, J., Ciolkowski, M. K., Trubicka, J., Grajkowska, W., Garcia, B. A., Majewski, J., Kaminska, B., & Mieczkowski, J. (2024). H2A.Z histone variants facilitate HDACi-dependent removal of H3.3K27M mutant protein in pediatric high-grade glioma cells. **Cell Reports**, 43(2), 113707. https://doi.org/10.1016/j.celrep.2024.113707

Leszczynska, K. B., **Dzwigonska, M**., Estephan, H., Moehlenbrink, J., Bowler, E., Giaccia, A. J., Mieczkowski, J., Kaminska, B., & Hammond, E. M. (2023). Hypoxia-mediated regulation of DDX5 through decreased chromatin accessibility and post-translational targeting restricts R-loop accumulation. **Molecular Oncology**, 17(7), 1173–1191. https://doi.org/10.1002/1878-0261.13431

# 8. Bibliography


1. Hammond, E.M., Asselin, M.C., Forster, D., O'Connor, J.P.B., Senra, J.M., and Williams, K.J. (2014). The Meaning, Measurement and Modification of Hypoxia in the Laboratory and the Clinic. Clin. Oncol. *26*, 277–288. https://doi.org/10.1016/j.clon.2014.02.002.
2. Thiruthaneeswaran, N., Bibby, B.A.S., Yang, L., Hoskin, P.J., Bristow, R.G., Choudhury, A., and West, C. (2021). Lost in application: Measuring hypoxia for radiotherapy optimisation. Eur. J. Cancer *148*, 260–276. https://doi.org/10.1016/j.ejca.2021.01.039.
3. Lee, K.H., Kim, D.Y., and Kim, W. (2021). Cultivation of human skin cells under physiological oxygen concentration modulates expression of skin significant genes and response to hydroxy acids. Biochem. Biophys. Res. Commun. *551*, 161–167. https://doi.org/10.1016/j.bbrc.2021.02.113.
4. Kim, J., Lee, H., Yi, S.-J., and Kim, K. (2022). Gene regulation by histone-modifying enzymes under hypoxic conditions: a focus on histone methylation and acetylation. Exp. Mol. Med. *54*, 878–889. https://doi.org/10.1038/s12276-022-00812-1.
5. Della Rocca, Y., Fonticoli, L., Rajan, T.S., Trubiani, O., Caputi, S., Diomede, F., Pizzicannella, J., and Marconi, G.D. (2022). Hypoxia: molecular pathophysiological mechanisms in human diseases. J. Physiol. Biochem. *78*, 739–752. https://doi.org/10.1007/s13105-022-00912-6.
6. Brown, J.M., and Giaccia, A.J. (1998). The unique physiology of solid tumors: Opportunities (and problems) for cancer therapy. Cancer Res. *58*, 1408–1416.
7. Lee, P., Chandel, N.S., and Simon, M.C. (2020). Cellular adaptation to hypoxia through hypoxia inducible factors and beyond. Nat. Rev. Mol. Cell Biol. *21*, 268–283. https://doi.org/10.1038/s41580-020-0227-y.
8. Lee, S.C.E.S., Pyo, A.H.A., and Koritzinsky, M. (2023). Longitudinal dynamics of the tumor hypoxia response: From enzyme activity to biological phenotype. Sci. Adv. *9*. https://doi.org/10.1126/sciadv.adj6409.
9. GRAY, L.H., CONGER, A.D., EBERT, M., HORNSEY, S., and SCOTT, O.C. (1953). The concentration of oxygen dissolved in tissues at the time of irradiation as a factor in radiotherapy. Br. J. Radiol. *26*, 638–648. https://doi.org/10.1259/0007-1285-26-312-638.

10. Suvac, A., Ashton, J., and Bristow, R.G. (2025). Tumour hypoxia in driving genomic instability and tumour evolution. Nat. Rev. Cancer *25*, 167–188. https://doi.org/10.1038/s41568-024-00781-9.
11. Michiels, C., Tellier, C., and Feron, O. (2016). Cycling hypoxia: A key feature of the tumor microenvironment. Biochim. Biophys. Acta - Rev. Cancer *1866*, 76–86. https://doi.org/10.1016/j.bbcan.2016.06.004.
12. Koritzinsky, M., and Wouters, B.G. (2013). The Roles of Reactive Oxygen Species and Autophagy in Mediating the Tolerance of Tumor Cells to Cycling Hypoxia. Semin. Radiat. Oncol. *23*, 252–261. https://doi.org/10.1016/j.semradonc.2013.05.006.
13. Bristow, R.G., and Hill, R.P. (2008). Hypoxia and metabolism: Hypoxia, DNA repair and genetic instability. Nat. Rev. Cancer *8*, 180–192. https://doi.org/10.1038/nrc2344.
14. Frost, J., Frost, M., Batie, M., Jiang, H., and Rocha, S. (2021). Roles of hif and 2-oxoglutarate-dependent dioxygenases in controlling gene expression in hypoxia. Cancers (Basel). *13*, 1–31. https://doi.org/10.3390/cancers13020350.
15. Wilson, W.R., and Hay, M.P. (2011). Targeting hypoxia in cancer therapy. https://doi.org/10.1038/nrc3064.
16. Denko, N.C. (2008). Hypoxia, HIF1 and glucose metabolism in the solid tumour. Nat. Rev. Cancer *8*, 705–713. https://doi.org/10.1038/nrc2468.
17. Iyer, N. V., Kotch, L.E., Agani, F., Leung, S.W., Laughner, E., Wenger, R.H., Gassmann, M., Gearhart, J.D., Lawler, A.M., Yu, A.Y., et al. (1998). Cellular and developmental control of O2 homeostasis by hypoxia- inducible factor 1α. Genes Dev. *12*, 149–162. https://doi.org/10.1101/gad.12.2.149.
18. Kim, J.W., Tchernyshyov, I., Semenza, G.L., and Dang, C. V. (2006). HIF-1-mediated expression of pyruvate dehydrogenase kinase: A metabolic switch required for cellular adaptation to hypoxia. Cell Metab. *3*, 177–185. https://doi.org/10.1016/j.cmet.2006.02.002.
19. Fukuda, R., Zhang, H., Kim, J. whan, Shimoda, L., Dang, C. V., and Semenza, G.L.L. (2007). HIF-1 Regulates Cytochrome Oxidase Subunits to Optimize Efficiency of Respiration in Hypoxic Cells. Cell *129*, 111–122. https://doi.org/10.1016/j.cell.2007.01.047.
20. Sun, R.C., and Denko, N.C. (2014). Hypoxic regulation of glutamine metabolism through HIF1 and SIAH2 supports lipid synthesis that is necessary for tumor

growth. Cell Metab. *19*, 285–292. https://doi.org/10.1016/j.cmet.2013.11.022.

21. Roongta, U. V., Pabalan, J.G., Wang, X., Ryseck, R.P., Fargnoli, J., Henley, B.J., Yang, W.P., Zhu, J., Madireddi, M.T., Lawrence, R.M., et al. (2011). Cancer cell dependence on unsaturated fatty acids implicates stearoyl-CoA desaturase as a target for cancer therapy. Mol. Cancer Res. https://doi.org/10.1158/1541-7786.MCR-11-0126.
22. Chabowski, A., Górski, J., Calles-Escandon, J., Tandon, N.N., and Bonen, A. (2006). Hypoxia-induced fatty acid transporter translocation increases fatty acid transport and contributes to lipid accumulation in the heart. FEBS Lett. *580*, 3617–3623. https://doi.org/10.1016/j.febslet.2006.05.045.
23. Mwaikambo, B.R., Yang, C., Chemtob, S., and Hardy, P. (2009). Hypoxia up-regulates CD36 expression and function via hypoxia-inducible factor-1-and phosphatidylinositol 3-kinase-dependent mechanisms. J. Biol. Chem. *284*, 26695–26707. https://doi.org/10.1074/jbc.M109.033480.
24. Bensaad, K., Favaro, E., Lewis, C.A., Peck, B., Lord, S., Collins, J.M., Pinnick, K.E., Wigfield, S., Buffa, F.M., Li, J.L., et al. (2014). Fatty acid uptake and lipid storage induced by HIF-1α contribute to cell growth and survival after hypoxia-reoxygenation. Cell Rep. *9*, 349–365. https://doi.org/10.1016/j.celrep.2014.08.056.
25. Qiu, B., Ackerman, D., Sanchez, D.J., Li, B., Ochocki, J.D., Grazioli, A., Bobrovnikova-Marjon, E., Alan Diehl, J., Keith, B., and Celeste Simon, M. (2016). HIF2α-dependent lipid storage promotes endoplasmic reticulum homeostasis in clear-cell renal cell carcinoma. Cancer Discov. https://doi.org/10.1158/2159-8290.CD-14-1507.
26. Koumenis, C., and Wouters, B.G. (2006). "Translating" tumor hypoxia: Unfolded protein response (UPR)-dependent and UPR-independent pathways. Mol. Cancer Res. *4*, 423–436. https://doi.org/10.1158/1541-7786.MCR-06-0150.
27. Koritzinsky, M., Magagnin, M.G., Van Den Beucken, T., Seigneuric, R., Savelkouls, K., Dostie, J., Pyronnet, S., Kaufman, R.J., Weppler, S.A., Voncken, J.W., et al. (2006). Gene expression during acute and prolonged hypoxia is regulated by distinct mechanisms of translational control. EMBO J. *25*, 1114–1125. https://doi.org/10.1038/sj.emboj.7600998.
28. B'Chir, W., Maurin, A.C., Carraro, V., Averous, J., Jousse, C., Muranishi, Y., Parry, L., Stepien, G., Fafournoux, P., and Bruhat, A. (2013). The eIF2α/ATF4

pathway is essential for stress-induced autophagy gene expression. Nucleic Acids Res. https://doi.org/10.1093/nar/gkt563.

29. Rozpedek, W., Pytel, D., Mucha, B., Leszczynska, H., Diehl, J.A., and Majsterek, I. (2016). The Role of the PERK/eIF2α/ATF4/CHOP Signaling Pathway in Tumor Progression During Endoplasmic Reticulum Stress. Curr. Mol. Med. *16*, 533–544. https://doi.org/10.2174/1566524016666160523143937.

30. van den Beucken, T., Koritzinsky, M., Niessen, H., Dubois, L., Savelkouls, K., Mujcic, H., Jutten, B., Kopacek, J., Pastorekova, S., van der Kogel, A.J., et al. (2009). Hypoxia-induced expression of carbonic anhydrase 9 is dependent on the unfolded protein response. J. Biol. Chem. *284*, 24204–24212. https://doi.org/10.1074/jbc.M109.006510.

31. Olcina, M., Lecane, P.S., and Hammond, E.M. (2010). Targeting hypoxic cells through the DNA damage response. Clin. Cancer Res. *16*, 5624–5629. https://doi.org/10.1158/1078-0432.CCR-10-0286.

32. Foskolou, I.P., Jorgensen, C., Leszczynska, K.B., Olcina, M.M., Tarhonskaya, H., Haisma, B., D'Angiolella, V., Myers, W.K., Domene, C., Flashman, E., et al. (2017). Ribonucleotide Reductase Requires Subunit Switching in Hypoxia to Maintain DNA Replication. Mol. Cell *66*, 206-220.e9. https://doi.org/10.1016/j.molcel.2017.03.005.

33. Pires, I.M., Bencokova, Z., Milani, M., Folkes, L.K., Li, J.A., Stratford, M.R., Harris, A.L., and Hammond, E.M. (2010). Effects of acute versus chronic hypoxia on DNA damage responses and genomic instability. Cancer Res. *70*, 925–935. https://doi.org/10.1158/0008-5472.CAN-09-2715.

34. Bencokova, Z., Kaufmann, M.R., Pires, I.M., Lecane, P.S., Giaccia, A.J., and Hammond, E.M. (2009). ATM Activation and Signaling under Hypoxic Conditions. Mol. Cell. Biol. https://doi.org/10.1128/mcb.01301-08.

35. Hammond, E.M., Denko, N.C., Dorie, M.J., Abraham, R.T., and Giaccia, A.J. (2002). Hypoxia Links ATR and p53 through Replication Arrest. Mol. Cell. Biol. *22*, 1834–1843. https://doi.org/10.1128/mcb.22.6.1834-1843.2002.

36. Brady, C.A., Laura, D., Brady, C.A., and Attardi, L.D. (2010). p53 at a glance p53 at a Glance. *2010*, 2527–2532. https://doi.org/10.1242/jcs.064501.

37. Graeber, T.G., Osmanian, C., Jacks, T., Housman, D.E., Koch, C.J., Lowe, S.W., and Giaccia, A.J. (1996). Hypoxia-mediated selection of cells with diminished apoptotic potential in solid tumours. Nature. https://doi.org/10.1038/379088a0.

38. Ramachandran, S., Ma, T.S., Griffin, J., Ng, N., Foskolou, I.P., Hwang, M.S., Victori, P., Cheng, W.C., Buffa, F.M., Leszczynska, K.B., et al. (2021). Hypoxia-induced SETX links replication stress with the unfolded protein response. Nat. Commun. *12*. https://doi.org/10.1038/s41467-021-24066-z.

39. Santos-Pereira, J.M., and Aguilera, A. (2015). R loops: New modulators of genome dynamics and function. Nat. Rev. Genet. *16*, 583–597. https://doi.org/10.1038/nrg3961.

40. Ng, N., Purshouse, K., Foskolou, I.P., Olcina, M.M., and Hammond, E.M. (2018). Challenges to DNA replication in hypoxic conditions. FEBS J. *285*, 1563–1571. https://doi.org/10.1111/febs.14377.

41. Brooks, J.M., Menezes, A.N., Ibrahim, M., Archer, L., Lal, N., Bagnall, C.J., Von Zeidler, S. V., Valentine, H.R., Spruce, R.J., Batis, N., et al. (2019). Development and validation of a combined hypoxia and immune prognostic classifier for head and neck cancer. Clin. Cancer Res. *25*, 5315–5328. https://doi.org/10.1158/1078-0432.CCR-18-3314.

42. Nordsmark, M., Bentzen, S.M., Rudat, V., Brizel, D., Lartigau, E., Stadler, P., Becker, A., Adam, M., Molls, M., Dunst, J., et al. (2005). Prognostic value of tumor oxygenation in 397 head and neck tumors after primary radiation therapy. An international multi-center study. Radiother. Oncol. *77*, 18–24. https://doi.org/10.1016/j.radonc.2005.06.038.

43. Hall, E.J., and Giaccia, A.J. (2012). Radiobiology for the radiologist: Seventh edition.

44. Singleton, D.C., Macann, A., and Wilson, W.R. (2021). Therapeutic targeting of the hypoxic tumour microenvironment. Nat. Rev. Clin. Oncol. *18*, 751–772. https://doi.org/10.1038/s41571-021-00539-4.

45. Brown, J.M., and Wilson, W.R. (2004). Exploiting tumour hypoxia in cancer treatment. Nat. Rev. Cancer *4*, 437–447. https://doi.org/10.1038/nrc1367.

46. Chiche, J., Brahimi-Horn, M.C., and Pouysségur, J. (2010). Tumour hypoxia induces a metabolic shift causing acidosis: A common feature in cancer. J. Cell. Mol. Med. *14*, 771–794. https://doi.org/10.1111/j.1582-4934.2009.00994.x.

47. Shang, T., Jia, Z., Li, J., Cao, H., Xu, H., Cong, L., Ma, D., Wang, X., and Liu, J. (2025). Unraveling the triad of hypoxia, cancer cell stemness, and drug resistance. J. Hematol. Oncol. *18*, 32. https://doi.org/10.1186/s13045-025-01684-4.

48. Bhandari, V., Hoey, C., Liu, L.Y., Lalonde, E., Ray, J., Livingstone, J., Lesurf, R.,

Shiah, Y.J., Vujcic, T., Huang, X., et al. (2019). Molecular landmarks of tumor hypoxia across cancer types. Nat. Genet. *51*, 308–318. https://doi.org/10.1038/s41588-018-0318-2.

49. Graeber, T.G., Osmanian, C., Jacks, T., Housman, D.E., Koch, C.J., Lowe, S.W., and Giaccia, A.J. (1996). Hypoxia-mediated selection of cells with diminished apoptotic potential in solid tumours. Nature *379*, 88–91. https://doi.org/10.1038/379088a0.
50. Zheng, H., and Kang, Y. (2014). Multilayer control of the EMT master regulators. Oncogene *33*, 1755–1763. https://doi.org/10.1038/onc.2013.128.
51. Kagan, H.M., and Li, W. (2003). Lysyl oxidase: Properties, specificity, and biological roles inside and outside of the cell. J. Cell. Biochem. https://doi.org/10.1002/jcb.10413.
52. Winkler, J., Abisoye-Ogunniyan, A., Metcalf, K.J., and Werb, Z. (2020). Concepts of extracellular matrix remodelling in tumour progression and metastasis. Nat. Commun. *11*. https://doi.org/10.1038/s41467-020-18794-x.
53. Scharping, N.E., Rivadeneira, D.B., Menk, A. V., Vignali, P.D.A., Ford, B.R., Rittenhouse, N.L., Peralta, R., Wang, Y., Wang, Y., DePeaux, K., et al. (2021). Mitochondrial stress induced by continuous stimulation under hypoxia rapidly drives T cell exhaustion. Nat. Immunol. https://doi.org/10.1038/s41590-020-00834-9.
54. Henze, A.T., and Mazzone, M. (2016). The impact of hypoxia on tumor-associated macrophages. J. Clin. Invest. *126*, 3672–3679. https://doi.org/10.1172/JCI84427.
55. Facciabene, A., Peng, X., Hagemann, I.S., Balint, K., Barchetti, A., Wang, L.P., Gimotty, P.A., Gilks, C.B., Lal, P., Zhang, L., et al. (2011). Tumour hypoxia promotes tolerance and angiogenesis via CCL28 and T reg cells. Nature *475*, 226–230. https://doi.org/10.1038/nature10169.
56. Estephan, H., Tailor, A., Parker, R., Kreamer, M., Papandreou, I., Campo, L., Easton, A., Moon, E.J., Denko, N.C., Ternette, N., et al. (2025). Hypoxia promotes tumor immune evasion by suppressing MHC-I expression and antigen presentation. EMBO J. *44*, 903–922. https://doi.org/10.1038/s44318-024-00319-7.
57. Sethumadhavan, S., Silva, M., Philbrook, P., Nguyen, T., Hatfield, S.M., Ohta, A., and Sitkovsky, M. V. (2017). Hypoxia and hypoxia-inducible factor (HIF) downregulate antigen-presenting MHC class I molecules limiting tumor cell

recognition by T cells. PLoS One. https://doi.org/10.1371/journal.pone.0187314.

58. Barsoum, I.B., Smallwood, C.A., Siemens, D.R., and Graham, C.H. (2014). A mechanism of hypoxia-mediated escape from adaptive immunity in cancer cells. Cancer Res. *74*, 665–674. https://doi.org/10.1158/0008-5472.CAN-13-0992.

59. Miar, A., Arnaiz, E., Bridges, E., Beedie, S., Cribbs, A.P., Downes, D.J., Beagrie, R.A., Rehwinkel, J., and Harris, A.L. (2020). Hypoxia induces transcriptional and translational downregulation of the type i IFN pathway in multiple cancer cell types. Cancer Res. *80*, 5245–5256. https://doi.org/10.1158/0008-5472.CAN-19-2306.

60. Luger, K., Mäder, A.W., Richmond, R.K., Sargent, D.F., and Richmond, T.J. (1997). Crystal structure of the nucleosome core particle at 2.8 Å resolution. Nature. https://doi.org/10.1038/38444.

61. Klemm, S.L., Shipony, Z., and Greenleaf, W.J. (2019). Chromatin accessibility and the regulatory epigenome. Nat. Rev. Genet. *20*, 207–220. https://doi.org/10.1038/s41576-018-0089-8.

62. Allis, C.D., and Jenuwein, T. (2016). The molecular hallmarks of epigenetic control. Nat. Rev. Genet. *17*, 487–500. https://doi.org/10.1038/nrg.2016.59.

63. Zhao, S., Allis, C.D., and Wang, G.G. (2021). The language of chromatin modification in human cancers. Nat. Rev. Cancer *21*, 413–430. https://doi.org/10.1038/s41568-021-00357-x.

64. Wang, Z., Zang, C., Cui, K., Schones, D.E., Barski, A., Peng, W., and Zhao, K. (2009). Genome-wide Mapping of HATs and HDACs Reveals Distinct Functions in Active and Inactive Genes. Cell. https://doi.org/10.1016/j.cell.2009.06.049.

65. Martire, S., and Banaszynski, L.A. (2020). The roles of histone variants in fine-tuning chromatin organization and function. Nat. Rev. Mol. Cell Biol. *21*, 522–541. https://doi.org/10.1038/s41580-020-0262-8.

66. Calo, E., and Wysocka, J. (2013). Modification of Enhancer Chromatin: What, How, and Why? Mol. Cell *49*, 825–837. https://doi.org/10.1016/j.molcel.2013.01.038.

67. Isbel, L., Grand, R.S., and Schübeler, D. (2022). Generating specificity in genome regulation through transcription factor sensitivity to chromatin. Nat. Rev. Genet. *23*, 728–740. https://doi.org/10.1038/s41576-022-00512-6.

68. Tausendschön, M., Dehne, N., and Brüne, B. (2011). Hypoxia causes epigenetic gene regulation in macrophages by attenuating Jumonji histone demethylase

activity. Cytokine *53*, 256–262. https://doi.org/10.1016/j.cyto.2010.11.002.

69. Beyer, S., Kristensen, M.M., Jensen, K.S., Johansen, J.V., and Staller, P. (2008). The histone demethylases JMJD1A and JMJD2B are transcriptional targets of hypoxia-inducible factor HIF. J. Biol. Chem. *283*, 36542–36552. https://doi.org/10.1074/jbc.M804578200.

70. Batie, M., Frost, J., Frost, M., Wilson, J.W., Schofield, P., and Rocha, S. (2019). Hypoxia induces rapid changes to histone methylation and reprograms chromatin. Science (80-. ). *363*, 1222–1226. https://doi.org/10.1126/science.aau5870.

71. Chakraborty, A.A., Laukka, T., Myllykoski, M., Ringel, A.E., Booker, M.A., Tolstorukov, M.Y., Meng, Y.J., Meier, S.R., Jennings, R.B., Creech, A.L., et al. (2019). Histone demethylase KDM6A directly senses oxygen to control chromatin and cell fate. Science (80-. ). *363*, 1217–1222. https://doi.org/10.1126/science.aaw1026.

72. Kim, I., and Park, J.W. (2020). Hypoxia-driven epigenetic regulation in cancer progression: A focus on histone methylation and its modifying enzymes. Cancer Lett. *489*, 41–49. https://doi.org/10.1016/j.canlet.2020.05.025.

73. Olcina, M.M., Leszczynska, K.B., Senra, J.M., Isa, N.F., Harada, H., and Hammond, E.M. (2016). H3K9me3 facilitates hypoxia-induced p53-dependent apoptosis through repression of APAK. Oncogene *35*, 793–799. https://doi.org/10.1038/onc.2015.134.

74. Park, S., Cho, J.H., Kim, J.H., Park, M., Park, S., Kim, S.Y., Kim, S.K., Kim, K., Park, S.G., Park, B.C., et al. (2023). Hypoxia stabilizes SETDB1 to maintain genome stability. Nucleic Acids Res. *51*, 11178–11196. https://doi.org/10.1093/nar/gkad796.

75. Olcina, M.M., Foskolou, I.P., Anbalagan, S., Senra, J.M., Pires, I.M., Jiang, Y., Ryan, A.J., and Hammond, E.M. (2013). Replication stress and chromatin context link ATM activation to a role in DNA replication. Mol. Cell *52*, 758–766. https://doi.org/10.1016/j.molcel.2013.10.019.

76. Ma, T.S., Worth, K.R., Maher, C., Ng, N., Beghè, C., Gromak, N., Rose, A.M., and Hammond, E.M. (2023). Hypoxia-induced transcriptional stress is mediated by ROS-induced R-loops. Nucleic Acids Res. *51*, 11584–11599. https://doi.org/10.1093/nar/gkad858.

77. Collier, H., Albanese, A., Kwok, C.S., Kou, J., and Rocha, S. (2023). Functional crosstalk between chromatin and hypoxia signalling. Cell. Signal. *106*.

https://doi.org/10.1016/j.cellsig.2023.110660.

78. Thienpont, B., Steinbacher, J., Zhao, H., D'Anna, F., Kuchnio, A., Ploumakis, A., Ghesquière, B., Van Dyck, L., Boeckx, B., Schoonjans, L., et al. (2016). Tumour hypoxia causes DNA hypermethylation by reducing TET activity. Nature. https://doi.org/10.1038/nature19081.

79. Camuzi, D., de Amorim, Í.S.S., Ribeiro Pinto, L.F., Oliveira Trivilin, L., Mencalha, A.L., and Soares Lima, S.C. (2019). Regulation Is in the Air: The Relationship between Hypoxia and Epigenetics in Cancer. Cells *8*, 300. https://doi.org/10.3390/cells8040300.

80. Hu, Y., Li, Z., Zhang, Y., Wu, Y., Liu, Z., Zeng, J., Hao, Z., Li, J., Ren, J., and Yao, M. (2023). The Evolution of Tumor Microenvironment in Gliomas and Its Implication for Target Therapy. Int. J. Biol. Sci. *19*, 4311–4326. https://doi.org/10.7150/ijbs.83531.

81. Weller, M., van den Bent, M., Preusser, M., Le Rhun, E., Tonn, J.C., Minniti, G., Bendszus, M., Balana, C., Chinot, O., Dirven, L., et al. (2021). EANO guidelines on the diagnosis and treatment of diffuse gliomas of adulthood. Nat. Rev. Clin. Oncol. https://doi.org/10.1038/s41571-020-00447-z.

82. Louis, D.N., Perry, A., Wesseling, P., Brat, D.J., Cree, I.A., Figarella-Branger, D., Hawkins, C., Ng, H.K., Pfister, S.M., Reifenberger, G., et al. (2021). The 2021 WHO classification of tumors of the central nervous system: A summary. Neuro. Oncol. https://doi.org/10.1093/neuonc/noab106.

83. Miller, J.J., Gonzalez Castro, L.N., McBrayer, S., Weller, M., Cloughesy, T., Portnow, J., Andronesi, O., Barnholtz-Sloan, J.S., Baumert, B.G., Berger, M.S., et al. (2023). Isocitrate dehydrogenase (IDH) mutant gliomas: A Society for Neuro-Oncology (SNO) consensus review on diagnosis, management, and future directions. Neuro. Oncol. *25*, 4–25. https://doi.org/10.1093/neuonc/noac207.

84. Pellerino, A., Caccese, M., Padovan, M., Cerretti, G., and Lombardi, G. (2022). Epidemiology, risk factors, and prognostic factors of gliomas. Clin. Transl. Imaging *10*, 467–475. https://doi.org/10.1007/s40336-022-00489-6.

85. Neftel, C., Laffy, J., Filbin, M.G., Hara, T., Shore, M.E., Rahme, G.J., Richman, A.R., Silverbush, D., Shaw, M.L., Hebert, C.M., et al. (2019). An Integrative Model of Cellular States, Plasticity, and Genetics for Glioblastoma. Cell. https://doi.org/10.1016/j.cell.2019.06.024.

86. Greenwald, A.C., Darnell, N.G., Hoefflin, R., Simkin, D., Mount, C.W., Gonzalez

Castro, L.N., Harnik, Y., Dumont, S., Hirsch, D., Nomura, M., et al. (2024). Integrative spatial analysis reveals a multi-layered organization of glioblastoma. Cell *187*, 2485-2501.e26. https://doi.org/10.1016/j.cell.2024.03.029.

87. Ravi, V.M., Will, P., Kueckelhaus, J., Sun, N., Joseph, K., Salié, H., Vollmer, L., Kuliesiute, U., von Ehr, J., Benotmane, J.K., et al. (2022). Spatially resolved multi-omics deciphers bidirectional tumor-host interdependence in glioblastoma. Cancer Cell *40*, 639-655.e13. https://doi.org/10.1016/j.ccell.2022.05.009.
88. Ortiz, R., Perazzoli, G., Cabeza, L., Jiménez-Luna, C., Luque, R., Prados, J., and Melguizo, C. (2020). Temozolomide: An Updated Overview of Resistance Mechanisms, Nanotechnology Advances and Clinical Applications. Curr. Neuropharmacol. https://doi.org/10.2174/1570159x18666200626204005.
89. Colopi, A., Fuda, S., Santi, S., Onorato, A., Cesarini, V., Salvati, M., Balistrieri, C.R., Dolci, S., and Guida, E. (2023). Impact of age and gender on glioblastoma onset, progression, and management. Mech. Ageing Dev. https://doi.org/10.1016/j.mad.2023.111801.
90. Hambardzumyan, D., and Bergers, G. (2015). Glioblastoma: Defining Tumor Niches. Trends in Cancer *1*, 252–265. https://doi.org/10.1016/j.trecan.2015.10.009.
91. Markwell, S.M., Ross, J.L., Olson, C.L., and Brat, D.J. (2022). Necrotic reshaping of the glioma microenvironment drives disease progression. Acta Neuropathol. *143*, 291–310. https://doi.org/10.1007/s00401-021-02401-4.
92. Michelucci, A., Sforna, L., Franciolini, F., and Catacuzzeno, L. (2023). Hypoxia, Ion Channels and Glioblastoma Malignancy. Biomolecules *13*, 1742. https://doi.org/10.3390/biom13121742.
93. Brat, D.J., and Van Meir, E.G. (2004). Vaso-occlusive and prothrombotic mechanisms associated with tumor hypoxia, necrosis, and accelerated growth in glioblastoma. Lab. Investig. *84*, 397–405. https://doi.org/10.1038/labinvest.3700070.
94. Sharma, P., Aaroe, A., Liang, J., and Puduvalli, V.K. (2023). Tumor microenvironment in glioblastoma: Current and emerging concepts. Neuro-Oncology Adv. https://doi.org/10.1093/noajnl/vdad009.
95. Hambardzumyan, D., Gutmann, D.H., and Kettenmann, H. (2016). The role of microglia and macrophages in glioma maintenance and progression. Nat. Neurosci. *19*, 20–27. https://doi.org/10.1038/nn.4185.

96. Prinz, M., Masuda, T., Wheeler, M.A., and Quintana, F.J. (2021). Microglia and Central Nervous System–Associated Macrophages—From Origin to Disease Modulation. Annu. Rev. Immunol. *39*, 251–277. https://doi.org/10.1146/annurev-immunol-093019-110159.

97. Shi, C., and Pamer, E.G. (2011). Monocyte recruitment during infection and inflammation. Nat. Rev. Immunol. *11*, 762–774. https://doi.org/10.1038/nri3070.

98. Ellert-Miklaszewska, A., Pasierbinska, M., Poleszak, K., and Kamińska, B. (2018). Molekularne podłoże oddziaływania komórek nowotworowych z mikrośrodowiskiem w glejakach złośliwych. Postepy Biochem. *64*, 129–140. https://doi.org/10.18388/pb.2018_123.

99. Szulzewsky, F., Pelz, A., Feng, X., Synowitz, M., Markovic, D., Langmann, T., Holtman, I.R., Wang, X., Eggen, B.J.L., Boddeke, H.W.G.M., et al. (2015). Glioma-associated microglia/macrophages display an expression profile different from M1 and M2 polarization and highly express Gpnmb and Spp1. PLoS One *10*, 1–27. https://doi.org/10.1371/journal.pone.0116644.

100. Zhao, W., Zhang, Z., Xie, M., Ding, F., Zheng, X., Sun, S., and Du, J. (2025). Exploring tumor-associated macrophages in glioblastoma: from diversity to therapy. npj Precis. Oncol. *9*. https://doi.org/10.1038/s41698-025-00920-x.

101. Ochocka, N., Segit, P., Walentynowicz, K.A., Wojnicki, K., Cyranowski, S., Swatler, J., Mieczkowski, J., and Kaminska, B. (2021). Single-cell RNA sequencing reveals functional heterogeneity of glioma-associated brain macrophages. Nat. Commun. *12*. https://doi.org/10.1038/s41467-021-21407-w.

102. Pombo Antunes, A.R., Scheyltjens, I., Lodi, F., Messiaen, J., Antoranz, A., Duerinck, J., Kancheva, D., Martens, L., De Vlaminck, K., Van Hove, H., et al. (2021). Single-cell profiling of myeloid cells in glioblastoma across species and disease stage reveals macrophage competition and specialization. Nat. Neurosci. *24*, 595–610. https://doi.org/10.1038/s41593-020-00789-y.

103. Wang, W., Li, T., Cheng, Y., Li, F., Qi, S., Mao, M., Wu, J., Liu, Q., Zhang, X., Li, X., et al. (2024). Identification of hypoxic macrophages in glioblastoma with therapeutic potential for vasculature normalization. Cancer Cell *42*, 815-832.e12. https://doi.org/10.1016/j.ccell.2024.03.013.

104. Yabo, Y.A., Moreno-Sanchez, P.M., Pires-Afonso, Y., Kaoma, T., Nosirov, B., Scafidi, A., Ermini, L., Lipsa, A., Oudin, A., Kyriakis, D., et al. (2024). Glioblastoma-instructed microglia transition to heterogeneous phenotypic states

with phagocytic and dendritic cell-like features in patient tumors and patient-derived orthotopic xenografts. Genome Med. *16*, 1–29. https://doi.org/10.1186/s13073-024-01321-8.

105. Banerjee, K., Ratzabi, A., Caspit, I.M., Ganon, O., Blinder, P., Jung, S., and Stein, R. (2023). Distinct spatiotemporal features of microglia and monocyte-derived macrophages in glioma. Eur. J. Immunol. https://doi.org/10.1002/eji.202250161.
106. Saavedra-López, E., Roig-Martínez, M., Cribaro, G.P., Casanova, P. V., Gallego, J.M., Pérez-Vallés, A., and Barcia, C. (2020). Phagocytic glioblastoma-associated microglia and macrophages populate invading pseudopalisades. Brain Commun. *2*. https://doi.org/10.1093/braincomms/fcz043.
107. Sattiraju, A., Kang, S., Giotti, B., Chen, Z., Marallano, V.J., Brusco, C., Ramakrishnan, A., Shen, L., Tsankov, A.M., Hambardzumyan, D., et al. (2023). Hypoxic niches attract and sequester tumor-associated macrophages and cytotoxic T cells and reprogram them for immunosuppression. Immunity *56*, 1825-1843.e6. https://doi.org/10.1016/j.immuni.2023.06.017.
108. Haley, M.J., Bere, L., Minshull, J., Georgaka, S., Garcia-Martin, N., Howell, G., Coope, D.J., Roncaroli, F., King, A., Wedge, D.C., et al. (2024). Hypoxia coordinates the spatial landscape of myeloid cells within glioblastoma to affect survival. Sci. Adv. *10*, 1–19. https://doi.org/10.1126/sciadv.adj3301.
109. Kloosterman, D.J., Erbani, J., Boon, M., Farber, M., Handgraaf, S.M., Ando-Kuri, M., Sánchez-López, E., Fontein, B., Mertz, M., Nieuwland, M., et al. (2024). Macrophage-mediated myelin recycling fuels brain cancer malignancy. Cell *187*, 5336-5356.e30. https://doi.org/10.1016/j.cell.2024.07.030.
110. Chen, X., Shen, Y., Draper, W., Buenrostro, J.D., Litzenburger, U., Cho, S.W., Satpathy, A.T., Carter, A.C., Ghosh, R.P., East-Seletsky, A., et al. (2016). ATAC-see reveals the accessible genome by transposase-mediated imaging and sequencing. Nat. Methods *13*, 1013–1020. https://doi.org/10.1038/nmeth.4031.
111. Buenrostro, J.D., Wu, B., Litzenburger, U.M., Ruff, D., Gonzales, M.L., Snyder, M.P., Chang, H.Y., and Greenleaf, W.J. (2015). Single-cell chromatin accessibility reveals principles of regulatory variation. Nature. https://doi.org/10.1038/nature14590.
112. Bolger, A.M., Lohse, M., and Usadel, B. (2014). Trimmomatic: A flexible trimmer for Illumina sequence data. Bioinformatics *30*, 2114–2120. https://doi.org/10.1093/bioinformatics/btu170.

113. Langmead, B., and Salzberg, S.L. (2012). Fast gapped-read alignment with Bowtie 2. Nat. Methods *9*, 357–359. https://doi.org/10.1038/nmeth.1923.

114. Kim, D., Langmead, B., and Salzberg, S.L. (2015). HISAT: A fast spliced aligner with low memory requirements. Nat. Methods *12*, 357–360. https://doi.org/10.1038/nmeth.3317.

115. Zhang, Y., Liu, T., Meyer, C.A., Eeckhoute, J., Johnson, D.S., Bernstein, B.E., Nussbaum, C., Myers, R.M., Brown, M., Li, W., et al. (2008). Model-based analysis of ChIP-Seq (MACS). Genome Biol. *9*. https://doi.org/10.1186/gb-2008-9-9-r137.

116. Robinson, J.T., Thorvaldsdóttir, H., Winckler, W., Guttman, M., Lander, E.S., Getz, G., and Mesirov, J.P. (2011). Integrative genomics viewer. Nat. Biotechnol. *29*, 24–26. https://doi.org/10.1038/nbt.1754.

117. Ramírez, F., Ryan, D.P., Grüning, B., Bhardwaj, V., Kilpert, F., Richter, A.S., Heyne, S., Dündar, F., and Manke, T. (2016). deepTools2: a next generation web server for deep-sequencing data analysis. Nucleic Acids Res. *44*, W160–W165. https://doi.org/10.1093/NAR/GKW257.

118. Love, M.I., Huber, W., and Anders, S. (2014). Moderated estimation of fold change and dispersion for RNA-seq data with DESeq2. Genome Biol. *15*. https://doi.org/10.1186/s13059-014-0550-8.

119. Robinson, M.D., McCarthy, D.J., and Smyth, G.K. (2009). edgeR: A Bioconductor package for differential expression analysis of digital gene expression data. Bioinformatics *26*, 139–140. https://doi.org/10.1093/bioinformatics/btp616.

120. Lawrence, M., Huber, W., Pagès, H., Aboyoun, P., Carlson, M., Gentleman, R., Morgan, M.T., and Carey, V.J. (2013). Software for Computing and Annotating Genomic Ranges. PLoS Comput. Biol. *9*. https://doi.org/10.1371/journal.pcbi.1003118.

121. Schep, A.N., Wu, B., Buenrostro, J.D., and Greenleaf, W.J. (2017). ChromVAR: Inferring transcription-factor-associated accessibility from single-cell epigenomic data. Nat. Methods *14*, 975–978. https://doi.org/10.1038/nmeth.4401.

122. Yu, G., Wang, L.G., and He, Q.Y. (2015). ChIP seeker: An R/Bioconductor package for ChIP peak annotation, comparison and visualization. Bioinformatics *31*, 2382–2383. https://doi.org/10.1093/bioinformatics/btv145.

123. Yu, G., Wang, L.G., Han, Y., and He, Q.Y. (2012). ClusterProfiler: An R package

for comparing biological themes among gene clusters. Omi. A J. Integr. Biol. *16*, 284–287. https://doi.org/10.1089/omi.2011.0118.

124. Supek, F., Bošnjak, M., Škunca, N., and Šmuc, T. (2011). Revigo summarizes and visualizes long lists of gene ontology terms. PLoS One *6*. https://doi.org/10.1371/journal.pone.0021800.

125. Shannon, P., Markiel, A., Ozier, O., Baliga, N.S., Wang, J.T., Ramage, D., Amin, N., Schwikowski, B., and Ideker, T. (2003). Cytoscape: A software Environment for integrated models of biomolecular interaction networks. Genome Res. *13*, 2498–2504. https://doi.org/10.1101/gr.1239303.

126. Heinz, S., Benner, C., Spann, N., Bertolino, E., Lin, Y.C., Laslo, P., Cheng, J.X., Murre, C., Singh, H., and Glass, C.K. (2010). Simple Combinations of Lineage-Determining Transcription Factors Prime cis-Regulatory Elements Required for Macrophage and B Cell Identities. Mol. Cell *38*, 576–589. https://doi.org/10.1016/j.molcel.2010.05.004.

127. Grant, C.E., Bailey, T.L., and Noble, W.S. (2011). FIMO: Scanning for occurrences of a given motif. Bioinformatics. https://doi.org/10.1093/bioinformatics/btr064.

128. Cook, A., Mieczkowski, J., and Tolstorukov, M.Y. (2017). Single-assay profiling of nucleosome occupancy and chromatin accessibility. Curr. Protoc. Mol. Biol. *2017*, 21.34.1-21.34.18. https://doi.org/10.1002/cpmb.45.

129. Channathodiyi, P., and Houseley, J. (2021). Glyoxal fixation facilitates transcriptome analysis after antigen staining and cell sorting by flow cytometry. PLoS One *16*. https://doi.org/10.1371/journal.pone.0240769.

130. Dobin, A., Davis, C.A., Schlesinger, F., Drenkow, J., Zaleski, C., Jha, S., Batut, P., Chaisson, M., and Gingeras, T.R. (2013). STAR: Ultrafast universal RNA-seq aligner. Bioinformatics *29*, 15–21. https://doi.org/10.1093/bioinformatics/bts635.

131. Anders, S., Pyl, P.T., and Huber, W. (2015). HTSeq-A Python framework to work with high-throughput sequencing data. Bioinformatics *31*, 166–169. https://doi.org/10.1093/bioinformatics/btu638.

132. Puchalski, R.B., Shah, N., Miller, J., Dalley, R., Nomura, S.R., Yoon, J.G., Smith, K.A., Lankerovich, M., Bertagnolli, D., Bickley, K., et al. (2018). An anatomic transcriptional atlas of human glioblastoma. Science (80-. ). *360*, 660–663. https://doi.org/10.1126/science.aaf2666.

133. Hao, Y., Stuart, T., Kowalski, M.H., Choudhary, S., Hoffman, P., Hartman, A.,

Srivastava, A., Molla, G., Madad, S., Fernandez-Granda, C., et al. (2024). Dictionary learning for integrative, multimodal and scalable single-cell analysis. Nat. Biotechnol. *42*, 293–304. https://doi.org/10.1038/s41587-023-01767-y.

134. Brady, L.K., Wang, H., Radens, C.M., Bi, Y., Radovich, M., Maity, A., Ivan, C., Ivan, M., Barash, Y., and Koumenis, C. (2017). Transcriptome analysis of hypoxic cancer cells uncovers intron retention in EIF2B5 as a mechanism to inhibit translation. PLoS Biol. https://doi.org/10.1371/journal.pbio.2002623.
135. Yu, Z., Mersaoui, S.Y., Guitton-Sert, L., Coulombe, Y., Song, J., Masson, J.Y., and Richard, S. (2020). DDX5 resolves R-loops at DNA double-strand breaks to promote DNA repair and avoid chromosomal deletions. NAR Cancer *2*. https://doi.org/10.1093/narcan/zcaa028.
136. Leszczynska, K.B., Dzwigonska, M., Estephan, H., Moehlenbrink, J., Bowler, E., Giaccia, A.J., Mieczkowski, J., Kaminska, B., and Hammond, E.M. (2023). Hypoxia-mediated regulation of DDX5 through decreased chromatin accessibility and post-translational targeting restricts R-loop accumulation. Mol. Oncol. *17*, 1173–1191. https://doi.org/10.1002/1878-0261.13431.
137. Quail, D.F., and Joyce, J.A. (2017). The Microenvironmental Landscape of Brain Tumors. Cancer Cell *31*, 326–341. https://doi.org/10.1016/j.ccell.2017.02.009.
138. Ivan, M., Kondo, K., Yang, H., Kim, W., Valiando, J., Ohh, M., Salic, A., Asara, J.M., Lane, W.S., and Kaelin, J. (2001). HIFα targeted for VHL-mediated destruction by proline hydroxylation: Implications for O2 sensing. Science (80-. ). *292*, 464–468. https://doi.org/10.1126/science.1059817.
139. Lombardi, O., Li, R., Halim, S., Choudhry, H., Ratcliffe, P.J., and Mole, D.R. (2022). Pan-cancer analysis of tissue and single-cell HIF-pathway activation using a conserved gene signature. Cell Rep. *41*. https://doi.org/10.1016/j.celrep.2022.111652.
140. Batie, M., Frost, J., Shakir, D., and Rocha, S. (2022). Regulation of chromatin accessibility by hypoxia and HIF. Biochem. J. *479*, 767–786. https://doi.org/10.1042/BCJ20220008.
141. Rocha, S. (2007). Gene regulation under low oxygen: holding your breath for transcription. Trends Biochem. Sci. *32*, 389–397. https://doi.org/10.1016/j.tibs.2007.06.005.
142. Liao, X., Sharma, N., Kapadia, F., Zhou, G., Lu, Y., Hong, H., Paruchuri, K., Mahabeleshwar, G.H., Dalmas, E., Venteclef, N., et al. (2011). Krüppel-like factor

4 regulates macrophage polarization. J. Clin. Invest. *121*, 2736–2749. https://doi.org/10.1172/JCI45444.

143. Knights, A.J., Yang, L., Shah, M., Norton, L.J., Green, G.S., Stout, E.S., Vohralik, E.J., Crossley, M., and Quinlan, K.G.R. (2020). Krüppel-like factor 3 (klf3) suppresses nf-b-driven inflammation in mice. J. Biol. Chem. *295*, 608–6091. https://doi.org/10.1074/jbc.RA120.013114.

144. Vollmann, H., Wölfel, S., Ohneseit, P., Stransky, E., Vonthein, R., Wick, W., Meyermann, R., and Simon, P. (2007). Differential expression of Egr1 and activation of microglia following irradiation in the rat brain. Strahlentherapie und Onkol. *183*, 248–255. https://doi.org/10.1007/s00066-007-1664-7.

145. Guo, H., Du, M., Yang, Y., Lin, X., Wang, Y., Li, H., Ren, J., Xu, W., Yan, J., and Wang, N. (2024). Sp1 Regulates the M1 Polarization of Microglia Through the HuR/NF-κB Axis after Spinal Cord Injury. Neuroscience *544*, 50–63. https://doi.org/10.1016/j.neuroscience.2024.02.014.

146. Zucker, S.N., Fink, E.E., Bagati, A., Mannava, S., Bianchi-Smiraglia, A., Bogner, P.N., Wawrzyniak, J.A., Foley, C., Leonova, K.I., Grimm, M.J., et al. (2014). Nrf2 amplifies oxidative stress via induction of Klf9. Mol. Cell *53*, 916–928. https://doi.org/10.1016/j.molcel.2014.01.033.

147. Abutbul, S., Shapiro, J., Szaingurten-Solodkin, I., Levy, N., Carmy, Y., Baron, R., Jung, S., and Monsonego, A. (2012). TGF-β signaling through SMAD2/3 induces the quiescent microglial phenotype within the CNS environment. Glia *60*, 1160–1171. https://doi.org/10.1002/glia.22343.

148. Rivera-Ramos, A., Cruz-Hernández, L., Talaverón, R., Sánchez-Montero, M.T., García-Revilla, J., Mulero-Acevedo, M., Deierborg, T., Venero, J.L., and Sarmiento Soto, M. (2024). Galectin-3 depletion tames pro-tumoural microglia and restrains cancer cells growth. Cancer Lett. *591*. https://doi.org/10.1016/j.canlet.2024.216879.

149. Atsaves, V., Leventaki, V., Rassidakis, G.Z., and Claret, F.X. (2019). AP-1 transcription factors as regulators of immune responses in cancer. Cancers (Basel). *11*. https://doi.org/10.3390/cancers11071037.

150. Sha, H., Zhang, D., Zhang, Y., Wen, Y., and Wang, Y. (2017). ATF3 promotes migration and M1/M2 polarization of macrophages by activating tenascin-C via Wnt/β-catenin pathway. Mol. Med. Rep. *16*, 3641–3647. https://doi.org/10.3892/mmr.2017.6992.

151. Hu, S., Zhao, X., Li, R., Hu, C., Wu, H., Li, J., Zhang, Y., and Xu, Y. (2022). Activating transcription factor 3, glucolipid metabolism, and metabolic diseases. J. Mol. Cell Biol. *14*. https://doi.org/10.1093/jmcb/mjac067.

152. Laderoute, K.R., Calaoagan, J.M., Gustafson-Brown, C., Knapp, A.M., Li, G.-C., Mendonca, H.L., Ryan, H.E., Wang, Z., and Johnson, R.S. (2002). The Response of c-Jun/AP-1 to Chronic Hypoxia Is Hypoxia-Inducible Factor 1α Dependent. Mol. Cell. Biol. *22*, 2515–2523. https://doi.org/10.1128/mcb.22.8.2515-2523.2002.

153. Obacz, J., Pastorekova, S., Vojtesek, B., and Hrstka, R. (2013). Cross-talk between HIF and p53 as mediators of molecular responses to physiological and genotoxic stresses. Mol. Cancer *12*. https://doi.org/10.1186/1476-4598-12-93.

154. Karthikeyan, A., Gupta, N., Tang, C., Mallilankaraman, K., Silambarasan, M., Shi, M., Lu, L., Ang, B.T., Ling, E.A., and Dheen, S.T. (2018). Microglial SMAD4 regulated by microRNA-146a promotes migration of microglia which support tumor progression in a glioma environment. Oncotarget *9*, 24950–24969. https://doi.org/10.18632/oncotarget.25116.

155. Maurya, S.K., Gupta, S., and Mishra, R. (2023). Transcriptional and epigenetic regulation of microglia in maintenance of brain homeostasis and neurodegeneration. Front. Mol. Neurosci. *15*. https://doi.org/10.3389/fnmol.2022.1072046.

156. Oikawa, M., Abe, M., Kurosawa, H., Hida, W., Shirato, K., and Sato, Y. (2001). Hypoxia induces transcription factor ETS-1 via the activity of hypoxia-lnducible factor-1. Biochem. Biophys. Res. Commun. *289*, 39–43. https://doi.org/10.1006/bbrc.2001.5927.

157. Tarassishin, L., Suh, H.S., and Lee, S.C. (2011). Interferon regulatory factor 3 plays an anti-inflammatory role in microglia by activating the PI3K/Akt pathway. J. Neuroinflammation *8*. https://doi.org/10.1186/1742-2094-8-187.

158. Vázquez-Cabrera, G., Škandík, M., Roncier, N., Real Oualit, F., Cruz De Los Santos, M., Baleviciute, A., Cheray, M., and Joseph, B. (2024). ID2-ETS2 axis regulates the transcriptional acquisition of pro-tumoral microglia phenotype in glioma. Cell Death Dis. *15*. https://doi.org/10.1038/s41419-024-06903-3.

159. De Oliveira, J.T., Ribeiro, C., Barros, R., Gomes, C., De Matos, A.J., Reis, C.A., Rutteman, G.R., and Gärtner, F. (2015). Hypoxia up-regulates galectin-3 in mammary tumor progression and metastasis. PLoS One *10*.

https://doi.org/10.1371/journal.pone.0134458.

160. Ikemori, R.Y., Machado, C.M.L., Furuzawa, K.M., Nonogaki, S., Osinaga, E., Umezawa, K., De Carvalho, M.A., Verinaud, L., and Chammas, R. (2014). Galectin-3 up-regulation in hypoxic and nutrient deprived microenvironments promotes cell survival. PLoS One *9*. https://doi.org/10.1371/journal.pone.0111592.

161. Kindrick, J.D., and Mole, D.R. (2020). Hypoxic Regulation of Gene Transcription and Chromatin: Cause and Effect. Int. J. Mol. Sci. *21*, 8320. https://doi.org/10.3390/ijms21218320.

162. Li, Y., Gruber, J.J., Litzenburger, U.M., Zhou, Y., Miao, Y.R., LaGory, E.L., Li, A.M., Hu, Z., Yip, M., Hart, L.S., et al. (2020). Acetate supplementation restores chromatin accessibility and promotes tumor cell differentiation under hypoxia. Cell Death Dis. *11*. https://doi.org/10.1038/s41419-020-2303-9.

163. Xin, J., Zhang, H., He, Y., Duren, Z., Bai, C., Chen, L., Luo, X., Yan, D.S., Zhang, C., Zhu, X., et al. (2020). Chromatin accessibility landscape and regulatory network of high-altitude hypoxia adaptation. Nat. Commun. *11*. https://doi.org/10.1038/s41467-020-18638-8.

164. Ward, M.C., Banovich, N.E., Sarkar, A., Stephens, M., and Gilad, Y. (2021). Dynamic effects of genetic variation on gene expression revealed following hypoxic stress in cardiomyocytes. Elife *10*, 1–33. https://doi.org/10.7554/eLife.57345.

165. Buonfiglioli, A., and Hambardzumyan, D. (2021). Macrophages and microglia: the cerberus of glioblastoma. Acta Neuropathol. Commun. *9*, 54. https://doi.org/10.1186/s40478-021-01156-z.

166. Wang, L., Li, Y.S., Yu, L.G., Zhang, X.K., Zhao, L., Gong, F.L., Yang, X.X., and Guo, X.L. (2020). Galectin-3 expression and secretion by tumor-associated macrophages in hypoxia promotes breast cancer progression. Biochem. Pharmacol. *178*. https://doi.org/10.1016/j.bcp.2020.114113.

167. Yeh, H., and Ikezu, T. (2019). Transcriptional and Epigenetic Regulation of Microglia in Health and Disease. Trends Mol. Med. *25*, 96–111. https://doi.org/10.1016/j.molmed.2018.11.004.

168. Mancino, A., Termanini, A., Barozzi, I., Ghisletti, S., Ostuni, R., Prosperini, E., Ozato, K., and Natoli, G. (2015). A dual cis-regulatory code links IRF8 to constitutive and inducible gene expression in macrophages. Genes Dev. *29*, 394–

408. https://doi.org/10.1101/gad.257592.114.

169. Saeki, K., Pan, R., Lee, E., Kurotaki, D., and Ozato, K. (2024). IRF8 defines the epigenetic landscape in postnatal microglia, thereby directing their transcriptome programs. Nat. Immunol. *25*, 1928–1942. https://doi.org/10.1038/s41590-024-01962-2.

170. Taylor, C.T., and Scholz, C.C. (2022). The effect of HIF on metabolism and immunity. Nat. Rev. Nephrol. *18*, 573–587. https://doi.org/10.1038/s41581-022-00587-8.

171. Prickaerts, P., Adriaens, M.E., Beucken, T. van den, Koch, E., Dubois, L., Dahlmans, V.E.H., Gits, C., Evelo, C.T.A., Chan-Seng-Yue, M., Wouters, B.G., et al. (2016). Hypoxia increases genome-wide bivalent epigenetic marking by specific gain of H3K27me3. Epigenetics and Chromatin. https://doi.org/10.1186/s13072-016-0086-0.

172. Hafner, A., and Boettiger, A. (2023). The spatial organization of transcriptional control. Nat. Rev. Genet. *24*, 53–68. https://doi.org/10.1038/s41576-022-00526-0.

173. Gao, C., Gao, A., Jiang, Y., Gao, R., Guo, Y., Peng, Z., Jiang, W., Zhang, M., Zhou, Z., Yan, C., et al. (2025). Hypoxia-induced phase separation of ZHX2 alters chromatin looping to drive cancer metastasis. Mol. Cell *85*, 1525-1542.e10. https://doi.org/10.1016/j.molcel.2025.03.009.

174. Beloribi-Djefaflia, S., Vasseur, S., and Guillaumond, F. (2016). Lipid metabolic reprogramming in cancer cells. Oncogenesis *5*. https://doi.org/10.1038/ONCSIS.2015.49.

175. Munir, R., Lisec, J., Swinnen, J. V., and Zaidi, N. (2019). Lipid metabolism in cancer cells under metabolic stress. Br. J. Cancer *120*, 1090–1098. https://doi.org/10.1038/s41416-019-0451-4.

176. Gonzalez, G.A., Osuji, E.U., Fiur, N.C., Clark, M.G., Ma, S., Lukov, L.L., and Zhang, C. (2025). Alteration of Lipid Metabolism in Hypoxic Cancer Cells. Chem. Biomed. Imaging *3*, 25–34. https://doi.org/10.1021/cbmi.4c00050.

177. Wu, H., Han, Y., Rodriguez Sillke, Y., Deng, H., Siddiqui, S., Treese, C., Schmidt, F., Friedrich, M., Keye, J., Wan, J., et al. (2019). Lipid droplet-dependent fatty acid metabolism controls the immune suppressive phenotype of tumor-associated macrophages. EMBO Mol. Med. *11*. https://doi.org/10.15252/emmm.201910698.

178. Masetti, M., Carriero, R., Portale, F., Marelli, G., Morina, N., Pandini, M., Iovino, M., Partini, B., Erreni, M., Ponzetta, A., et al. (2021). Lipid-loaded tumor-

associated macrophages sustain tumor growth and invasiveness in prostate cancer. J. Exp. Med. *219*. https://doi.org/10.1084/jem.20210564.

179. Luo, Q., Zheng, N., Jiang, L., Wang, T., Zhang, P., Liu, Y., Zheng, P., Wang, W., Xie, G., Chen, L., et al. (2020). Lipid accumulation in macrophages confers protumorigenic polarization and immunity in gastric cancer. Cancer Sci. *111*, 4000–4011. https://doi.org/10.1111/cas.14616.

180. Monteiro-Cardoso, V.F., and Giordano, F. (2024). Emerging functions of the mitochondria–ER–lipid droplet three-way junction in coordinating lipid transfer, metabolism, and storage in cells. FEBS Lett. *598*, 1252–1273. https://doi.org/10.1002/1873-3468.14893.

181. Deng, Y., Zhou, C., Mirza, A.H., Bamigbade, A.T., Zhang, S., Xu, S., and Liu, P. (2021). Rab18 binds PLIN2 and ACSL3 to mediate lipid droplet dynamics. Biochim. Biophys. Acta - Mol. Cell Biol. Lipids *1866*. https://doi.org/10.1016/j.bbalip.2021.158923.

182. Mosser, D.M., Hamidzadeh, K., and Goncalves, R. (2021). Macrophages and the maintenance of homeostasis, https://doi.org/10.1038/s41423-020-00541-3 https://doi.org/10.1038/s41423-020-00541-3.

183. Zhao, S., Zhao, R., Wang, C., Ma, C., Gao, Z., Li, B., Qi, Y., Qiu, W., Pan, Z., Wang, S., et al. (2024). HDAC7 drives glioblastoma to a mesenchymal-like state via LGALS3-mediated crosstalk between cancer cells and macrophages. Theranostics *14*, 7072–7087. https://doi.org/10.7150/thno.100939.

184. El Omari, N., Bakrim, S., Khalid, A., Abdalla, A.N., Almalki, W.H., Lee, L.H., Ardianto, C., Ming, L.C., and Bouyahya, A. (2023). Molecular mechanisms underlying the clinical efficacy of panobinostat involve Stochasticity of epigenetic signaling, sensitization to anticancer drugs, and induction of cellular cell death related to cellular stresses. Biomed. Pharmacother. *164*. https://doi.org/10.1016/j.biopha.2023.114886.